SURFACE-ENHANCED RAMAN SCATTERING FOR THE RELIABLE AND REPRODUCIBLE DETECTION OF DISEASE ANTIGENS IN BIOLOGICALLY RELEVANT MEDIA

by

Alexis Cathrine Crawford

A dissertation submitted to the faculty of
The University of Utah
in partial fulfillment of the requirements for the degree of

Doctor of Philosophy

Department of Chemistry

The University of Utah

May 2016

The University of Utah Graduate School

STATEMENT OF DISSERTATION APPROVAL

The dissertation of **Alexis Cathrine Crawford**

has been approved by the following supervisory committee members:

Marc D. Porter	, Chair	**12/01/2015** Date Approved
Joel Mark Harris	, Member	**12/01/2015** Date Approved
Jennifer Shumaker-Parry	, Member	**12/01/2015** Date Approved
Michael David Morse	, Member	**12/01/2015** Date Approved
Hamidreza S. Ghandehari	, Member	**12/01/2015** Date Approved

and by **Cynthia Burrows** , Chair/Dean of

the Department/College/School of **Chemistry**

and by David B. Kieda, Dean of The Graduate School.

ABSTRACT

Surface-enhanced Raman scattering (SERS) is a technique that can be used for the detection of materials down to the single molecule level. The development of the extrinsic Raman Label (ERL) that incorporates biorecognition, a Raman reporter molecule, and gold nanoparticles (AuNPs), is the base for an extensible, sensitive, and selective SERS-based sandwich immunoassay. The use of SERS as a quantitative detection platform, however, has not progressed past the laboratory.

Research presented here in describes how the analysis and production of a SERS immunoassay substrate has a significant role in the reliability and reproducibility of SERS substrates. First, the analysis of the SERS immunoassay platform and can be simulated as a random distribution of points on a surface. Simulation results indicated the best method to improve the accuracy of the analysis was through increasing the number of measurements or increasing the area measured by a single measurement. The precision of the measurement, however, was only improved by increasing the analysis area. This indicates that a larger laser spot used for analysis improves the accuracy and precision of SERS measurements. Second, to produce a SERS substrate with a random distribution of ERLs, the adsorption of ERLs should follow diffusional transport to increase the uniformity of ERLs on the substrate. By inverting the substrates during the ERL incubation step, sedimentation of the ERLs is directed away from the substrate and stable ERLs left

in suspension diffuse to the substrate. Diffusional transport and a more even distribution of ERLs increased the reliability and reproducibility of the SERS substrates.

Improved SERS immunoassay techniques implemented in conjunction with a novel pretreatment of serum samples for tuberculosis (TB) diagnostics was used to validate the SERS method. The TB marker mannose-capped lipoarabinomannan (ManLAM) is a lipopolysaccharide cell wall component that is constantly sloughed off the surface of the virulent bacterium, *Mycobacterium tuberculosis*. Normally ManLAM complexes with serum protein inhibiting detection but the use of a simple five step pretreatment method frees ManLAM improving the limit of detection (LoD). Improved SERS methodologies and sample pretreatment provide promising sensitivity and specificity for set of patient samples.

“Be who you are and say what you feel,
because those who mind don't matter
and those who matter don't mind.”

~Dr. Seuss

TABLE OF CONTENTS

LIST OF SCHEMES

LIST OF FIGURES

ABBREVIATIONS

$\langle\overline{x^2}\rangle$ ..... root mean square distance
2D ..... two-dimensional
AAR ..... area analysis ratio
Ab ..... antibody
ACN ..... acetonitrile
ACR ..... α-crystalline protein
ACS ..... American chemical society
AFM ..... atomic force microscopy
Ag ..... antigen
AIDS ..... acquired immune deficiency syndrome
AuNP ..... gold nanoparticle
BB ..... borate buffer
BBT ..... 2.0 mM borate buffer with 0.1% Tween 20
BCG ..... non-Bacillus Calmette–Guérin
B_D ..... incident beam diameter
BSA ..... bovine serum albumin
C ..... concentration of particles in solution
CaDPA ..... calcium dipicolinate
CCD ..... charge coupled device
CSF ..... cerebral spinal fluid
CSU ..... Colorado state university
DAB ..... p-dimethylaminoazobenzene
$\mathcal{D}_{\text{Avg}}$ ..... average absolute deviation from the mean
DLS ..... dynamic light scattering
dS ..... flux of points through the area
DSP ..... dithiobis(succinimidyl propionate)
dV ..... concentration in a volume element
ELISA ..... enzyme-linked immunosorbent assay
ERL ..... extrisic Raman label
Fba ..... fructose-bisphosphate aldolase
F_D ..... laser spot size diameter
g ..... gravitational force
GMR ..... giant magnetoresistance
HDLs ..... high density lipoproteins
h-IgG ..... human immunoglobulin G
HIV ..... human immunodeficiency virus

J ..... flux
$J_{z,in}$ ..... flux of particles entering each volume element
$J_{z,out}$ ..... flux of particles leaving each volume element
K_S ..... sampling constant
LAM ..... lipoarabinomannan
L_D ..... lens diameter
LoD ..... limit of detection
LoQ ..... limit of quantification
LSPR ..... localized surface plasmon resonance
m ..... mass (g)
mAb ..... monoclonal antibodies
ManLAM ..... mannose-capped lipoarabinomannan
MAP ..... *Mycobacterium avium* subsp. *paratuberculosis*
n ..... index of refraction
$\boldsymbol{n}$ ..... normal unit vector
NA ..... numerical aperture
NAATs ..... nucleic acid amplification tests
NBS ..... national bureau of standards
NP ..... nanoparticle
$n_{replicate}$ ..... number of replicate samples
ODT ..... octadecanethiol
PBS ..... phosphate-buffered saline
PBST ..... 10 mM phosphate-buffered saline with 1% Tween 20
PCR ..... polymerase chain reaction
PDMS ..... poly(dimethyl siloxane)
PILAM ..... phosphor-myo-inositol-capped lipoarabinomannan
PIM ..... phosphatidylinositol mannoside anchor
PPD ..... purified protein derivative
PSA ..... prostate specific antigen
PSAs ..... point-sized adsorbates
R ..... relative standard deviation
RAM ..... random adsorption model
RIA ..... radioimmunoassay
ROC ..... receiver operating characteristic
ρ_m ..... media density
ρ_p ..... particle density
RRM ..... Raman reporter molecule
RSD ..... relative standard deviation
s ..... standard deviation
s ..... sedimentation coefficient
SEM ..... scanning electron microscopy
SERS ..... surface-enhanced Raman scattering
s_m ..... standard deviation of the method
s_m^2 ..... method variance
s_O^2 ..... overall variance
SPI ..... solid-phase immunoassay

SPR ..... surface plasmon resonance
s_s ..... standard deviation of the sample
s_s^2 ..... sample variance
SSM ..... sputum smear microscopy
t ..... time
t_0 ..... measurement at time zero
T20 ..... Tween 20
t_{24} ..... measurement at 24 hours
TB ..... tuberculosis
TSG ..... template stripped gold
TSH ..... thyroid stimulating hormone
WHO ..... world health organization
$\bar{x}$ ..... average number
α-HIgG ..... antihuman immunoglobulin G
ΔV ..... finite volume element
Δz ..... finite volume element in the z direction
λ ..... laser wavelength
v_{sed} ..... sedimentation velocity

ACKNOWLEGEMENTS

I would like to express my appreciation to all of the people that have made my graduate career a stimulating, entertaining, and unique learning experience. While nothing in life is ever exactly as you expected it to be, I have primarily fond memories of my experience. I will be forever grateful for my colleges, friends, and family that made my career and life what it is today. I would like to give special thanks to my advisor, Marc Porter, for providing me with the resources and freedom to do research that I believe will help make a positive impact on the world.

CHAPTER 1

INTRODUCTION

1.1 Overview

Early diagnosis of disease is a worldwide problem that involves the identification of a disease causing agent at the early stage of disease progression. In the preliminary stages of a disease the patient can be asymptomatic and may have low levels of disease markers readily available for detection. This can require a test that bridges the gap between a screening test, performed periodically for asymptomatic individuals, and a diagnostic test, designed to diagnose a systematic patient. The term diagnostic is, however, commonly used to describe any method for the identification of a disease causing agent. The term diagnostic test is most often used to describe both types of tests.

Detecting disease at an early stage is important in improving patient prognosis as well as reducing the spread of communicable diseases. This can improve a patients' quality of life, increase life expectancy, and/or allow for effective treatment of potentially fatal diseases. Common limitations in the utility of available testing include speed, cost, and reliability of the test. However, the implementation of new testing has additional considerations for the practicality of a diagnostic method for the region of interest and factors specific to the disease. These considerations include local resources, regional health

considerations, cost adjustments, impact of false positive/false negative results on patient heath, and safety of the working environment and training/availability of resources for the analyst.

Building on work that has previously been reported, this dissertation is an expansion on the development of a nanoparticle (NP)-based surface-enhanced Raman scattering (SERS) immunoassay for disease diagnostics. The document is organized into seven separate sections including an introduction, five original chapters, and conclusion. The introduction outlines and defines the general understanding of what constitutes an ideal diagnostic method for reliable detection of disease, as well as an introduction to the basic history and background of important topics used throughout the dissertation.

The five original research chapters that follow the introduction are as follows. Chapter 2 discusses the influence of sampling on SERS immunoassay readout in terms of accuracy and precision. Chapter 3 investigates the influence of ERL sedimentation on the reliability of the SERS immunoassay substrate during assay preparation. Chapter 4 describes the development of a SERS immunoassay for the tuberculosis (TB) marker phosphoinositol-capped lipoarabinomannan (PILAM) in buffer, synthetic urine, and serum, as well as multiplexed detection of three antigenic markers. Chapter 5 extends the methodology developed in Chapter 4 to the detection of mannose-capped (ManLAM) and a panel of patient samples from endemic areas. This dissertation concludes with general statements on the reliability of SERS-based immunoassays and speculation on the impact of the cumulative findings in the dissertation.

1.2 An "Ideal" Diagnostic Method

A diagnostic test is a medical test designed to detect the presence of disease in a host.[1-4] This is typically performed through the detection of a "marker" that is present in the host due to the existence of disease. Diagnostic test results give the medical professional the information required to take the next step for a patient, be it additional testing or a treatment plan. The primary components of a diagnostic test are a reliable disease marker, recognition element, and detectable label. It is also important to know that a diagnostic test is not inherently useful on its own. A test may require additional sample handling, preservation, and sample treatment to provide reliable results. The entire process for the identification of a disease-causing agent in a patient sample is called the diagnostic method. The validity of the diagnostic method is based on the ability to accurately predict the presence of disease in large sets of patient samples. The performance of a diagnostic test is typically determined by the percentage of patient samples that have a true positive (clinical sensitivity) and a true negative (clinical specificity) results compared to the best available method. In order to visualize the difference between multiple sample sets a receiver operating characteristic (ROC) curve can be used.[5] The ROC curve was developed as a statistical method to visually represent binary systems. In the case of a diagnostic method, the classifiers for true positive and true negative rates can the strength of the method.[6] Example ROC curves are illustrated in Figure 1.1 and indicate the potential differences in the performance of diagnostic methods. An ideal method has a vertical segment of the line at 0% false positives and then a horizontal segment of the line at 100% true positives. This represents a method with 100% sensitivity and 100% specificity. A straight line from the lower left to the upper right portion of the graph indicates no

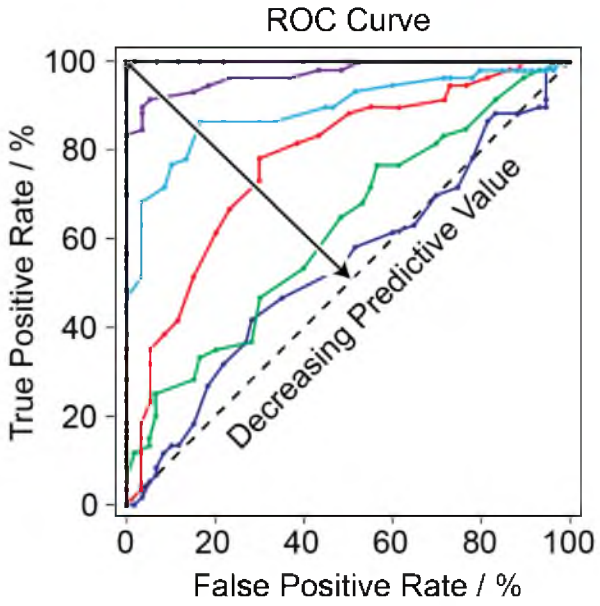

Figure 1.1. Biomedical ROC curve displaying the difference from diagnostic methods. The ROC curve displays the results from diagnostic analysis of patient samples with a known disease status as the true positive rate versus the false positive rates. The position of the segmented line represents the overall performance of the diagnostic method and shows where there is a tradeoff between true positives and false positives. The overall predictive value of the method is displayed from the ideal method in black, to decreasing values from purple, blue, red, green, violet, and finally no predictive value for the dashed line. Each point represents the progression of the ROC curve based on the results of a patient sample.

diagnostic value. Most methods display a stepped line representing the performance of the method on patient samples and visually indicating the ability of the test to distinguish between positive and negative samples.

While there is always a push for improvement in terms of sensitivity and specificity for early diagnostics, the access to methods available in well developed countries is remarkable. There are redundancies in many of the testing options which increases the probability of accurate diagnosis. When one diagnostic method lacks specific aspects of ideal performance there are additional options available.[7] This stems from the availability of resources that produce core facilities outfitted with expensive equipment, highly trained professions, and a communal infrastructure that allows for rapid transport and communication. Patient samples can be shipped and processed by highly qualified facilities and results available with minimal turnaround times, often without consideration to the expense. Considering the number of resources that comprise medical diagnostics in well-developed countries, it is good to keep in mind the global problem that persists and requirements that prohibit the use of currently available methods. The need for new diagnostic methods is highlighted by a list of the top 12 causes of death worldwide in 2008 (Table 1.1). [8] Of the top 12 causes of death on the list only two are nondisease related and rank in the 10th and 12th positions, demonstrating the global hardship of disease.

High profile and high-risk diseases most easily display the need for readily available diagnostic methods that can help reduce the spread of the diseases as well as improve patient prognosis. Global health scares such as the one associated with the 2014 Ebola outbreak in Western Africa[9, 10] are harsh reminders of the potential catastrophic threat of highly communicable and deadly diseases. Fortunately, only a few diseases

Table 1.1. Leading causes of death worldwide in 2008.[8]

Rank	Description	Estimated number of deaths ($\times 10^6$)	Percent of all deaths
1	Ischemic heart disease	7.25	12.8
2	Cerebrovascular disease	6.15	10.8
3	Lower respiratory infections	3.46	6.1
4	Chronic obstructive pulmonary disease	3.28	5.8
5	Diarrheal diseases	2.46	4.3
6	HIV/AIDS	1.78	3.1
7	Trachea, bronchus, lung cancers	1.39	2.4
8	Tuberculosis	1.34	2.4
9	Diabetes mellitus	1.26	2.2
10	Road traffic accidents	1.21	2.1
11	Hypertensive heart disease	1.15	2.0
12	Prematurity and low birth weight	1.00	1.8

display similar fast-acting development along with the high mortality rate exhibited by Ebola. However, preventable and treatable infectious diseases still have a high impact in low-resource regions with reduced hygiene standards that enable the continual spread of communicable diseases. In these regions the availability, access, and reliability of detection methods play a major role in the number of people that actively seek out diagnostic testing. The effectiveness of a diagnostic method is therefore primarily related to the monetary and time costs associated with testing.

There are, however, necessary components for a diagnostic test to be applicable in any region of the world. It is easy to define an ideal diagnostic method as rapid, cost effective, and reliable,[11] but the utility also depends on the burden associated with testing. This requires taking into account all socioeconomic factors that increase the number of constraints used for development. Each community has different requirements for the cost, resources, and complexity that a diagnostic method requires. In well-developed regions, a glucose sensor for diabetes is an example of a widely available and simplistic diagnostic tool. However, some low-resource regions must combat problems associated with the lack of clean needles, electrical power, and individuals with the proper education to perform testing and interpret results. While it at times seems impossible to meet all these qualifications, by working as a scientific community small improvements can potentially be combined to an eventual solution.

Regional restrictions can also be compounded by unique characteristics of a disease. A high impact example for the global need for improved diagnostic methods with unique requirements is the detection of tuberculosis (TB) infection. Tuberculosis, while commonly considered a disease of the past in well-developed regions, persists as the

world's second greatest killer due to a single infectious agent. TB is second only to human immunodeficiency virus (HIV)/acquired immune deficiency syndrome (AIDS).[12, 13] Caused by the bacillus *Mycobacterium tuberculosis* (*M. tuberculosis*) TB is a preventable and curable disease but has specifically adapted to evade eradication attempts.

The high threat of TB infection to patients in regions of Asia and Africa is due to a combination of hygiene standards, coinfection with immune suppressing diseases, and limited resources. While simple skin testing is commonly used in the United States, this test can be rendered inaccurate due to coinfection with immune suppressing diseases. The test is based on the presence of antibodies to TB in the host. False negatives are caused immunocompromised hosts not producing antibodies and false positives by a patient's exposure to *M. tuberculosis* without infection. Due to this limitation, current diagnosis methods in high-burden regions primarily depend on sputum smear microscopy (SSM) and commercially available serological tests.[14] However, the World Health Organization (WHO) has recently issued a policy urging resource-limited countries to ban these serological tests. The alarmingly high inaccuracy of serological tests that results in negative impact on the patients' health leaves SSM as the primary available test. SSM requires an advanced stage of pulmonary disease for detection.

The global problem of TB testing is a reasonable model system that can be used to test the reliability and accuracy of new diagnostic methods. The ability to develop a diagnostic that can meet all the requirements outlined by the problems associated with TB diagnostics would fill a large void in the currently available diagnostic technologies. The adaptation of a SERS-based immunoassay towards the development of a rapid, low-cost, and reliable detection method for immune compromised patients is a focus of discussion

for this dissertation. The system also has the benefits of robust low-tech detection of the antigenic TB marker ManLAM (shown in Figure 1.2).[15-18]

1.3 Data Acquisition and Sampling

The development of any new analytical method requires the consideration of the potential impact of sampling on the results.[19-21] Often times, measuring an entire population is impractical, due to the time and expense of assessing a potentially excessively large population. In many cases a small portion of the whole population, a sample, is tested and results are considered to represent the population. A sample can refer to multiple processes during analysis and should always be considered. While some populations are inherently homogenous (e.g., a uniformly colored solution), while not all populations are (e.g., a soil sample). Problems with sampling arise when the sample does not accurately represent the population. This can occur due to undersampling which leads to statistically inaccurate results due to the sample dispersity relative to the sample size. This is visually depicted in Figure 1.3 where two populations and samples of equal size display distinctly different distributions. The populations and sample sizes are equal, but Figure 1.3a sampling displays representative results while Figure 1.3b sampling is nonrepresentative of the true population.

Typically a sampling problem originates when a researcher is under the assumption that an analyte of interest is evenly dispersed at a high enough concentration within the sample to accurately represent the entire population. However, when a sample size is too small to contain the analyte of interest at a statistically relevant level, there is a high probability the result will not match the population. There should also be consideration as

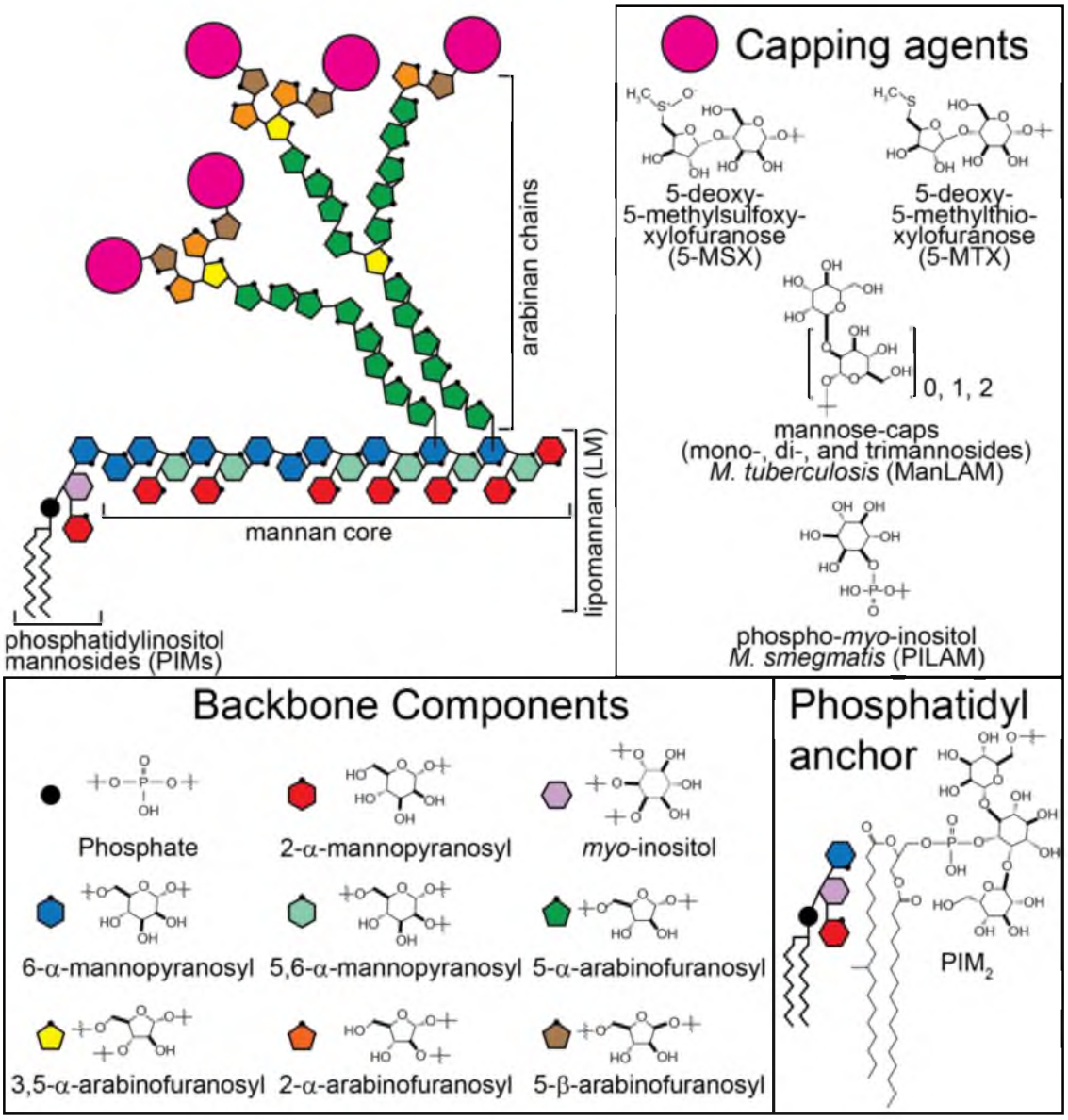

Figure 1.2. Structure of LAM, represented as the four primary components: phosphatidylinositol mannoside (PIM) anchor, mannan core, arabinan chains, and capping agents. The length and number of branches of the mannan core and arabinan chains are fewer than those found in nature. Phosphor-*myo*-inositol-caps produce PILAM and mannose-caps produce ManLAM.

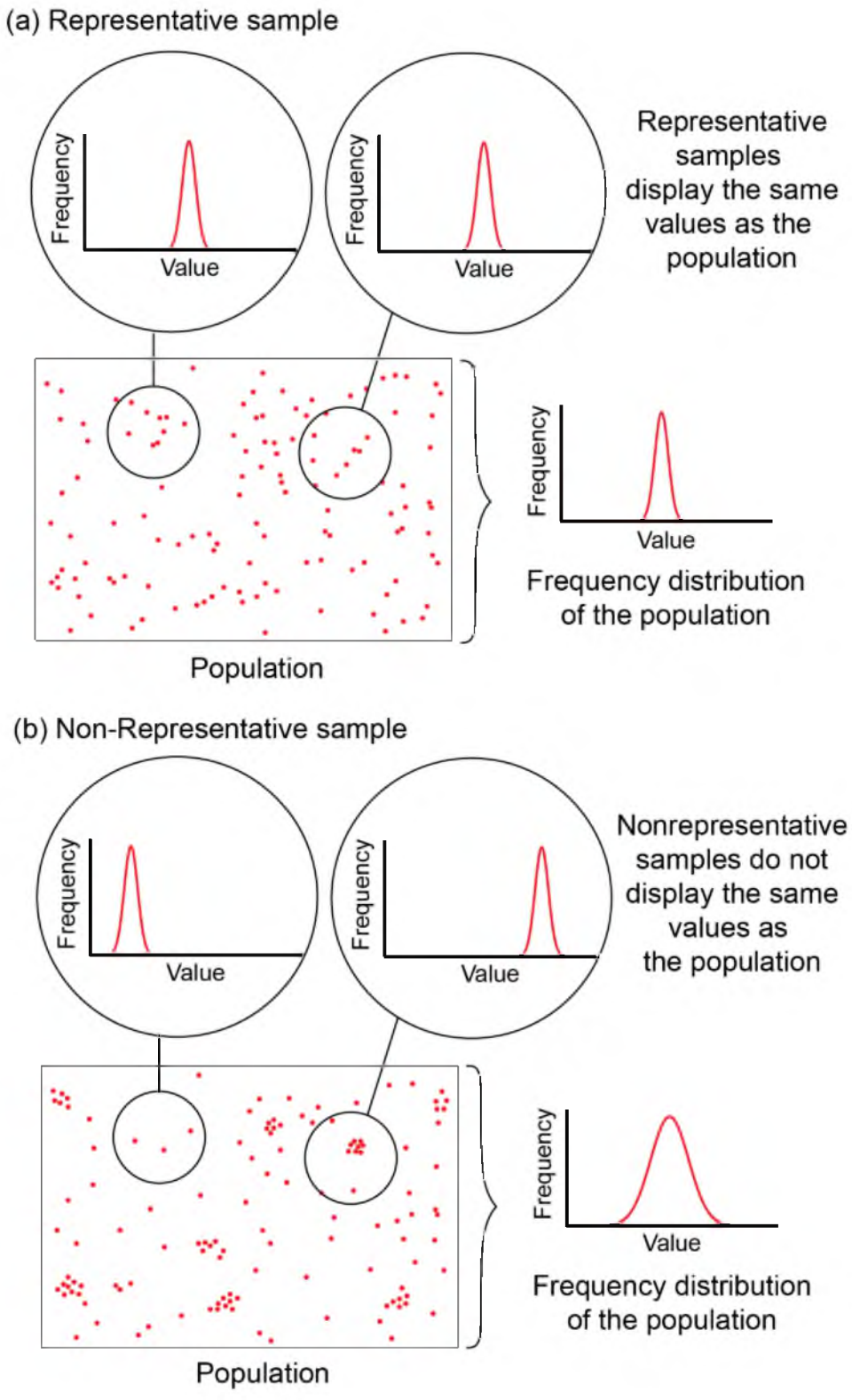

Figure 1.3. Visual representation of (a) representative and (b) nonrepresentative sampling. Sampling can dictate the accuracy and precision of the final result which can potentially misrepresent the population.

to whether the sample size accounts for heterogeneity within in the sample. The accuracy and precision of sample size is dependent on the heterogeneity of the sample.

Sampling can occur during several different points in an experiment. Typically sampling occurs when an aliquot of a bulk material is taken for analysis. When this is done there are multiple potential sources of error, including techniques used for sample collection, storage, processing, preservation, and preparation. There can also be a problem associated when the analysis method that only measures a portion of the prepared sample. Sampling of material during the analysis step can be of equal importance. If the use of an analysis method is adapted for a new technique, the impact of the setup on the results should be examined.

High-resolution data collection performed with small analysis areas can be used to display the distribution of an analyte within a sample. This type of high-resolution data collection is very useful but is designed to inherently indicate minor deviations in analyte concentration. This technique is counterproductive if the goal of analysis is to determine the mean or true value for the population. In this case the sampling size should be large enough to statistically display an accurate and precise result for the system. Minor errors associated with sampling can be accounted for with blanks, standards, and reference samples. However, options are limited if the sample measured is nonrepresentative. Methods are available to determine the source of error present in the analysis.

Inherent errors are present in any sample preparation and analysis method. These errors can lead to deviations from expected values as well as variations in signal. Small variations in signal and their relation to the true value are described by the accuracy and precision. The precision of the result associated with the measurement can be described by

the relative variance associated with the method (s_m^2) and the relative variance that is present due to the sample (s_s^2). In order to separate which portion of the error is present due to the method versus the sample, the overall variance (s_O^2) is determined by the variance in the measured readout.[22, 23] The difference of between the s_O^2 and s_m^2 give the variance that is directly related to the sample which is described by the following.[24]

$$s_O^2 = s_m^2 + s_s^2 \tag{1.1}$$

This equation shows that the overall variance of a measurement is either limited by the sampling error or by the error of the method and can be rewritten to encompass a variety of known sources of error. From Equation 1.1 determination of the primary source of error can be determined as coming from either the s_m^2 or s_s^2. Depending on the primary source of error, it can be determined if replicate measurements will or will not improve the quality of the result. When s_m^2 is larger than s_s^2, replicate measurements are not beneficial to the analysis.

Youden explained the ratio of the standard deviations $\frac{s_s}{s_m}$ indicates the percentage of s_O^2 that is present due to the different components.[25] If s_s is three times as large as s_m then only 10% of the variance comes from the method. The graphical representation of this calculation, shown in Figure 1.4, displays the law of diminishing returns for the benefits of improving the method when the error in the sample is larger than that in the method. The analysis also indicates that low-quality samples can limit the ability of a method to display precise measurements. There is also a question about what the optimum sample size should be to produce an accurate analysis. A common example of this type of sampling problem

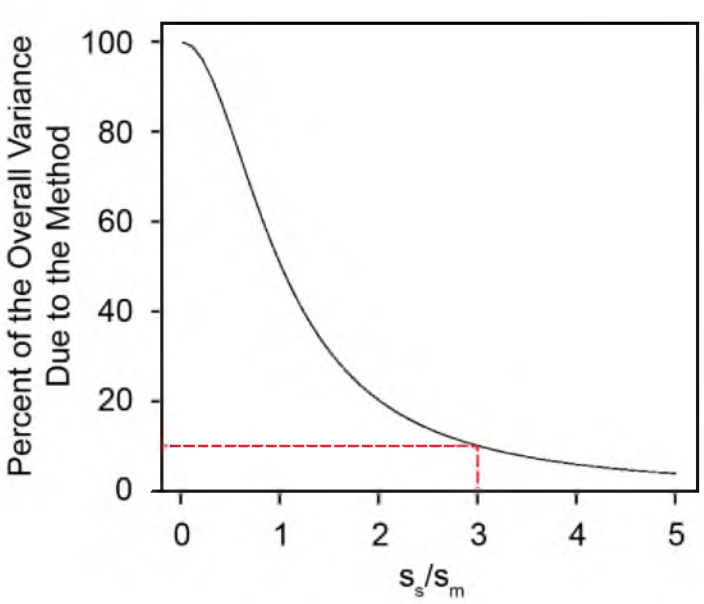

Figure 1.4. Relationship between the contribution of variance in the method to the overall variance versus the ratio of the standard deviation of the sample (s_s) to the standard deviation of the method (s_m). The red dashed line represents that when the variance of the sample is three times higher than the variance for the method, the overall contribution of the error from the method is only 10%.[25]

is a solid sample that is composed of two or more components with an analyte of interest in low quantities. In this type of sample there is a question of how much sample should be analyzed to ensure that the results will display an accurate level of the analyte of interest. The sample size then dictates the accuracy and precision of the results. The sample taken from the bulk has to be sufficiently large to contain a statistically relevant amount of the analyte to accurately measure the concentration of the material.

Several methods to estimate the amount of a sample needed to exceed a predetermined level of uncertainty have been previously addressed. Ingamells determined a relationship between the decreases in the error associated with a measurement of a sample and increasing the sample size.[26] The relation:

$$mR^2 = K_S \tag{1.2}$$

where m represents the amount of sample analyzed (g), R is the relative standard deviation of the sample (%), and K_S is the sampling constant or the sample mass required for 1% R (g). The sampling constant represents the amount of the sample that is required to limit the sampling uncertainty to 1% with 68% confidence. This method can be used to estimate the mass of a sample needed for a given R.

One of the most well-known examples of this method was used for determining the sodium content of liver samples via radiotracing of ^{24}Na.[27] The analysis was used to evaluate specimen collection, processing, storage, and analysis for the National Bureau of Standards (NBS). The study required a small portion of the liver specimens to be analyzed from a stored specimen. Variability in the result for the content of ^{24}Na in a liver sample

was demonstrated to be dependent on the sample size. This is to ensure that variations in the result were due to specimen collection, processing, and storage. The results of the sampling experiments are shown in Figure 1.5; they clearly show decrease in signal variability with increased sample size. The K_S for the sample type was calculated as 35 g.

1.4 Raman Laser Spot Size Diameter

Raman instrumentation commonly consists of an excitation source, spectrograph, and fiber optic probe. The area of the surface, which defines the sample size, that is, analyzed by a Raman instrument is based on the excitation area defined by a focused laser spot.[28] While the true laser spot is not always circular and the laser strength follows a Gaussian distribution, a circular area on the surface is a reasonable estimation of the sample size. The spot size and signal collection efficiency are both, in large part, determined by the objective. The numerical aperture (NA) for an objective indicates the relative laser spot size and collection efficiency, which are inversely proportional to each other. From this relationship, we see that a smaller laser spot size has a higher collection efficiently or signal. When selecting an objective for quantitative analysis, the analysis area should be large enough to properly represent the sample.

The laser spot size diameter is dependent on the laser wavelength, incident beam diameter, and the NA of the objective displayed in Figure 1.6. The focused spot size can be estimated by Equation 1.3

$$F_D = \frac{n \lambda L_D}{NA\, B_D} \tag{1.3}$$

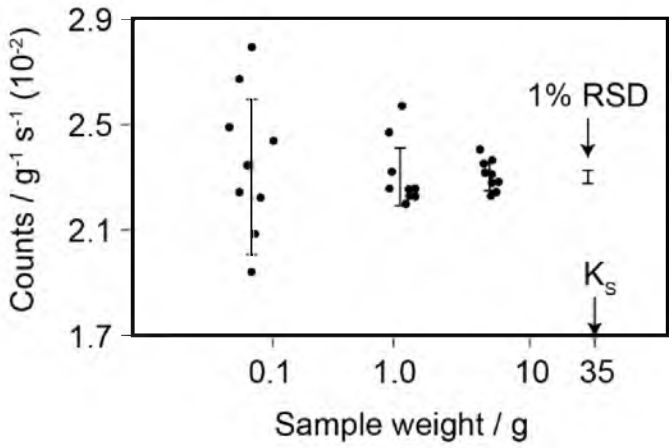

Figure 1.5. Sampling diagram for sodium-24 counts of homogenous human liver samples. (Adapted from reference "The Sampling and Analysis of Human Livers.")[27]

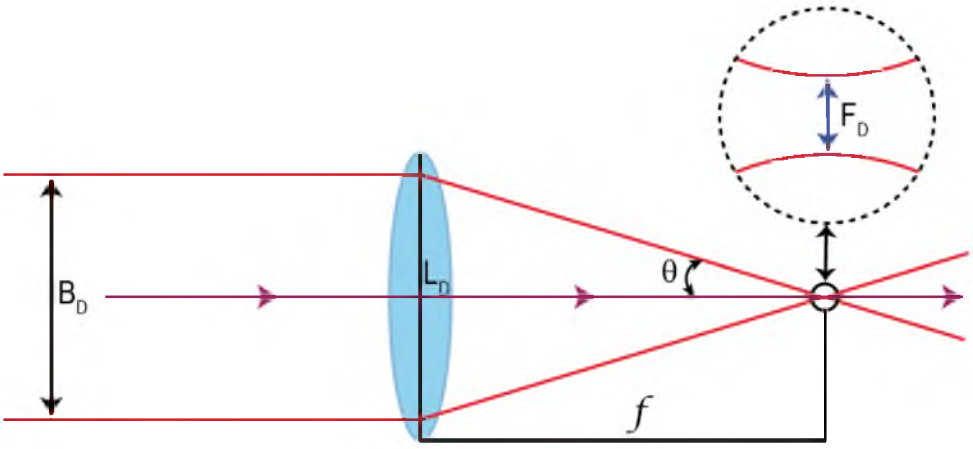

Figure 1.6. Visual representation of the diameter of the laser spot size produced by an incident beam focused through a lens.

where, F_D is the laser spot size diameter, n is the index of refraction, λ is the laser wavelength, L_D is the lens diameter, and B_D is the incident beam diameter. The equation indicates that as the NA is increased the F_D decreases, thus reducing the laser spot size. A larger NA is desired for analysis of many SERS-active substrates due to the increased collection efficiency, which can aid in lowering detection limits. However, based on Equation 1.2, there is also an inherent decrease in sampling size. An objective that is sometimes in SERS analysis is a 50x Olympus,[29, 30] which produces an F_D of ~0.5 μm or analyses area of 0.79 μm^2. In comparison to a 3.0 mm area the area analyzed would be a ratio of 1.1×10^{-7} of the surface, resulting in the measurement of an exceptionally small portion of the overall sample.

1.5 Immunoassay Development

The beginning of modern diagnostic tests began in the 1940s with colorimetric detection of enzymes and metabolites in biological fluids.[31] These experiments confirmed that biological components of bodily fluids contained molecules indicative of disease. The concept led to deployment of an immunoassay performed by Landsteiner in 1945 which demonstrated that small molecules (haptens) could illicit an immune response when conjugated to larger carrier molecules.[32] The use of antibodies produced by a host increased the sensitivity of diagnostic platforms acting as recognition elements for the targeted marker.[33]

The first successful use of an immunoassay was developed by Yalow and Berson in the late 1950s.[34] This radioimmunoassay (RIA) used a known quantity of ^{131}I-labeled insulin (labeled antigen) which was exposed to a known quantity tracer antibody. After a

set incubation period, the labeled antigen was bound to the tracer antibody at equilibrium quantities in the solution. A patient sample was then added to the solution and the free antigen in solution competed to bind to the tracer antibody, changing the equilibrium of the solution. The ratio of free-to-bound labeled antigen was directly proportional to the amount of free antigen in a patient sample. This procedure is known as a competitive immunoassay that requires separation of the bound and free labeled antigen in solution for analysis. While many different techniques have been used for the separation of the free and bound materials, all are time consuming and cumbersome. Despite these drawbacks, the RIA was introduced into the diagnostic market in the late 1960s[35] and the developers were awarded the Nobel Prize in Physiology or Medicine in 1977 for the breakthrough in diagnostics.

The solid-phase immunoassay (SPI) as shown in Figure 1.7 was developed by Catt and Tregear in the late 1960s; it increased the sensitivity and reduced costs of diagnostics.[36] The SPI immobilized capture antibodies on a solid interface. The surface was then exposed to a solution or patient sample containing the homologous antigen, and was extracted from solution and immobilized on the surface, allowing the excess solution to be rinsed away. This provided a reasonable alternative to the cumbersome separation techniques used by RIA. The success of basic SPI detection methods has been widespread with techniques that include radioactive isotopes, enzymes, fluorophores, electrochemistry, and chemiluminescent labels; many of these methods are still currently in use. [37-41]

One of the largest advancements in immunoassays was the introduction of enzymes in the 1970s as alternative radioisotope labels.[42, 43] The use of enzymes produced one of the most widely used immunoassay techniques: the enzyme-linked immunosorbant assay

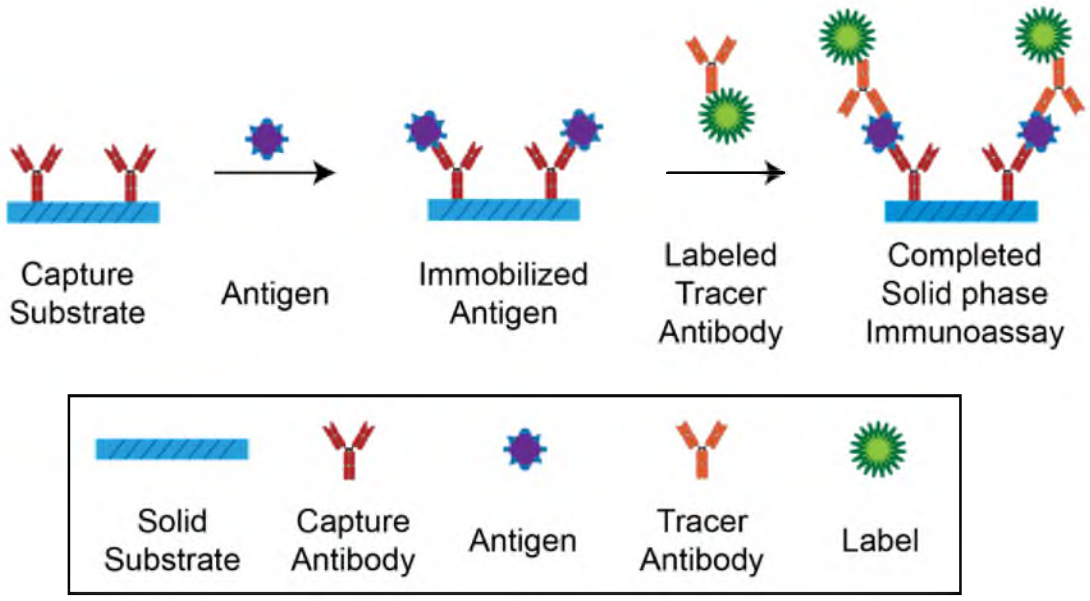

Figure 1.7. Basic solid-phase sandwich immunoassay format.

(ELISA).[37] The success of ELISA is based on the inherent ability of the enzyme to increase the rate of a chemical reaction, thus increasing the signal output with time. The enzyme is conjugated with a tracer antibody and used to locate the antigen immobilized in a SPI. The reaction vessel is then filled with substrate and the product of the enzyme-substrate reaction can be detected with a large variety of methods including visual assessment, colorimetry, fluorimetry, luminometry, or electrometry.[37, 44-47]

While the development of ELISA has to be the most notable advancement in SPI technology, there are still drawbacks to the technique that have prompted the development of new detection methods. Some problems associated with enzymes used for immunoassay are associated with the environmental sensitivity of the enzyme. Changes in the environmental conditions surrounding the enzyme such as pH, ionic strength, and temperature can cause fluctuations in the activity of the enzyme. Conjugation techniques used to attach the enzyme to the recognition element can cause localized denaturation or conformational changes which also impede the enzyme activity. The physical properties and structure of the enzyme also allow the adsorption to surfaces used in SPIs. There is also an inherent complication in multiplexing capabilities of enzyme-based detection. The challenge lies in the ability to find multiple enzymes that will produce unique and reliable readout without any interactions between the enzymes and the substrates.[48]

The demand for diagnostic methods to have increased speed, sensitivity, lower detection limits, and higher throughput have helped broaden the potential tools available. Technological advancements in detection methods and instrumentation has produced several novel techniques including surface plasmon resonance,[49-56] quantum dots,[57-65] giant magnetoresistance[66, 67] and surface-enhanced Raman scattering,[68-88] to name a few. Each

of these techniques, displays great potential for the progression of diagnostic technologies with immunoassay having many applications for use in clinical,[89, 90] environmental,[91] and agricultural diagnostics.[92, 93]

1.6 Raman Spectroscopy and Surface -enhanced Raman Scattering

Raman spectroscopy is a vibrational spectroscopy technique discovered in 1928 by Sir Chandrasekhara Venkata Raman.[94, 95] Raman signal is produced when an incident photon causes molecular vibrations that influence the polarizable electron density and inelastic scattering. While, a majority of scattered light, has a conserved frequency, Rayleigh scattering, the inelastic scattered light is shifted in frequency due to a gain or loss in energy. The gain or loss of energy is described as anti-Stokes and Stokes shifts, respectively. The change in energy is equal to the transition of an energy state producing a molecular fingerprint of the molecule. The Stokes shifts have higher signal intensity than the anti-Stokes intensity due to the higher probability of energy loss versus an energy gain. Modern instrumentation uses a laser to provide a simple and powerful excitation source, and a long pass filter removes the signal from Rayleigh scattering and anti-Stokes lines. The resulting Raman vibrational spectrum is dispersed by a grating and the resulting spectrum is detected with a charge couple device (CCD). The final result is plotted as the signal intensity in counts per unit time versus the Raman shift in wavenumber relative to the excitation source.

Raman spectroscopy is rich with vibrational information. However, the signal is inherently weak produced by only 1 in 10^6 incident photons and not all molecules are Raman active. Historically the weak signals associated with Raman spectroscopy have

limited the use of the technique. The invention of lasers in the 1960s[96] and the discovery of surface-enhanced Raman scattering (SERS) in the 1970s renewed interest in the field of Raman spectroscopy.[97-99] Both scientific advancements were paramount to overcoming some of the shortcomings of Raman spectroscopy.

SERS displayed significant increases in the Raman signal produced by Raman-active molecules adsorbed to a roughened metal surface. Surface enhancement factors have been reliably measured to be on the order of 10^6 to 10^8,[100-112] with sensitivity demonstrating single molecule detection.[113-116] The early success of SERS detection and subsequent promises made about the potential of the technique are based primarily based on the increased level of sensitivity provided by SERS over traditional Raman. However, the success has also been surrounded by debate over the enhancement mechanism, reproducibility of the signal strength, and reliability of the method as a quantifiable detection platform.

The SERS effect was originally achieved when Raman-active molecules were adsorbed on a roughened coinage metal surface.[97-99, 117, 118] The original discovery of SERS found that the signal enhancement was produced by the increase in the number of adsorbed molecules on the roughened surface.[97] The proper identification of the active role of the surface in signal enhancement and the true beginning of SERS was the discovery by Albrecht and Crieghton as a chemical effect [98] and Jeanmaire and Van Duyne as an electromagnetic effect,[99] in 1977. The initial false interpretation and subsequent two surface theories lead to confusion in the field as to the true mechanism for SERS enhancement.

Since that time, defining the mechanisms of the signal enhancement has been a

difficult and long process with highly complex mathematical and theoretical explanations.[100, 117, 118] The scientific community developed theories based on early reports and determined that the enhancement mechanism was a combination of chemical and electromagnetic enhancement factors. The chemical enhancement theory, accepted as the lesser of the two sources of the effect, is attributed to a resonant charge-transfer state between the adsorbed Raman-active molecule and substrate.[119-121] On the other hand, the electromagnetic theory, considered the predominant source of the effect, is consistent with the observed experimental dependence of the roughness and dielectric properties of the SERS substrate.[100, 101, 103, 110, 122-124] The electromagnetic enhancements contributes to the signal through the production of a localized surface plasmon resonance (LSPR), as displayed in Figure 1.8. Coinage metal materials (copper, silver, and gold) are the most commonly used substrates for the production of SERS substrate. Incident photons, on a similar order of magnitude as the size of the metal features, cause a collective oscillation of the conduction electrons producing LSPR which can be tuned to maximum enhancement of surfaces with uniform roughness features. The enhancement displayed by SERS has been attributed to both mechanisms, but with unequal contributions to the overall signal enhancement. The chemical component is generally believed to be responsible for 10 to 100 enhancement factors and the electromagnetic component is thought to be responsible for enhancement factors of 10^5 to 10^6.[100-112]

While the majority of the enhancement in SERS originates from the large LSPR from nanometer-sized asperities the conduction of electrons in the bulk smooth films producing a surface plasmon resonance (SPR) can also contribute to the enhancement.[125-132] The AuNPs therefore interact with the gold substrate in a similar fashion as interparticle

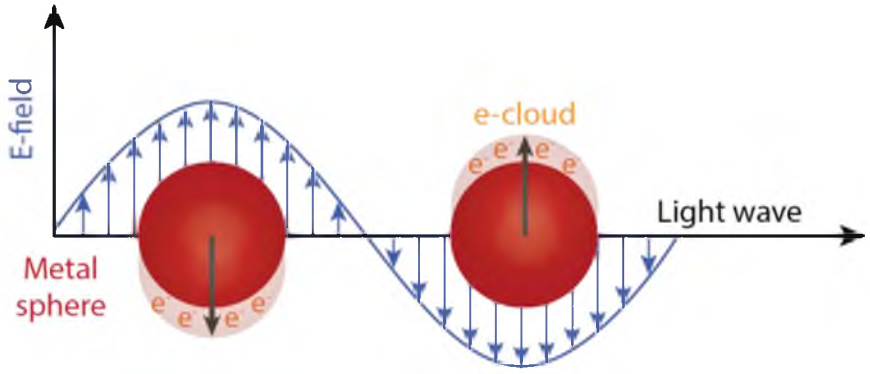

Figure 1.8. Illustration of a localized surface plasmon resonance of a metal sphere. The incident electric field component of a light source causes the collective oscillation of the conduction electron cloud.

interactions. The theoretical calculations indicate that the LSPR and SPR are dependent on the NP-substrate spacing in addition to the size, shape, composition, and dielectric constant of the materials involved.[132-134] By isolation Raman labeled AuNPs on a gold substrate which increases enhancement reproducibility but reduces the overall signal enhancement that is achievable. However, fine tuning of the components of the assay.

SERS is therefore in the category of highly sensitive readout methods that can be used in detection platforms. The advantages to using SERS as a detection method is based on several inherent and beneficial attributes of Raman spectroscopy.[68-83] The most important attribute of SERS detection is the simplicity and cost-effective production of currently available Raman instrumentation. The simplistic design, fast readout, and decrease in cost of more reliable components now sees Raman instrumentation that are available for ~$7,000 or more.

SERS also displays signal intensities comparable to those of fluorescence. However, compared to fluorescence, Raman bands are much narrower. The narrow bands reduce the likelihood of spectral overlap from multiple labels, which is beneficial in a multiplexed assay detection.[87] This is due to the excitation being dictated by the enhancing substrate rather than the scattering molecule, allowing for a single excitation source. Plasmonics of the system also allow for red-shifted excitation, reducing natural fluorescence produced by biological materials that can cause background interference. Raman scattering is unaffected by its surrounding environment (e.g., pH, ionic strength, quenchers) resulting in a more stable and reproducible signal and long-term sample storage. This helps the Raman active molecules be more photostable due to the extremely short liftetime of the excited state.

1.7 Nanoparticle-based SERS Sandwich Immunoassay

Historically, SERS substrates were electrochemically roughened silver substrates. The production method produced a roughened substrate that was not easily controlled on the nanometer scale, and thus these substrates were considered irreproducible from a production stand point. Recent developments in the controlled production of nanoparticles (NPs) with specified sizes and shapes[135] in combination with smooth substrates allows for a simplified approach to the fabrication of nanometrically roughened substrates.[70, 136] NPs in colloidal suspension have added benefits produced by the conjunction of the NPs with smooth substrates.[132, 136, 137] NPs immobilized on smooth metallic surface are straightforward constructions of a nanometrically roughened surface with consistent shape of the features. Hybridization of the plasmon created by the NP and the surface also increase the observed enhancement.[138] The SERS signal enhancement has been demonstrated to have a dependence on the distance between the NP and the surface,[139] size of the NP,[140] angle of incidence,[141] dielectric properties of the medium,[141, 142] and composition material of the NP and surface.[143, 144] The enhancement is considered to be produced primarily in the nanometeric region next to the NP between the NP and the surface creating a small "hot spot" or "hot junction" when the Raman active molecule is within a few nanometers of the NP surface.[145]

Before the introduction of the first NP-based SERS sandwich immunoassay, there were several attempts to create a SERS immunoassay. The first SERS sandwich immunoassay was demonstrated by Rohr and collaborators using a roughened silver surface coated with a capture antibody and was used to immobilize thyroid stimulating hormone (TSH).[73] TSH was then labeled with a tracer antibody covalently coupled to p-

dimethylaminoazobenzene (DAB), a Raman resonance dye. Another developmental step by Dou and collaborators was the demonstration of an enzyme and silver NP-based immunoassay.[72] The detection of mouse IgG was performed using a basic ELISA platform in which the resulting product of the enzyme-substrate reaction was Raman active. The azo compound produced by the substrate reaction was removed and spontaneously adsorbed on silver colloids for solution-based analysis. The work of Zhang and collaborators successfully developed a label-free SERS platform for an anthrax biomarker.[76] That work described the release of the biomarker calcium dipicolinate (CaDPA) via sonication in nitric acid and subsequent adsorption onto a silver film coating a nanoshere. The method demonstrated the usefulness of the system via the identification of Raman active biomarkers.

The Porter laboratory developed the first NP-based SERS sandwich immunoassay that has been used for a variety of disease markers, as shown in Figure 1.9.[69, 70, 84-88]. Our format is based on a sandwich immunoassay platform, and uses SERS as a detection method. The platform includes antigen selectively via the incorporation of a selective and Raman-active extrinsic Raman label (ERL) and capture antibodies bound to an atomically smooth gold capture substrate. The ERL consists of 60-nm gold nanoparticle (AuNP) with a Raman label chemisorbed to the surface, followed by a layer of tracer antibody. The antigen is sandwiched between a smooth gold substrate and an AuNP maximizing the enhancement of the SERS substrate and producing a quantifiable signal based on the number of ERLs adsorbed to the substrate. Of the many types of SERS-based platforms that have demonstrated the NP-based sandwich immunoassay, it is one of the most extensible and applicable in terms of analyte detection.

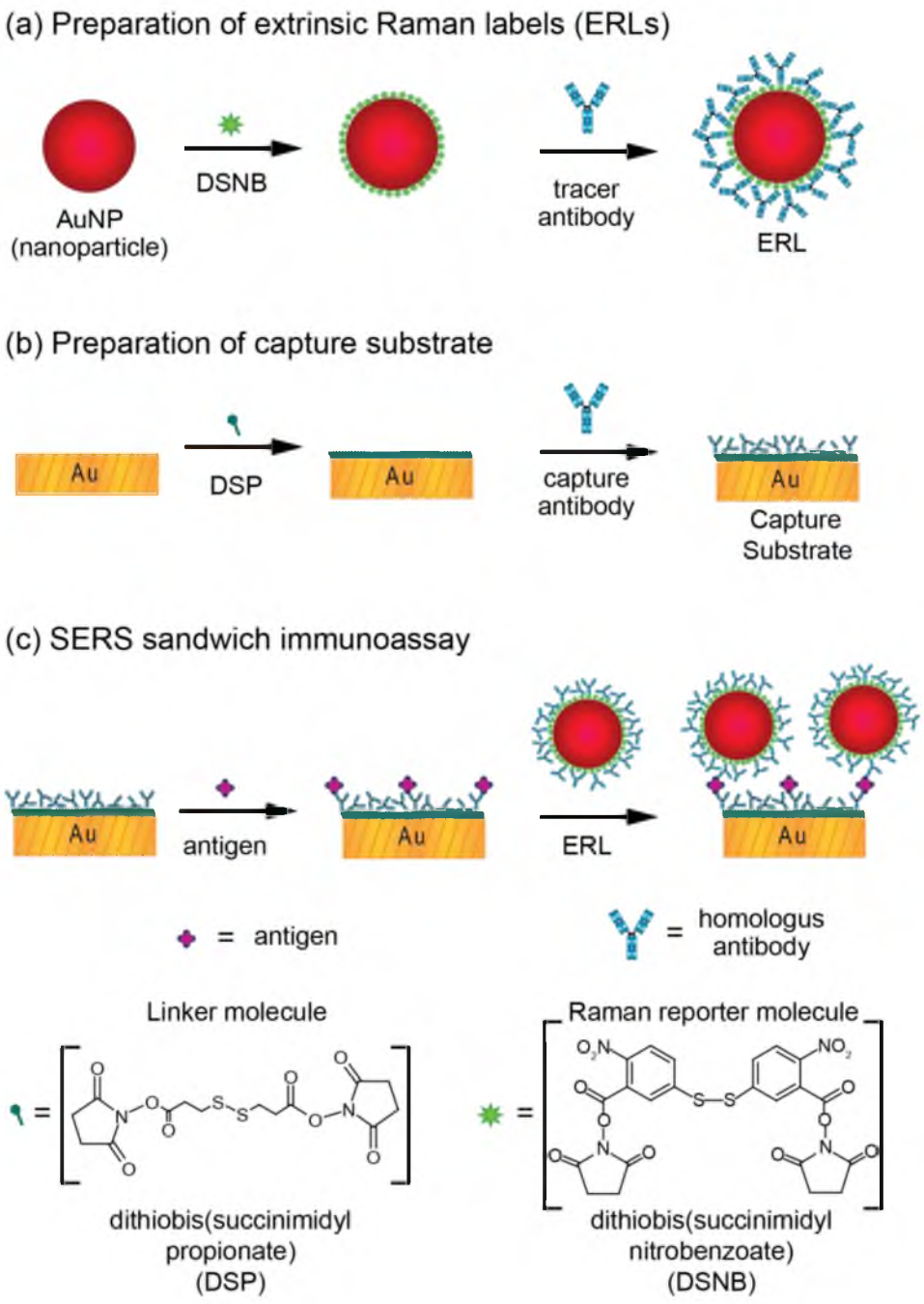

Figure 1.9. The three main components of the SERS-based immunoassay: (a) ERL preparation; (b) capture substrate preparation; and (c) assay steps. The ERLs are prepared with AuNP core modified with a Raman reporter molecule and tracer antibody. The capture substrate is prepared by chemisorption of a linker molecule and immobilization of the capture antibody. Preparation of the ERLs and capture substrate are carried out prior to the assay. The capture substrate is exposed to the antigen solution and subsequently to the ERLs are added to complete the NP-based SERS immunoassay.

The ability to quantitatively measure the number of antigens in a solution is based on the sandwich immunoassay design. In the sandwich immunoassay the antigen is immobilized by a capture substrate and subsequently labeled by a tracer antibody modified for detection. In the performance of an ideal SERS sandwich immunoassay, this indicates that each bound ERL is indicative of a bound antigen. ERL can then be used as a measure of the number of antigens in solution. However, for SERS to be a reliable and quantitative detection tool, the signal from each of the ERLs bound on the surface should provide the similar quantity of signal. It is known that SERS enhancement is increased for large aggregates of NPs.[146, 147] Due to the complexity of the mechanism behind SERS signal enhancement, more simplistic systems, such as the influence based on the interaction of two particles, has been studied.[110, 111, 125-132] The plasmon behavior of NP pairs is different from individual particles, causing shifts in the position of the LSPR and influencing the strength of enhancement.[11, 102, 110, 113-132, 134] While the increased signal enhancement of paired NP is an advantage in terms of sensitivity, it is undesirable for quantitative analysis unless the dimer formation can be strictly controlled. Controlled aggregation of particles is difficult to achieve. The demonstration of individual particles having detectable signal indicates that the use of aggregated particles is not entirely necessary.[71] An ideal surface for SERS-based immunoassay has minimal ERL interactions to ensure a linear signal increase with increasing ERL densities. The spacing of the particles only needs to be on the order of ~100 nm, or just over the diameter of the particle, with reports stating most interactions occur within a one-diameter distance relative to the NP size.[122, 123, 148, 149]

The SERS immunoassay platform developed in the Porter laboratory has successfully demonstrated many of the advantages of SERS detection. The assay first

demonstrated the ability to achieve low limits of detection (LoDs) of prostate specific antigen (PSA) in the femtomolar range. The detection of femtomolar concentrations of PSA was achieved with a cost-effective Raman instrument; the most expensive assay element was the biological recognition elements.[70] This design has also been applied multiplexed detection to the simultaneous detection of rabbit, human, and mouse IgG proteins.[71, 87] Development of methods for decreased assay times to decreases turn-around times via increased flux to the SERS-based immunoassay substrate.[150] The extensibility and adaptability of the SERS-based immunoassay also allows for the detection of different antigens[70, 84-86, 88] and demonstration of fundamental applications.[71, 86, 87, 115, 151]

1.8 Nanoparticle Transport

In a colloidal suspension NPs are normally considered to move in solution based on Brownian motion.[152] Brownian motion occurs due to the collisions between the particles and the fast moving atoms or molecules in the suspending fluid. The movement of the particles is also considered to be based on diffusional transport, which is dependent on the size of the particle, temperature, and media viscosity. A diffusion coefficient for a spherical NP suspended in solution can be calculated with the Stokes-Einstein equation for diffusivity, given by:

$$D = \frac{k_B T}{6\pi\eta r} \tag{1.4}$$

where k_B is Boltzman constant (1.3807×10^{-23} J K^{-1}), T is the temperature (K), η is the viscosity of the suspending fluid (kg m^{-1} s^{-1}), and r is the particle radius (m).[153] The root

mean square distance $\langle\overline{x^2}\rangle$ of a NP moving based on diffusion is explained by:

$$t = \frac{\langle\overline{x^2}\rangle}{2D} \tag{1.5}$$

where the time it takes for a given particle to travel an average total distance in one dimension is based on the diffusion coefficient for the particle. From this relationship it can be concluded that if the movement of a particle is based on diffusion, then the displacement of the particle will have a linear relationship with respect to the square root of time.

It is a commonly held belief that a colloidal suspension is stable and predominantly displays diffusional or Brownian motion. However, NPs of adequate size and composed of sufficiently dense material are also susceptible to settling due to gravitational force.[154] The rate of particle settling is influenced by buoyancy, drag, and gravity. Buoyancy and drag forces can oppose the gravitational forces and can increase the stability of particles in solution. Buoyancy is the force exerted by the fluid displaced by a particle and is a function of the particle volume and the density of the liquid. The drag force is produced by the fluid motion acting on the particle based on fluid viscosity, particle size, and velocity. Stoke's Law describes the terminal settling velocity of a particle in a solution

$$v_{sed} = \frac{g(\rho_p - \rho_m)d^2}{18\eta} \tag{1.6}$$

where g is the acceleration due to gravity (m s^{-2}), ρ_p is the particle density (g m^{-3}), and

ρ_m is the media density(g m^{-3}).[155] This formula shows that settling increased with particle density and the square of the particle radius, matching experimental and theoretical results based on the behavior of NP sedimentation.[154, 156, 157]

The Stokes-Einstein equation and Stokes Law define the transport of NPs in suspension based on diffusion and sedimentation. The final component that can influence the transport of NPs in suspension is the interaction between the particles that causes aggregation. NP aggregation is an extremely complex phenomenon with a few well-defined descriptions and calculations for estimating the kinetics of NP aggregation.[158-160] However, the accepted methods that typically describe particle transport assume that the particles do not interact in suspension. Movement of particles in a stagnate suspension under a uniform force, such as gravity, can then be described by the Mason-Weaver equation.[161]

$$\frac{\partial C}{\partial t} = D\frac{\partial^2 C}{\partial z^2} + v_{sed}\frac{\partial C}{\partial z} \tag{1.7}$$

In Equation 1.7 C is the concentration of particles in solution (mol L^{-1}), t is time (s), and z is the vertical direction opposing gravity. In this equation v_{sed} can also be displayed as the sedimentation coefficient (s) multiplied by gravitational force (g), two terms are which is sometimes displayed separately. The partial differential equation describes the movement of the particles in suspension as a function of both time and position after an initial point where all particles are evenly distributed in the suspension.

Most research involving NP incubations look at the size, shape, and surface chemistry of nanoparticles as having an influence on the interactions of NPs with biological

materials.[162-165] Few articles have taken into account the influence of sedimentation on NP incubations.[154] If it can be assumed that the dominate transportation of NPs in suspension is defined by the diffusion influenced by the behavior of the tracer antibody immobilized on the surface of an NP, then the diffusion and adsorption should follow a $t^{1/2}$ adsorption dependence.

1.9 Dissertation Overview

The bulk of the work in the dissertation is based on the themes introduced above. The primary aim is to address the concerns presented by the scientific community centered on the reliability of SERS-based detection method. Each of the chapters is presented as an individual manuscript that investigates differing aspects of the reliability of the SERS-based immunoassay. The foci of the chapters is on the influence of sampling and particle transport on the reliability of the SERS readout and the impact of the implementation of new techniques on the SERS analysis. Chapter 2 describes the investigation into the influence of sampling on SERS readout. Chapter 3 explains the development of procedures used for the SERS immunoassay towards the development of diffusional transport of ERLs in suspension in order to increase the likelihood of random dispersion on the immunoassay substrate. Chapter 4 discusses the development and implementation of the new techniques for the detection of TB markers. Chapter 5 outlines the validation of the platform via analysis of patient samples. This dissertation is concluded with a summation of the insights gained through these works and a discussion of the future prospects of these technologies.

1.10 References

(1) Fody, E. P.; Duben-Engelkirk, J. L.; Bishop, M. L. *Clinical Chemistry: Principles, Procedures, Correlations*; Lippincott: Philadelphia, 1985.

(2) Turner, A. *Biosensors: Fundamentals and Applications*; Oxford University Press: Oxford, 1987.

(3) Banica, F.-G. *Chemical Sensors and Biosensors: Fundamentals and Applications*; John Wiley & Sons: Chichester, 2012.

(4) McPhee, S. J.; Papadakis, M. A.; Rabow, M. W.; Education, M.-H. *Current Medical Diagnosis and Treatment 2012*; McGraw-Hill: New York, 2012.

(5) Swets, J. A. *Signal Detection Theory and ROC Analysis in Psychology and Diagnostics: Collected Papers*; Lawrence Erlbaum Associates: Mahwah, 2014.

(6) Youden, W. J. *Cancer* **1950,** *3,* 32-35.

(7) Horton, J. B.; Hollier, L. H. *Aesthet. Surg. J.* **2012,** *32,* 230-235.

(8) *Causes of Death 2008: Data Sources and Methods;* World Health Organization: Geneva, Switzerland, 2009.

(9) Meltzer, M. I.; Atkins, C. Y.; Santibanez, S.; Knust, B.; Petersen, B. W.; Ervin, E. D.; Nichol, S. T.; Damon, I. K.; Washington, M. L. *MMWR. Surveill. Summ.* **2014,** *63,*

(10) Dixon, M. G.; Schafer, I. J. *MMWR. Morb. Mortal. Wkly. Rep.* **2014,** *63,* 548-51.

(11) Zeman, D. H. *Swine Health Prod.* **1997,** *5,* 159-160.

(12) *Global Tuberculosis Report 2012;* World Health Organization: Geneva, Switzerland, 2012.

(13) Nester, E.; Aderson, D.; Roberts, C. E.; Nester, M. *Microbiology: A Human Perspective*; 5th ed.; McGraw-Hill: New York, 2007; p 593-595.

(14) *Commercial Serodiagnostic Test for Diagnosis of Tuberculosis;* World Health Organization: Geneva, Switzerland, 2011.

(15) Torrelles, J. B.; Sieling, P. A.; Zhang, N.; Keen, M. A.; McNeil, M. R.; Belisle, J. T.; Modlin, R. L.; Brennan, P. J.; Chatterjee, D. *Glycobiology* **2012,** *22,* 1118-1127.

(16) Cao, B.; Williams, S. J. *Nat. Prod. Rep.* **2010,** *27,* 919-947.

(17) Turnbull, W. B.; Stalford, S. A. *Org. Biomol. Chem.* **2012,** *10,* 5698-5706.

(18) Torrelles, J. B.; Azad, A. K.; Schlesinger, L. S. *J. Immunol.* **2006,** *177,* 1805-1816.

(19) Kratochvil, B.; Taylor, J. K. *Anal. Chem.* **1981,** *53,* 924A-938A.

(20) Kratochvil, B.; Wallace, D.; Taylor, J. K. *Anal. Chem.* **1984,** *56,* 113R-129R.

(21) Harris, D. C. *Quantitative Chemical Analysis*; Macmillan: New York, 2010.

(22) Brownlee, K. A. *Statistical Theory and Methodology in Science and Engineering*; Wiley: New York, 1965.

(23) Harvey, D. *Analytical Chemistry 2.0*; McGraw-Hill: New York, 2010.

(24) Harvey, D. *Modern Analytical Chemistry*; McGraw-Hill: New York, 2000.

(25) Youden, W. *J. AOAC* **1967,** *50,* 1007-&.

(26) Ingamells, C.; Switzer, P. *Talanta* **1973,** *20,* 547-568.

(27) Zeisler, R. *J. Res. Nat. Bur. Stand.* **1986,** *91,* 75-85.

(28) Svelto, O.; Hanna, D. C. *Principles of Lasers*; Springer Publishing: New York, 1976.

(29) Kim, J.; Kang, K.-N.; Sarkar, A.; Malempati, P.; Hah, D.; Daniels-Race, T.; Feldman, M. *J. Vac. Sci. Technol., B* **2013,** *31,* 06FE02.

(30) Sundaram, J.; Park, B.; Hinton Jr, A.; Windham, W.; Yoon, S.; Lawrence, K. *SPIE Defense, Security, and Sensing* **2011,** *8027,* 80270B.

(31) Gates, S. C.; Sweeley, C. C. *Clin. Chem.* **1978,** *24,* 1663-1673.

(32) Lansteiner, K. *The Specificity of Serological Reactions*; Harvard University Press: Cambridge, 1947.

(33) Mix, E.; Goertsches, R.; Zett, U. K. *J. Neurol.* **2006,** *253,* v9-v17.

(34) Yalow, R. S.; Berson, S. A. *Nature* **1986,** *184,* 1648-9.

(35) Jacobs, L.; Kagan, A.; Roy, B.; Friesen, H.; Glick, S. *Methods of Hormone Radioimmunoassay*; Academic Press: New York, 1979.

(36) Catt, K. J.; Niall, H. D.; Tregear, G. W. *Nature* **1967,** *213,* 825-7.

(37) Diamandis, E. P.; Christopoulos, T. K. *Immunoassay*; Academic Press: San Diego, 1996.

(38) Hemmila, I. *Clin. Chem.* **1985,** *31,* 359-370.

(39) Baker, T. S.; Abbott, S. R.; Daniel, S. G.; Wright, J. F. *Alternative Immunoassays*; John Wiley & Sons: Chichester, 1985.

(40) Johannsson, A.; Price, C.; Newman, D., Principles and Practice of Immunoassay. Price, CP: 1991.

(41) Nargessi, R. D.; Landon, J. *Methods Enzymol.* **1981,** *74,* 60-79.

(42) Engvall, E.; Perlmann, P. *Immunochemistry* **1971,** *8,* 871-874.

(43) Van Weemen, B.; Schuurs, A. *FEBS Lett.* **1971,** *15,* 232-236.

(44) John, W.; Edwards, R.; Price, C. *Ann. Clin. Biochem.* **1994,** *31,* 367-370.

(45) Emami, M.; Shamsipur, M.; Saber, R.; Irajirad, R. *Analyst* **2014,** *139,* 2858-2866.

(46) Tang, C. K.; Vaze, A.; Rusling, J. F. *Anal. Methods* **2014,** *6,* 8878-8881.

(47) Heineman, W. R.; Halsall, H. B. *Anal. Chem.* **1985,** *57,* 1321A-1331A.

(48) Jenkins, S. H. *J. Immunol. Methods* **1992,** *150,* 91-97.

(49) Smith, E. A.; Corn, R. M. *Appl. Spectrosc.* **2003,** *57,* 320A-332A.

(50) Mullett, W. M.; Lai, E. P. C.; Yeung, J. M. *Methods* **2000,** *22,* 77-91.

(51) Lyon, L. A.; Musick, M. D.; Natan, M. J. *Anal. Chem.* **1998,** *70,* 5177-5183.

(52) Nelson, B. P.; Grimsrud, T. E.; Liles, M. R.; Goodman, R. M.; Corn, R. M. *Anal. Chem.* **2001,** *73,* 1-7.

(53) Miyashita, M.; Shimada, T.; Miyagawa, H.; Akamatsu, M. *Anal. Bioanal. Chem.* **2005,** *381,* 667-673.

(54) Gobi, K. V.; Kataoka, C.; Miura, N. *Sens. Actuators, B* **2005,** *108,* 784-790.

(55) Fratamico, P. M.; Strobaugh, T. P.; Medina, M. B.; Gehring, A. G. *Biotechnol. Tech.* **1998,** *12,* 571-576.

(56) Bokken, G. C. A. M.; Corbee, R. J.; van Knapen, F.; Bergwerff, A. A. *FEMS Microbiol. Lett.* **2003,** *222,* 75-82.

(57) Sun, B.; Xie, W.; Yi, G.; Chen, D.; Zhou, Y.; Cheng, J. *J. Immunol. Methods* **2001,** *249,* 85-89.

(58) Goldman, E. R.; Balighian, E. D.; Kuno, M. K.; Labrenz, S.; Tran, P. T.; Anderson, G. P.; Mauro, J. M.; Mattoussi, H. *Phys. Status Solidi B* **2002,** *229,* 407-414.

(59) Goldman, E. R.; Balighian, E. D.; Mattoussi, H.; Kuno, M. K.; Mauro, J. M.; Tran, P. T.; Anderson, G. P. *J. Am. Chem. Soc.* **2002,** *124,* 6378-6382.

(60) Goldman, E. R.; Anderson, G. P.; Tran, P. T.; Mattoussi, H.; Charles, P. T.; Mauro, J. M. *Anal. Chem.* **2002,** *74,* 841-847.

(61) Goldman, E. R.; Medintz, I. L.; Mattoussi, H. *Anal. Bioanal. Chem.* **2006,** *384,* 560-563.

(62) Tran, P. T.; Goldman, E. R.; Anderson, G. P.; Mauro, J. M.; Mattoussi, H. *Phys. Stat. Sol. B* **2002,** *229,* 427-432.

(63) Hahn, M. A.; Tabb, J. S.; Krauss, T. D. *Anal. Chem.* **2005,** *77,* 4861-4869.

(64) Su, X.-L.; Li, Y. *Anal. Chem.* **2004,** *76,* 4806-4810.

(65) Chan, W. C.; Nie, S. *Science* **1998,** *281,* 2016-2018.

(66) Millen, R. L.; Kawaguchi, T.; Granger, M. C.; Porter, M. D.; Tondra, M. *Anal. Chem.* **2005,** *77,* 6581-6587.

(67) Wang, S. X.; Li, G. *IEEE Trans. Magn.* **2008,** *44,* 1687-1702.

(68) Butler, J. E. *Enzyme-linked immunosorbent assay*; CRC Press: Boca Raton, 2000; p 165-209.

(69) Driskell, J. D.; Kwarta, K. M.; Lipert, R. J.; Porter, M. D.; Neill, J. D.; Ridpath, J. F. *Anal. Chem.* **2005,** *77,* 6147-6154.

(70) Grubisha, D. S.; Lipert, R. J.; Park, H.-Y.; Driskell, J.; Porter, M. D. *Anal. Chem.* **2003,** *75,* 5936-5943.

(71) Ni, J.; Lipert, R. J.; Dawson, B.; Porter, M. D. *Anal. Chem.* **1999,** *71,* 4903-4908.

(72) Dou, X.; Takama, T.; Yamaguchi, T.; Tamamoto, H.; Ozaki, Y. *Anal. Chem.* **1997,** *69,* 1492-1495.

(73) Rohr, T. E.; Cotton, T.; Fan, N.; Tarcha, P. J. *Anal. Biochem.* **1989,** *182,* 388-398.

(74) Xu, S.; Ji, X.; Xu, W.; Li, X.; Wang, L.; Bai, Y.; Zhao, B.; Ozaki, Y. *Analyst* **2004,** *129,* 63-68.

(75) Mulvaney, S. P.; Musick, M. D.; Keating, C. D.; Natan, M. J. *Langmuir* **2003,** *19,* 4784-4790.

(76) Zhang, X.; Young, M. A.; Lyandres, O.; Duyne, R. P. V. *J. Am. Chem. Soc.* **2005,** *127,* 4484-4489.

(77) Ansari, D. O.; Stuart, D. A.; Nie, S. *Proc. of SPIE* **2005,** *5699,* 82-90.

(78) Cao, Y. C.; Jin, R.; Mirkin, C. A. *Science* **2002,** *297,* 1536-1540.

(79) Faulds, K.; Smith, D. R.; Graham, D. *Anal. Chem.* **2004,** *76,* 412-417.

(80) Faulds, K.; Barbagallo, R. P.; Keer, J. T.; Smith, D. R.; Graham, D. *Analyst* **2004,** *129,* 567-568.

(81) Graham, D.; Mallinder, B. J.; Whitcombe, D.; Smith, W. E. *ChemPhysChem* **2001,** *12,* 746-748.

(82) Graham, D.; Mallinder, B. J.; Whitcombe, D.; Watson, N. D.; Smith, W. E. *Anal. Chem.* **2002,** *74,* 1069-1074.

(83) Cui, Y.; Ren, B.; Yao, J.-L.; Gu, R.-A.; Tian, Z.-Q. *J. Phys. Chem. B* **2006,** *110,* 4002-4006.

(84) Granger, J. H.; Granger, M. C.; Firpo, M. A.; Mulvihill, S. J.; Porter, M. D. *Analyst* **2013,** *138,* 410-416.

(85) Wang, G.; Lipert, R. J.; Jain, M.; Kaur, S.; Chakraboty, S.; Torres, M. P.; Batra, S. K.; Brand, R. E.; Porter, M. D. *Anal. Chem.* **2011,** *83,* 2554-2561.

(86) Dufek, E. J.; Ehlert, B.; Granger, M. C.; Sandrock, T. M.; Legge, S. L.; Herrmann, M. G.; Meikle, A. W.; Porter, M. D. *Analyst* **2010,** *135,* 2811-2817.

(87) Wang, G.; Park, H.-Y.; Lipert, R. J.; Porter, M. D. *Anal. Chem.* **2009,** *81,* 9643-9650.

(88) Yakes, B. J.; Lipert, R. J.; Bannantine, J. P.; Porter, M. D. *Clin. Vaccine Immunol.* **2008,** *15,* 227-234.

(89) Singh, P.; Sharma, P. B.; Tyle, P. *Diagnostics in the Year 2000: Antibody, Biosensor, and Nucleic Acid Technologies*; Van Nostrand Reinhold: New York, 1993.

(90) Wu, J.; Fu, Z.; Yan, F.; Ju, H. *Trends Anal. Chem.* **2007,** *26,* 679-688.

(91) Diana, S. A.; Thurman, E. M. *Environmental Immunoassays: Alternative Techniques for Soil and Water Analysis*; American Chemical Society: Washington, 1997; p 1-20.

(92) Shan, G. *Immunoassays in Agricultural Biotechnology*; John Wiley & Sons: New York, 2011.

(93) Paraf, A.; Poltre, G. *Immunoassays in Food and Agriculture*; Kluwer Academic Publisher: Boston, 1991.

(94) Skoog, D. A.; Holler, F. J.; Nieman, T. A. *Principles of Instrumental Analysis*; Harcourt Brace & Company: Orlando, 1998.

(95) Ingle Jr., J. D.; Crouch, S. R. *Spectrochemical Analysis*; Prentice Hall: Upper Saddle River, 1988; p 590.

(96) Steen, W.; Watkins, K. G.; Mazumder, J. *Laser Material Processing*; Springer: Berlin, 2010.

(97) Fleischmann, M.; Hendra, P. J.; McQuillan, A. *Chem. Phys. Lett.* **1974,** *26,* 163-166.

(98) Albrecht, M. G.; Creighton, J. A. *J. Am. Chem. Soc.* **1977,** *99,* 5215-5217.

(99) Jeanmaire, D. L.; Van Duyne, R. P. *J. Electroanal. Chem.* **1977,** *84,* 1-20.

(100) Moskovits, M. *J. Chem. Phys.* **1978,** *69,* 4159-4161.

(101) Otto, A.; Timper, J.; Billmann, J.; Kovacs, G.; Pockrand, I. *Surf. Sci.* **1980,** *92,* L55-L57.

(102) Schatz, G. C.; VanDuyne, R. P. *Surf. Sci.* **1980,** *101,* 425-438.

(103) Wang, D.-S.; Chew, H.; Kerker, M. *Appl. Opt.* **1980,** *19,* 2256-2257.

(104) Kerker, M.; Siiman, O.; Bumm, L. A.; Wang, D.-S. *Appl. Opt.* **1980,** 3253-3255.

(105) Gersten, J.; Nitzan, A. *J. Phys. Chem.* **1980,** *73,* 3023-3037.

(106) Gersten, J. I. *J. Chem. Phys.* **1980,** *72,* 5779-5780.

(107) Aravind, P. K.; Nitzan, A.; Metiu, H. *Surf. Sci.* **1981,** *110,* 189-204.

(108) Abe, H.; Manzel, K.; Schulze, W.; Moskovits, M.; DiLella, D. P. *J. Chem. Phys.* **1981,** *74,* 792-797.

(109) Creighton, J. A. *Surf. Sci.* **1983,** *124,* 209-219.

(110) Schatz, G. C. *Acc. Chem. Res.* **1984,** *17,* 370-376.

(111) Kerker, M. *Acc. Chem. Res.* **1984,** *17,* 271-277.

(112) Zeman, E. J.; Schatz, G. C. *J. Phys. Chem.* **1987,** *91,* 634-643.

(113) Qian, X.-M.; Nie, S. *Chem. Soc. Rev.* **2008,** *37,* 912-920.

(114) Nie, S.; Emory, S. R. *science* **1997,** *275,* 1102-1106.

(115) Park, H.-Y.; Lipert, R. J.; Porter, M. D. In *Single-particle Raman Measurements of. Gold Nanoparticles Used in Surface-enhanced Raman Scattering (SERS)-based Sandwich Immunoassays*, Optics East, International Society for Optics and Photonics: 2004; pp 464-477.

(116) Liu, H.; Zhang, L.; Lang, X.; Yamaguchi, Y.; Iwasaki, H.; Inouye, Y.; Xue, Q.; Chen, M. *Sci. Rep.* **2011,** *1,* 1-5.

(117) Kneipp, K.; Moskovits, M.; Kneipp, H. *Surface-enhanced Raman Scattering: Physics and Applications*; Springer: Berlin, 2006.

(118) Stiles, P. L.; Dieringer, J. A.; Shah, N. C.; Van Duyne, R. P. *Annu. Rev. Anal. Chem.* **2008,** *1,* 601-626.

(119) Persson, B. N. J. *Chem. Phys. Lett.* **1981,** *82,* 561-565.

(120) Adrian, F. J. *J. Chem. Phys.* **1982,** *77,* 5302-5314.

(121) Kambhampati, P.; Child, C. M.; Foster, M. C.; Campion, A. *J. Chem. Phys.* **1998,** *108,* 5013-5026.

(122) Tabor, C.; Murali, R.; Mahmoud, M.; El-Sayed, M. A. *J. Phys. Chem. A* **2008,** *113,* 1946-1953.

(123) Reinhard, B. M.; Siu, M.; Agarwal, H.; Alivisatos, A. P.; Liphardt, J. *Nano Lett.* **2005,** *5,* 2246-2252.

(124) Kinnan, M. K.; Chumanov, G. *J. Phys. Chem. C* **2010,** *114,* 7496-7501.

(125) Kim, K.; Yoon, J. K. *J. Phys. Chem. B* **2005,** *109,* 20731-20736.

(126) Holland, W. R.; Hall, D. In *Coupling of Radiation into Thin Film Modes by Means of Localized Plasma Resonances*; Optics East, International Society for Optics and Photonics: 1983; pp 188-190.

(127) Kume, T.; Nakagawa, N.; Hayashi, S.; Yamamoto, K. *Solid State Commun.* **1995,** *93,* 171-175.

(128) Shchegrov, A.; Novikov, I.; Maradudin, A. *Phys. Rev. Lett.* **1997,** *78,* 4269.

(129) Zheng, J.; Zhou, Y.; Li, X.; Ji, Y.; Lu, T.; Gu, R. *Langmuir* **2003,** *19,* 632-636.

(130) Kim, K.; Lee, H. S. *J. Phys. Chem. B* **2005,** *109,* 18929-18934.

(131) Orendorff, C. J.; Gole, A.; Sau, T. K.; Murphy, C. J. *Anal. Chem.* **2005,** *77,* 3261-3266.

(132) Driskell, J. D.; Lipert, R. J.; Porter, M. D. *J. Phys. Chem. B* **2006,** *110,* 17444-17451.

(133) Wind, M.; Vlieger, J.; Bedeaux, D. *Physica A* **1987,** *141,* 33-57.

(134) Okamoto, T.; Yamaguchi, I. *J. Phys. Chem. B* **2003,** *107,* 10321-10324.

(135) Kimling, J.; Maier, M.; Okenve, B.; Kotaidis, V.; Ballot, H.; Plech, A. *J. Phys. Chem. B* **2006,** *110,* 15700-15707.

(136) Li, L.; Hutter, T.; Steiner, U.; Mahajan, S. *Analyst* **2013,** *138,* 4574-4578.

(137) Mock, J. J.; Hill, R. T.; Degiron, A.; Zauscher, S.; Chilkoti, A.; Smith, D. R. *Nano Lett.* **2008,** *8,* 2245-2252.

(138) Schatz, G. C.; Van Duyne, R. P. *Electromagnetic Mechanism of Surface-enhanced Spectroscopy*; John Wiley & Sons: Chichester, 2002.

(139) Hill, R. T.; Mock, J. J.; Urzhumov, Y.; Sebba, D. S.; Oldenburg, S. J.; Chen, S.-Y.; Lazarides, A. A.; Chilkoti, A.; Smith, D. R. *Nano Lett.* **2010,** *10,* 4150-4154.

(140) Yoon, J. K.; Kim, K.; Shin, K. S. *J. Phys. Chem. C* **2009,** *113,* 1769-1774.

(141) Mubeen, S.; Zhang, S.; Kim, N.; Lee, S.; Krämer, S.; Xu, H.; Moskovits, M. *Nano Lett.* **2012,** *12,* 2088-2094.

(142) Knight, M. W.; Wu, Y.; Lassiter, J. B.; Nordlander, P.; Halas, N. J. *Nano Lett.* **2009,** *9,* 2188-2192.

(143) Kim, K.; Lee, H. B.; Yoon, J. K.; Shin, D.; Shin, K. S. *J. Phys. Chem. C* **2010,** *114,* 13589-13595.

(144) Li, L.; Hutter, T.; Finnemore, A. S.; Huang, F. M.; Baumberg, J. J.; Elliott, S. R.; Steiner, U.; Mahajan, S. *Nano Lett.* **2012,** *12,* 4242-4246.

(145) Rodríguez-Lorenzo, L.; Alvarez-Puebla, R. A.; Pastoriza-Santos, I.; Mazzucco, S.; Stéphan, O.; Kociak, M.; Liz-Marzán, L. M.; García de Abajo, F. J. *J. Am. Chem. Soc.* **2009,** *131,* 4616-4618.

(146) Braun, G. B.; Lee, S. J.; Laurence, T.; Fera, N.; Fabris, L.; Bazan, G. C.; Moskovits, M.; Reich, N. O. *J. Phys. Chem. C* **2009,** *113,* 13622-13629.

(147) Braun, G.; Pavel, I.; Morrill, A. R.; Seferos, D. S.; Bazan, G. C.; Reich, N. O.; Moskovits, M. *J. Am. Chem. Soc.* **2007,** *129,* 7760-7761.

(148) Jain, P. K.; Huang, W.; El-Sayed, M. A. *Nano Lett.* **2007,** *7,* 2080-2088.

(149) Su, K. H.; Wei, Q. H.; Zhang, X.; Mock, J. J.; Smith, D. R.; Schultz, S. *Nano Lett.* **2003,** *3,* 1087-1090.

(150) Driskell, J. D.; Uhlenkamp, J. M.; Lipert, R. J.; Porter, M. D. *Anal. Chem.* **2007,** *79,* 4141-4148.

(151) Yakes, B. J.; Lipert, R. J.; Bannantine, J. P.; Porter, M. D. *Clin. Vaccine Immunol.* **2008,** *15,* 235-242.

(152) Batchelor, G. K. *An Introduction to Fluid Dynamics*; Cambridge University Press: Cambridge, 2000.

(153) Zwanzig, R.; Harrison, A. K. *J. Chem. Phys.* **1985,** *83,* 5861-5862.

(154) Cho, E. C.; Zhang, Q.; Xia, Y. *Nat. Nanotechnol.* **2011,** *6,* 385-391.

(155) Lamb, H. *Hydrodynamics*; Cambridge University Press: Cambridge, 1993.

(156) Alexander, C. M.; Dabrowiak, J. C.; Goodisman, J. *J. Colloid Interface Sci.* **2013,** *396,* 53-62.

(157) Alexander, C. M.; Goodisman, J. *J. Colloid Interface Sci.* **2014,** *418,* 103-112.

(158) Kallay, N.; Žalac, S. *J. Colloid Interface Sci.* **2002,** *253,* 70-76.

(159) French, R. A.; Jacobson, A. R.; Kim, B.; Isley, S. L.; Penn, R. L.; Baveye, P. C. *Environ. Sci. Technol.* **2009,** *43,* 1354-1359.

(160) Huynh, K. A.; Chen, K. L. *Environ. Sci. Technol.* **2011,** *45,* 5564-5571.

(161) Mason, M.; Weaver, W. *Phys. Rev.* **1924,** *23,* 412-426.

(162) Jiang, W.; Kim, B. Y.; Rutka, J. T.; Chan, W. C. *Nat. Nanotechnol.* **2008,** *3,* 145-150.

(163) Chithrani, B. D.; Chan, W. C. *Nano Lett.* **2007,** *7,* 1542-1550.

(164) Verma, A.; Stellacci, F. *Small* **2010,** *6,* 12-21.

(165) Leroueil, P. R.; Hong, S.; Mecke, A.; Baker Jr, J. R.; Orr, B. G.; Banaszak Holl, M. M. *Acc. Chem. Res.* **2007,** *40,* 335-342.

CHAPTER 2

IMPACT OF SAMPLING ERROR ON THE ANALYSIS OF NANOPARTICLE-BASED SURFACE-ENHANCED RAMAN SCATTERING IMMUNOASSAYS

2.1 Introduction

Surface-enhanced Raman scattering (SERS) has emerged as a powerful tool for the analysis of a wide range of materials.[1-3] However, the reliability of this surface-sensitive technique to serve as a basis for quantitative measurements remains an ongoing concern.[4-8] Part of the issue rests with the intrigue and importance of creating nanostructured materials that have ever-larger enhancements. Many of these materials, however, can be difficult to prepare reproducibly or have a size and/or shape that may have limited structural stability.[9, 10] As a result, several laboratories,[4-8, 11-18] including the Porter laboratory,[3, 19-26] have pursued tactics that have proven useful in overcoming the reproducibility of SERS measurements. Our approach sacrifices the extraordinarily high-levels of enhancement afforded by some types of nanostructured materials (e.g., nanocavity arrays,[5, 8, 27] nanostructured metal surfaces,[28-31] and porous metal films[32]) by using particle geometries (e.g., spherically-shaped particles), which are more readily produced with a more controllable and stable size and shape dispersity but do not have as large of a plasmonics-based signal enhancement.[33, 34] This "management of reproducibility"[33, 35-37] has begun to

demonstrate the merits of SERS as an quantitative analysis tool in diagnostic testing [3, 7, 22, 38, 39] and other arenas.[2, 40-42]

This paper examines another obstacle encountered when attempting to take advantage of the strength of SERS as a quantitative measurement tool: sampling error. By sampling error, we are referring to the error introduced in a measurement when the size of the sample analyzed is below that needed to represent reliably the composition of the sample. We show herein how sampling error occurs with SERS due to the small size of the focused laser spot that is typically used to measure the concentration of biolytes captured and labeled in the sandwich-styled, SERS-based immunoassay shown in Figure 2.1. Indeed, this type of sampling error is exactly the same as the classic sampling problem encountered when, for example, the size of the sample collected and analyzed from a large waste site fails to match accurately that of a larger, more representative sample, which introduces bias into the measurement.

The statistical underpinning of this situation is found in the central limit theorem. This theorem states that the data collected from a sufficiently large sampling of a population will be normally distributed about the mean value of the population.[43, 44] This theorem also indicates that the variance of the measured distribution will decrease as the size of the sampled population becomes larger and/or the number of samplings of a population, $n_{\text{replicate}}$, at a fixed sample size is increased. The benefits of increasing n is, however, governed by the law of diminishing returns.[45] The law of diminishing returns dictates that the decrease in the variance of the measurement, and thus improvements in the "trueness" of the mean, improves with $\sqrt{n}$.

We hypothesized that a significant and unrecognized portion of the error associated

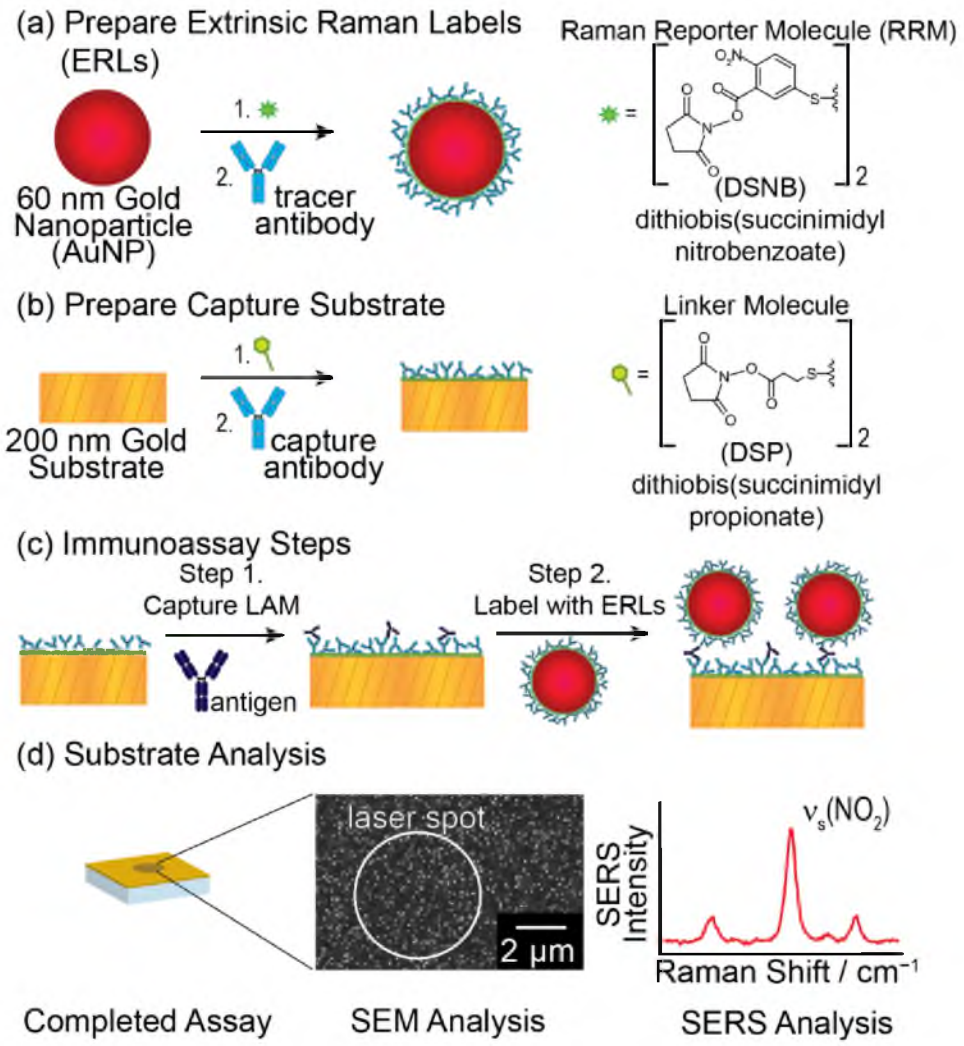

Figure 2.1. The three primary steps of the SERS-based immunoassay: (a) preparation of extrinsic Raman labels (ERLs); (b) preparation of the capture substrate; and (c) procedure for the production of the antigen sandwich. The first two primary steps are performed prior to the assay. The immunoassay is performed by incubating a 20 µL droplet on the capture substrate at room temperature. The sample is then rinsed, exposed to a 20 µL droplet of ERLs, rinsed, dried under ambient conditions, and analyzed. (d) Analysis of the SERS-based preparation is performed via excitation of the SERS substrate with a focused laser spot. The SEM images shows ERLs on the capture surface and the SERS spectrum collected from a focused laser spot with a 5 µm diameter.

with SERS readout, especially when attempting to push limits of detection (LoD) to lower levels, is due to sampling error. In diagnostic tests like enzyme-linked immunosorbent assays (ELISA),[46] the signal arises from a measurement of the homogenous solution produced at the end of the assay. This type of readout inherently averages the response across the entire capture address located at the bottom of each well in a microplate. However, the optics associated with a Raman spectrometer are designed to have high light collection efficiencies by using optical components with large numerical apertures, which result in small laser spot sizes, that is, small surface sampling areas. In most Raman spectrometers, the actual area of the focused laser spot is exceedingly small (tens of microns in diameter), which examines only a small fraction of the total surface of the sample (e.g., a 10 μm laser spot interrogates ~10^{-6} of the geometric surface area of a 3 mm diameter address). It follows that a small analysis area can result in an inherent sampling error that can lead to a large measurement variance and a biased "apparent" mean value, both of which become more problematic as the analyte concentration in the assayed sample decreases.

There are several statistical methods that can be used to assess the impact of the variance of an analytical measurement. The overall variance[47-49] of the analytical result, s_O^2, equals the sum of the relative variance due to sampling, s_s^2, and the relative variance due the actual measurement, s_l^2. This relationship can be written as:

$$s_O^2 = s_l^2 + s_s^2 \tag{2.1}$$

Assuming that all of the other components of the assay are under statically control,[50] s_l^2

can be found by measuring repeatedly a sample that produces a consistent signal. That is, the variance in the measurement represents the overall instrumental error, for example, power fluctuations and detector noise. As a result, s_s^2 can be determined from the difference between s_O^2 and s_s^2. Too often, however, attempts to improve the precision of a measurement focus on reducing s_i^2, while neglecting the importance of s_s^2. Youden's Rule of Thumb states that if s_s^2 is nine times greater than s_i^2, only marginal improvements in s_O^2 will be realized when attempting to improve s_s^2. In such a case, more notable improvements in s_O^2 will be achieved by lowering s_s^2, which entails either an increase in the number of replicate samplings ($n_{\text{replicate}}$) of fixed size or an increase in the overall size of each sample being analyzed in one sampling.

One approach to this type of analysis is to determine the amount of sample needed to produce results at a predefined level of reliability (i.e., accuracy and precision). Classically, this can be done using the sampling constant, K_S:

$$K_S = mR^2 \tag{2.2}$$

where m is the mass of the sample and R is the percent relative standard deviation (%RSD) due to sampling error. While the use of K_S is frequently associated with the analysis of particulate-based samples[51, 52] (e.g., the analysis of a small fraction of a powdered sample), it can be applied to other types of analyses that may be plagued by undersampling. This approach is most useful in the sampling region where the accuracy and precision of the results is sensitive to the sample size. K_S can then be calculated to determine the mass required to realize, for example, a 1% RSD for a particular sample type.

Herein, we examine the impact of sampling error when using SERS as a quantitative analytical tool in a sandwich-styled immunoassay. In doing so, we first construct a simple random accumulation model to represent the SERS immunoassay substrate removing any systematic or experimental error. Analysis of the modeled substrate is then used to determine the error associated strictly with the analysis of the substrate.

2.2 Experimental

2.2.1 Reagents and Materials

Borate buffer packs (pH 8.5), modified Dulbecco's phosphate buffed saline packs (pH 7.4), dithiobis(succinimidyl propionate) (DSP), and StartingBlock were obtained from Thermo Scientific. Acetonitrile (ACN), Tween 20, sodium chloride, and bovine serum albumin (BSA) were purchased from Sigma-Aldrich. Goat antihuman immunoglobulin G and human IgG were acquired from Pierce; Epoxy 377 from EPO-TEK; octadecanethiol (ODT) from Fluka, poly(dimethyl siloxane) (PDMS) from SlyGard; and 200-proof ethanol from Pharmco-AAPER. The synthesis of the Raman reporter molecule 5-5'-dithiobis(succinimidyl-2-nitrobenzoate) (DSNB) has been described previously.[22] All reagents were used without further purification.

2.2.2 Preparation of Extrinsic Raman Labels (ERLs)

A detailed description of the SERS assay procedure has been described previously.[19] The ERLs were prepared in batches using a 0.96 mL suspension of 60-nm gold nanoparticles (AuNPs) at 2.6×10^{10} AuNPs/mL, and adjusting the buffer strength by the addition of 40 μL of 50 mM borate buffer (BB, pH 8.5). The buffered AuNPs (2.0 mM

BB) were then modified by the addition of 10 μL of 1.0 mM DSNB, followed by 10.0 μg of antihuman IgG (13.3 μL of 1.5 mg/mL stock solution), and 100 μL of 10% BSA (20 mM BB), which produced a 1% BSA solution. After letting the resulting suspenstion stand for 7 h, excess reactants were removed by centrifugation of the suspension at 2,000*g* for 10 min to pellet the ERLs and then by withdrawing carefully the supernatant. The ERLs were resuspended with 1.0 mL 1% BSA (2.0 mM BB). This cleanup process was repeated two more times. As a result of these steps, the ERLs were concentrated to 4.0×10^{10}, as determined using the spectrometric method of Haiss and collaborators.[53]

2.2.3 Preparation of the Capture Substrate and SERS Immunoassay Procedure

The capture substrate was prepared on template stripped gold (TSG) by first creating a hydrophobic boundary, which defined address diameter (2.0 or 3.0 mm) address, using microcontact printing with ODT. The address was then reacted with DSP (14-16 h), followed by 2.0 μg/mL of the capture antibody, antihuman IgG, in 10 mM phosphate-buffered saline with 1% Tween 20 (PBST, pH 7.4) for 7 h. These capture substrates were rinsed three times with PBST and treated with StartingBlock. Finally, the substrates were incubated with antigen solution (20 μL), rinsed three times with PBST, inverted, exposed to the ERL suspension for 16 h, rinsed with BB [0.1% Tween 20, 10 mM NaCl (BBT, pH 8.5)], and allowed to dry under ambient conditions for a least 1 h.

2.2.4 Instrumentation

Analysis and mapping of the sample substrates by SERS used a Thermo Scientific DXR Raman microscope that was equipped with a HeNe laser (632.8 nm), a thermoelectrically cooled to (−65 ^{0}C) CCD detector, and a 50 μm entrance slit. The spectral resolution changed from 5.2 to 8.8 cm^{-1} over the spectral acquisition range of 50 to 3500 cm^{-1}, respectively. All spectra were collected by averaging the signal from two 1-s integrations at each sample location. The microscope was fitted with a 10x Olympus MPlan N objective, which predicts a 5-μm diameter laser spot, or a 50× objective, which predicts a laser spot diameter of 0.5 μm.

The Raman map was collected in 20-μm steps over the entire assay address (2.0 mm) by using a translation stage with a 1-μm resolution. Maps for 2.0-mm addresses consist of ~14,500 data points (i.e., a square matrix of ~120 rows and columns) of data, whereas the 3.0-mm maps contain ~26,000 data points (i.e., a square matrix of ~160 rows and columns) of data. The intensity at each location was determined from the SERS spectrum based on the peak height at 1336 cm^{-1} [$\upsilon_s(NO_2)$] of DSNB after baseline correction, which was then normalized to the average signal of 4,000 data points at the center of the address. The *x*- and *y*-coordinates for each pixel were converted to polar coordinates in order to analyze and present the data as a function of the radial displacement of the signal from the center of the address. Next, the frequency of the signal strengths were then organized by binning the normalized intensities into 0.01 increments, with the resulting histogram fit to a Gaussian distribution by means of a nonlinear least squares analysis. Finally, the residuals of the Gaussian fit were plotted to examine the quality of the fit with respect to the actual data distribution about the mean value.

Scanning electron microscopy (SEM) images were obtained using a field emission scanning electron microscope (NanoNova SEM, FEI) equipped with a through-the-lens detector. Post imaging analysis used ImageJ software (National Institutes of Health, Bethesda, MD).

2.2.5 Computational Modeling

In order to understand the impact of sampling size on the measurement (i.e., the area of the capture surface interrogated by the focused laser light), Monte Carlo simulations (C++ programing language) were designed to mimic the analysis of the sample by SERS. The first step in the simulation produced a two-dimensional (2D) surface (3.0 mm diameter only) composed of a random distribution of point-sized adsorbates (PSAs). The next step simulated the analysis of the surface by a focused laser spot by randomly placing a disk of predetermined area on the simulated capture surface and counting the number of PSAs encompassed within the disk. Different predetermined numbers of replicate measurements were then made by repeating the procedure, with the average and standard deviation of PSAs per unit area used to assess the accuracy and precision of the results.

To produce a 2D surface with a random PSA distribution, a 3×10^{15} by 3×10^{15} x-y network was populated by using a pseudo-random number generator with 15 digit accuracy. A location was rejected if it was positioned outside the defined 3.0-mm diameter address. This process was repeated until reaching a specified number of randomly selected locations across the address.

Given the spacing between PSAs, the x- and y-coordinates in both directions have a step size of 1×10^{-15} mm. This produces PSAs of an equal square size of 9.0×10^{-18} nm^2

that were then populated with 1×10^7 PSAs (unless otherwise defined) within the defined 3.0-mm disk. We did not account for the possibility of PSA co-occupancy, but the probability of populating the same location was extremely low.

To simulate the analysis of an address by a laser spot, a pseudo-random number generator was used to select another set of *x*- and *y*-coordinates to serve as the center of a predefined circular analysis area. If the entire analysis area was contained within the bounds of the defined 3.0-mm diameter address, the number of PSAs was counted and recorded. An analysis area was rejected if any portion of the analysis area extended beyond the defined 3.0-mm address, and a new location was chosen.

The results from all of the simulations are reported as the area analysis ratio (AAR). The AAR is defined as the area contained within a single circular analysis area divided by the total area of the simulated substrate. A majority of results presented are for AAR values from 0.99 to 1×10^{-7}. By way of example, a substrate with a 3.0-mm diameter has an area of 7.07×10^6 μm^2. AARs of 0.99 and 1×10^{-7}, and therefore equate to simulated laser spots with areas of 7.0×10^6 and 7.1×10^{-1} μm^2, respectively; these AARs correspond to circular analysis diameters of 2.9 mm and 0.95 μm.

2.3 Results and Discussion

2.3.1 SEM Imaging and Development of a Monte Carlo Simulation for an NP-based Immunoassay Substrate

To set the stage for the sampling problem associated with the analysis of an NP-based SERS immunoassay substrate, we devised a random accumulation model (RAM) to document how the accuracy and precision of the measurement are affected by the surface

area of the sample analyzed. We opted to construct a computational model of the immunoassay in order to eliminate any impact from possible experimental biases in preparing the assay components or from carrying out the assay. To do so, we first defined a standard (i.e., an expectation value) to use for the RAM from SEM images of a SERS substrate after the completion of an assay. A representative image is shown in Figure 2.2. This image is for a capture substrate that was first exposed to an antigen (H-IgG) concentration of 6.67×10^{-11} M (10.0 ng mL^{-1} H- IgG) and subsequently to a suspension of ERLs with a gold core of ~60 nm.

The image consists largely of isolated ERLs, a few cluster-like (for example, dimers, trimers, and short filaments) arrangements, and clearly visible voids. A few nonspherically-shaped ERLs are also evident. This distribution is characteristic of randomly accumulated particles on a surface,[54] and is representative of 5 images obtained from different locations across the sample surface. Determination of the number of ERLs in the 5 images yielded an average density of 13.5 ± 1.5 ERLs μm^{-2}. For the Monte Carlo simulations, we used a lower PSA density (1.415 PSAs μm^{-2} or 1.000×10^7 PSAs for a 3-mm diameter address) in order to manage computational time, which proportionally corresponds to a H-IgG concentration of 4.35×10^{-11} M (~0.74 ng/mL H- IgG). The true value for the computational simulation was defined to have 4 significant figures in order to more fully assess the impact of the results. We have assumed that each captured antigen is tagged by one ERL.

Figure 2.3a presents an example of the random accumulation of PSAs on a 3-mm diameter substrate. For visual clarity, the representations show only 5,000 of the randomly distributed PSAs. Each PSA is represented by an oversized cross that is ~10^{31} times larger

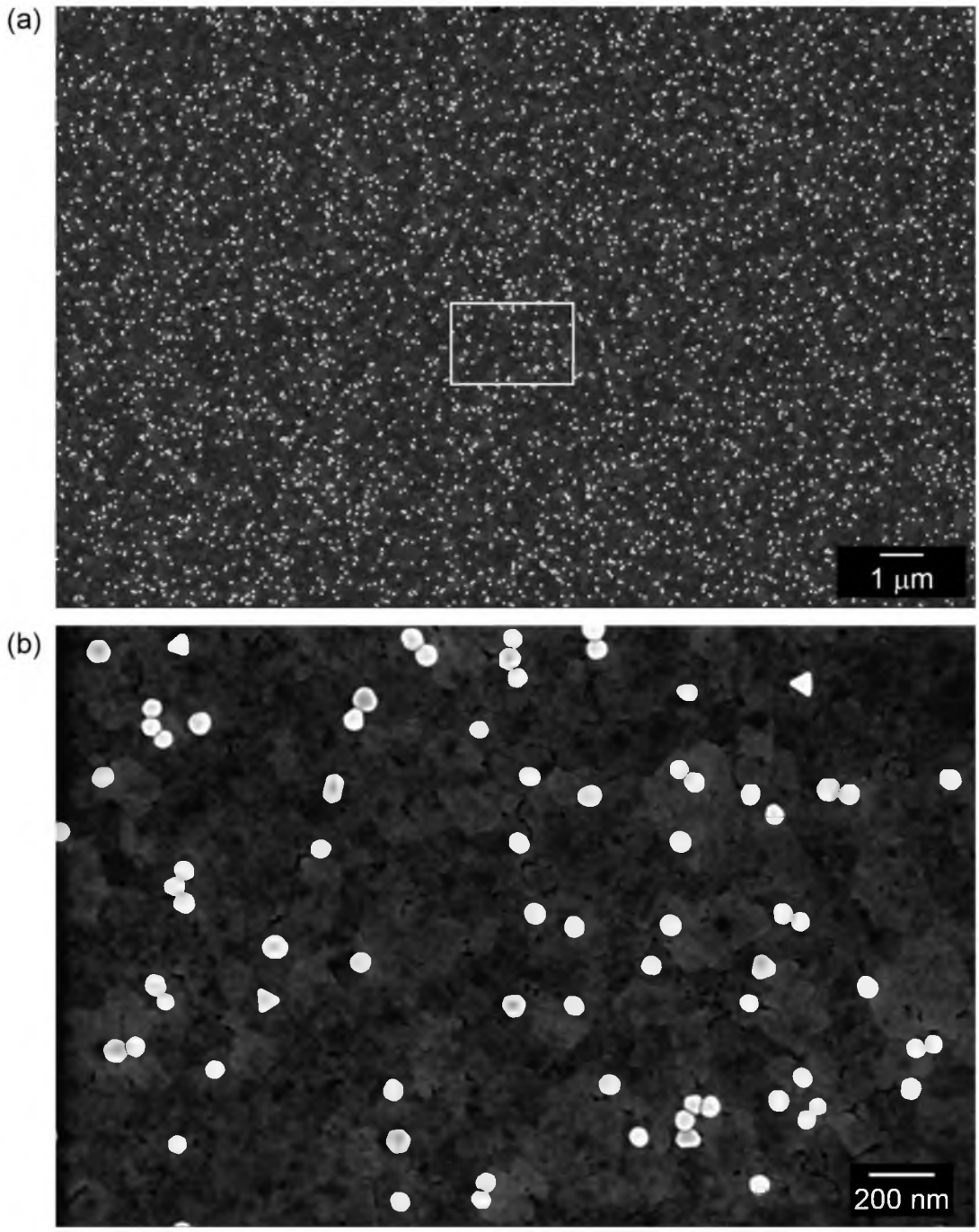

Figure 2.2. SEM image of a SERS immunoassay substrate for H-IgG at a concentration of 6.67×10^{-11} M (10.0 ng mL^{-1}), which has an ERL density of ~13.5 ± 1.5 ERLs μm^{-2}. The brighter circular features in the SEM image are consistent with a 60 nm AuNP core used to produce ERLs. (a) Image area of ~290 μm^2; (b) enlargement of the highlighted area in the center of (a).

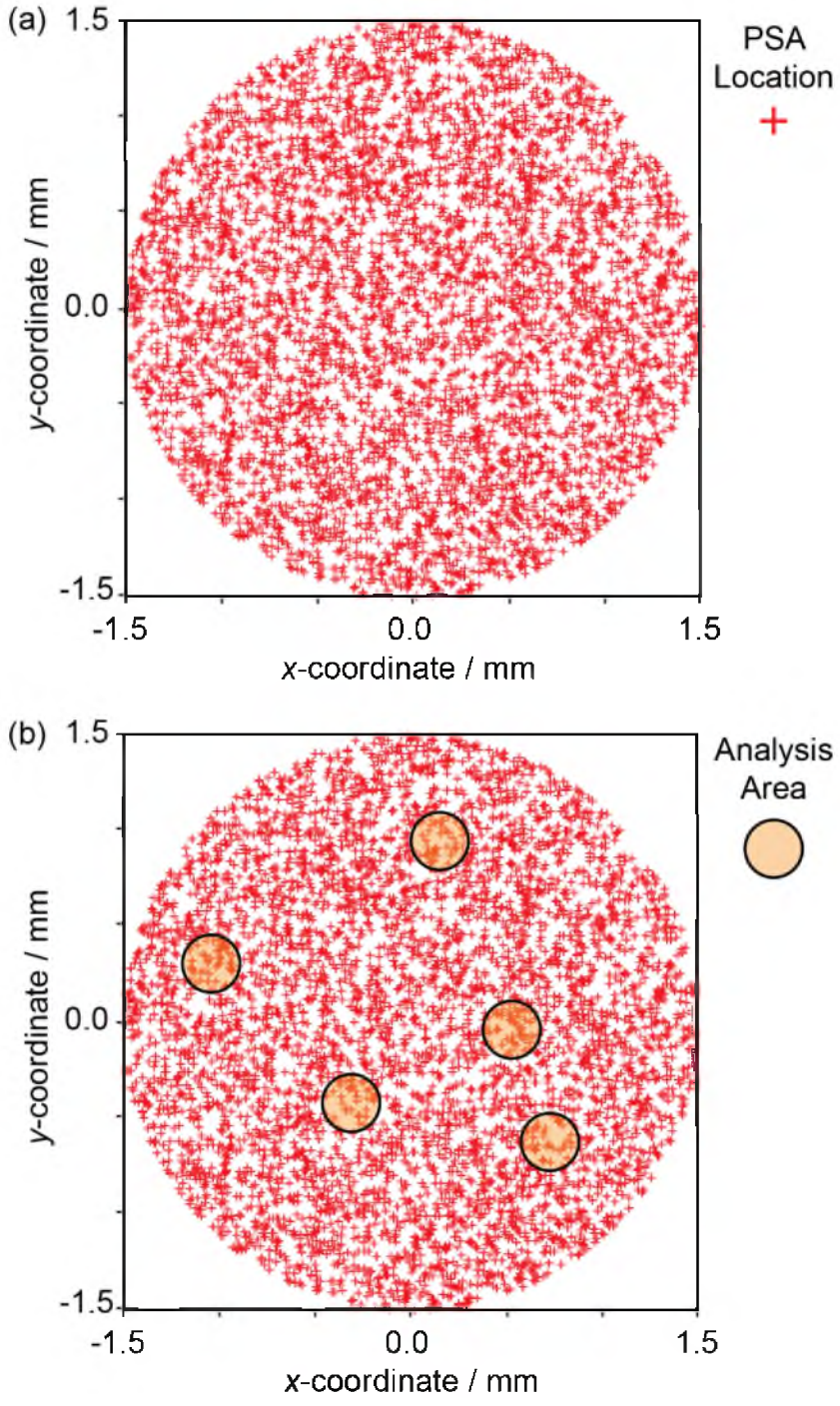

Figure 2.3. Visual representation of pseudo-random distribution of PSAs on a 3.0-mm diameter substrate. (a) 5,000 oversized PSAs (1×10^{31} times larger than actual size) on the simulated address. (b) Same simulated substrate with five randomly located analysis areas, each with a 300-μm diameter or an AAR of 1.0×10^{-2}.

than an actual PSA; the actual size of a PSA is not be visible at the length scale of the two representations. The analysis example in Figure 2.3b shows the location of 5 randomly than placed, disk-shaped analysis areas ($n_{replicate}$ = 5), each with a diameter of 300 μm or an AAR of 1.0 $\times 10^{-2}$. The analysis counts the number of PSAs within each disk, and the average and standard deviation of the results for different sizes and numbers of sampling areas are then compared to the true value (mean) for the simulated substrates to determine the accuracy and precision of the measurements.

2.3.2 Importance of $n_{replicate}$ and Sample Size Using a Simulated Assay

Assuming all other components of the assay are under statistical control, the reliability of a measurement can be improved by increasing the sample size. The sample size is related to the number of measurements on the substrate ($n_{replicate}$) for a given AAR and/or by increasing the actual size of each sampling (AAR). Data for assessing the impact of each approach are shown in Figure 2.4 by plotting the PSA density, average absolute deviation from the mean ($\mathcal{D}_{Avg}$), and standard deviation (s) from the mean as a function of $n_{replicate}$ for three values of AAR: 1.0 $\times$ 10^{-7} (0.95 μm diameter), 1.0 $\times$ 10^{-6} (3.0 μm diameter), and 1.0 $\times$ 10^{-5} (9.5 μm diameter). These results are from 10 separate simulations with $n_{replicate}$ equal to 1, 2, 3, 4, 5, 10, 25, 50, 75, and 100 in order to examine the trends in $\mathcal{D}_{Avg}$ and s. Figure 2.4a shows the raw simulation results with many of the points overlapping due the discrete values for PSA analysis with small AARs. Values for $\mathcal{D}_{Avg}$ and s indicate trends in the simulated data for the accuracy and precision, respectively.

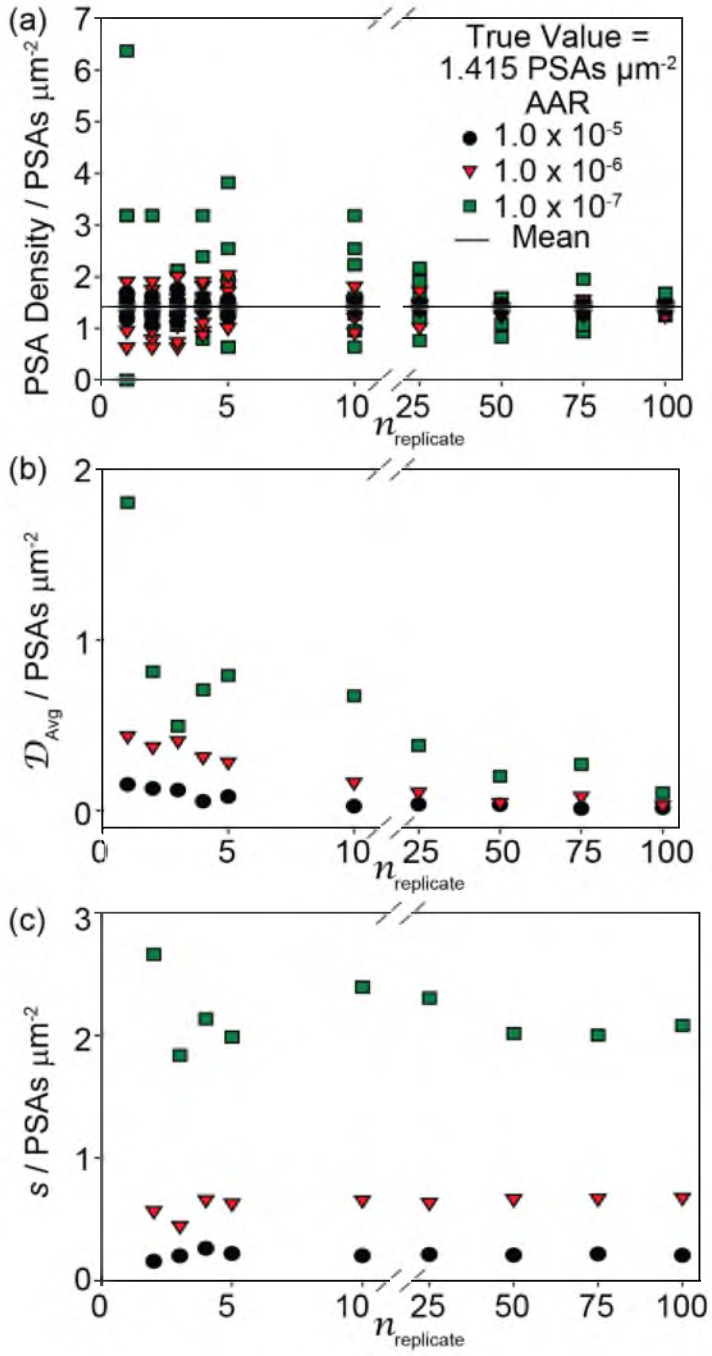

Figure 2.4. Results from 10 simulations of the random accumulation of PSAs indicate the impact of $n_{replicate}$ on the (a) raw simulation results for PSA density (b) accuracy expressed as the $\mathcal{D}_{Avg}$, and (c) the precision expressed as the s for PSA counting, with no provided value for $n_{replicate}$ of one. Results are shown for several AARs that were selected based on the magnitude of change in the accuracy and precision.

As evident, increases in both $n_{replicate}$ and AAR improve the accuracy of the measurement (that is, $\mathcal{D}_{Avg}$ approaches zero). The improvement with $n_{replicate}$ is the most notable for the smallest AAR, 1.0×10^{-7}. That is, the rate of convergence in accuracy is dependent on the total area sampled; thus, the largest of the sampled areas (AAR = 1.0×10^{-5}) has the highest rate of convergence, and the smallest of the sampled areas (AAR = 1.0×10^{-7}) has the lowest rate of convergence. The error in the accuracy for an AAR of 1.0×10^{-7} for an $n_{replicate}$ of 1 is ~80% larger than that for $n_{replicate} \geq 25$. Similar improvements in accuracy are also evident for the larger AARs (1.0×10^{-6} and 1.0×10^{-5}), though not as dramatic. These results indicate, as expected, that increases in both $n_{replicate}$ and AAR can be used to improve the accuracy of the measurement.

Figure 2.4c plots how the precision (i.e., s) of the simulated measurements is influenced by $n_{replicate}$ as a function of the same three AAR values. The results show that s at a given AAR fluctuates at low values of $n_{replicate}$, but then converge to different limiting levels as $n_{replicate}$ increases. The smallest AAR value, 1.0×10^{-7}, approaches a limit in s at an $n_{replicate}$ of ~50. This value of s indicates that the error in the measurement is larger than the mean value of the measurement (Figure 2.4c), that is, representing a large fundamental error due to undersampling. The two larger AARs, 1.0×10^{-6} and 1.0×10^{-5}, approach smaller limiting values in s after only 10 measurements, which document a clear improvement in the error associated with sampling. As will be shown later, the fundamental error associated with sample size is a large source of the actual experimental error reported in our SERS-based immunoassay results. Note also that the value for s follow the expected

decrease with respect to the $\sqrt{n}$ as expected.

These results can be used to estimate the minimum value for $n_{replicate}$ at a given AAR that is needed to produce a true value by using the sampling variance at each AAR. The minimum value of $n_{replicate}$, calculated for a chosen confidence interval, for a target RSD is expressed as:

$$n_{replicate} = \frac{t^2 s^2}{RSD^2} \tag{2.3}$$

where t can be found from the Student's t-table at a given confidence level. With a confidence interval of 95%, a relative standard deviation of 1% (an RSD of 0.014 with respect to the true value of 1.415 PSAs μm^{-2}), and a value for s (determined by the simulation for values of $n_{replicate} > 50$), the minimum value of $n_{replicate}$ required to produce a result at the specified tolerance can be calculated.

Using these parameter values, the simulated results indicate that an $n_{replicate}$ of 1 is sufficient to measure the true PSA density of 1.415 PSAs μm^{-2} for AARs larger than 1.0×10^{-2} ($\geq$ 300 µm diameter). For the smaller AARs of 1.0×10^{-3} (95 µm diameter), 1.0×10^{-4} (30 µm diameter), 1.0×10^{-5} (9.5 µm diameter), 1.0×10^{-6} (3.0 µm diameter), and 1.0×10^{-7} (0.95 µm diameter), the required values of $n_{replicate}$ are 1, 8, 857, 8,768, and 81,359, respectively. If the %RSD is increased by a factor of 5 to 5%, which approximates the error expected from the noise of the instrument used in our experiments (see section 2.3.6), the values of $n_{replicate}$ for 1.0×10^{-4}, 1.0×10^{-5}, 1.0×10^{-6}, and 1.0×10^{-7} decrease to 3, 34, 355, and 3,254, respectively. All larger AARs require only a single measurement.

The impact of increasing AAR was also examined and these results are presented in Figure 2.5. The inserts have an *x*- and *y*-axis on a log scale in order to show the small changes in the results. The evolution in $\mathcal{D}_{Avg}$ and s indicate that $n_{replicate}$ has a larger impact on the results for lower AARs. Improvements in the results for different numbers of $n_{replicate}$ are evident for lower AARs, but are only marginally distinguishable, at best, at higher values of AAR. The AAR that shows the greatest increase in accuracy and precision is for an AAR of 1.0×10^{-7} to $\sim 1.0 \times 10^{-2}$. When the value of AAR is $\sim 1.0 \times 10^{-2}$ (i.e., a 300-μm diameter laser spot), the simulated measurement for a PSA density of 1.415 PSAs μm^{-2} is > 99% accurate and has an RSD of 1% or better for $n_{replicate} > 2$. AARs matching the laser spot size (e.g., 0.5 to 5 μm laser spot diameter) would indicate that larger laser spot sizes would produce more accurate and precise results. The benefit of using a larger laser spot does none the less come with a tradeoff. That is, the use of a lower numerical aperture to increase the spot size also decreases the collection efficiency, and thus, LoD of the objective.

2.3.3 Normal Distribution of Simulation Results for a Given AAR.

Another way to examine the differences in the impact of sample size is to analyze the results in terms of the normal distribution of 100 simulations, each at an $n_{replicate} = 1$. These plots are shown in Figure 2.6. The center of the distribution represents the mean of the results, whereas the standard deviation is directly linked to the width of the distribution. The normal distribution for an accurate and precise result therefore depends on a given AAR. In other words, a bias-free measurement will have a higher accuracy and precision

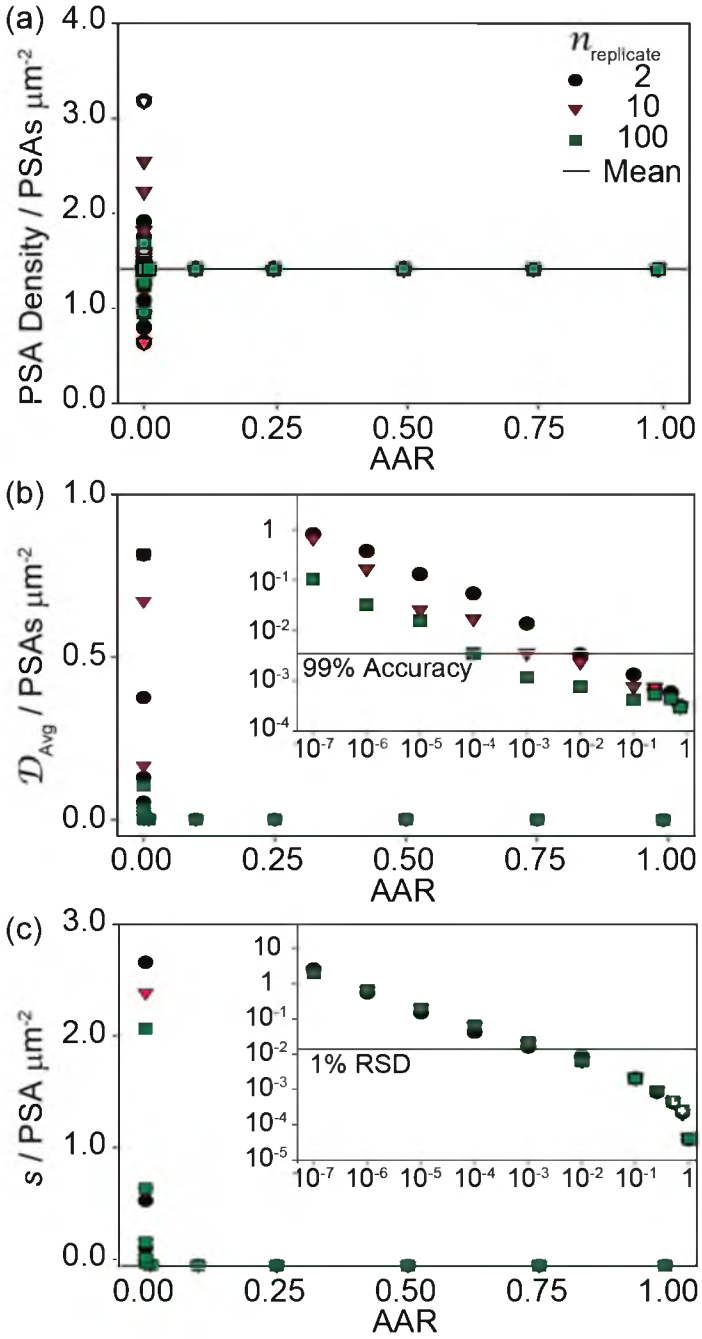

Figure 2.5. Monte Carlo simulation results indicating the impact of sample size in terms of the AAR on the (a) PSA density, (b) accuracy expressed as the $\mathcal{D}_{Avg}$, and the (c) precision expressed as the s from the mean. Insets show the same data with the x- and y-axis on a log scale to highlight small changes in the data. Results are shown for several $n_{replicate}$ samples taken to demonstrate the relative influence on the results.

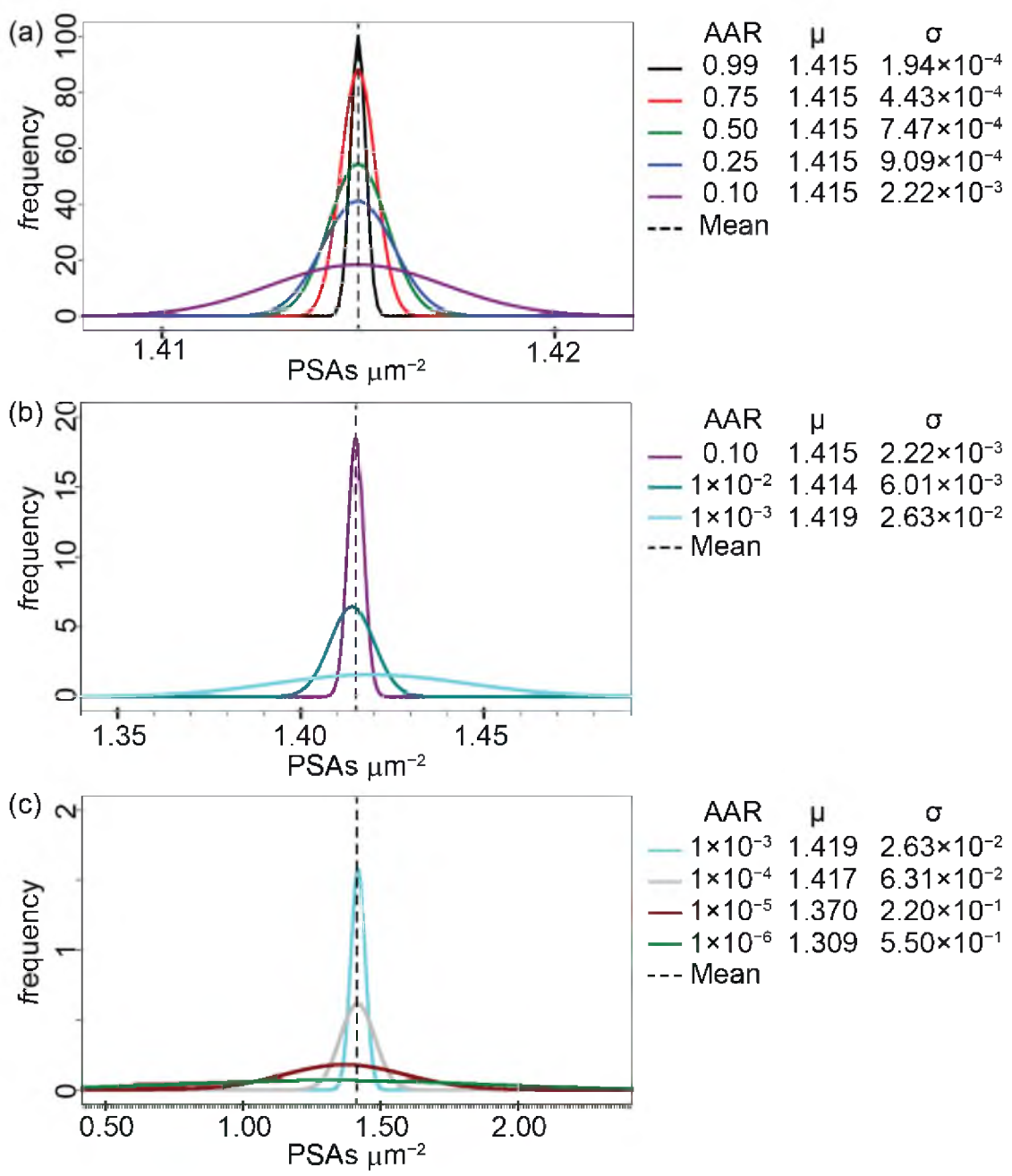

Figure 2.6. Normal distribution curves for data collected from 100 simulation results. (a) Normal distribution curves for AARs between 99 and 1.0×10^{-6}. (b) Normal distribution curves for AARs between 0.10 and 1.0×10^{-3}. (c) AARs between 1.0×10^{-3} and 1.0×10^{-6} on different vertical and horizontal scales to show differences in the height and width of the distributions. The values for µ and σ for each fit are shown within the figure.

at a larger value of AAR.

As expected, the results show that the highest probability of measuring an accurate and precise value occurs at an AAR of 0.99. The precision in the measurement, however, degrades with decreases in AAR. This is represented, for example, by the increase of the width of the distribution at the AAR of 0.10, the center of the normal distribution of the profile shifts away from the true mean value, indicating inaccuracy in the results. It is also important to note that the accuracy of the measurements begins to diminish as AAR decreases. Below an AAR of 0.99 represents how small decreases in AAR have an impact on the potential distribution of the results. We note that the analysis of an AAR of 1.0×10^{-7} is not shown because the extremely small sample size produces discretized results that are dominated by zeros and cannot be reliably fit.

2.3.4 Determination of the Sampling Constant (K_S) for the Simulated SERS Substrate

The simulations show that the accuracy of the results converge more rapidly towards the true value with increases in AAR, following the expectations of the sampling problem associated with the accuracy and precision often found when determining trace constituents in geological samples.[51] Along these lines, Equation 2.2, which is used to establish the mass of a sample required in geological analysis to reach a given accuracy and precision, was adapted to determine K_S for the simulated SERS substrate by setting m equal to AAR.

To predict the K_S value, 10 separate simulations were carried out and analyzed to determine the spread of the results for evenly spaced increments of AARs between $1.0 \times$

10^{-3} to 0.5. The resulting PSA densities versus AAR are presented in Figure 2.7a. The distributions again exhibit an increase in the accuracy and precision of the measurement with larger values of AAR. This plot was used to calculate values of the RSD for the measurement at each AAR, which was then applied to construct the graph in Figure 2.7b of %RSD versus the diameter of the sampling area. For a 1% RSD, the laser spot size has a diameter of 550 μm, which corresponds to a value for K_S of 3.4×10^{-2} AAR. After finding K_S, Equation 2.2 can be rearranged to calculate the AAR required for a given RSD. By loosening the tolerance in the precision, for example, from 1% RSD to 5% RSD, the required value of AAR decreases from 3.4×10^{-4} to 1.4×10^{-3} or from a sampling diameter of 550 to 56 μm, respectively. The results for the 5% RSD are of particular interest, being a readily achievable laser spot diameter. A laser diameter of 100 μm, which is available in commercially available instrumentation, would require a laser power of 2 W to achieve an equivalent power density as a laser spot diameter of 5.0 μm at 5 mW.

2.3.5 Monte Carlo Simulations on the Influence of AAR on LoD

The LoD of a method is defined as the lowest concentration that can be distinguished from the blank based on a specified level of confidence.[55] In terms of NP-based SERS detection, a single ERL can produce a signal that is distinguishable from the background (this analysis assumes that there is not a contribution to the measurement from nonspecific adsorption).[3, 24] Using this performance level as a guiding metric, we can define the LoD for the simulations as the ability to find at least one PSA with 95% confidence for a given AAR. We assume that there is no nonspecific adsorption, no mass transfer limitations, infinite sample volume, and that the binding affinity has a linear relationship

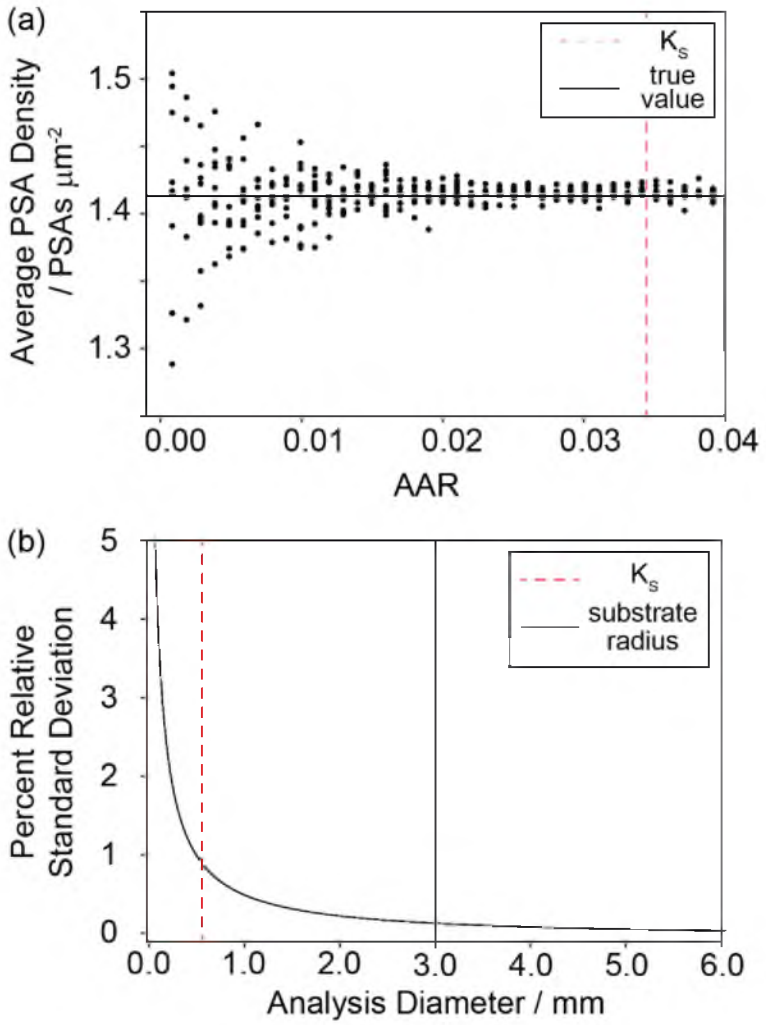

Figure 2.7. Determination of the sampling constant (K_S) based on simulation results. (a) Sampling diagram of simulated results for PSA counting of a random distribution of PSAs on a 3.0-mm substrate with 1.415 PSAs µm^{-2} for 10 simulations results with an $n_{\text{replicate}}$ of one. (b) Plot of analysis diameter (mm) versus percent relative standard deviation equal to $\sqrt{K_S/m}$ based on Equation 2.2. The calculation predicts the percent relative standard deviation past the substrate diameter because the calculation assumes an infinite substrate size.

with the ERL density displayed for the 10 ng mL^{-1} sample down to a blank with zero binding. For this analysis, the number of PSAs on a 3.0-mm diameter substrate was varied and analyzed with a value of $n_{replicate}$ of 100 for densities ranging from 1 to 1×10^7 PSAs μm^{-2} at intervals of half an order of magnitude. The average number ($\bar{x}$) and standard deviation (s) for the PSAs accumulated by the simulation were then used to calculate the lowest PSA density in which at least one PSA will be detected at 95% confidence from an individual simulation. The t value for a one-sided (0.5%) probability distribution with (n−1) degrees of freedom is 1.645, which indicates that if the value of $\bar{x} - 1.645s \geq 1$, then the AAR is of sufficient size as defined by the LoD. A pictorial representation of the predicted LoD is shown in Figure 2.8, and the LoD versus AAR is presented in the insert.

The LoD versus AAR plot indicates that increases in AAR yield lower LoDs. The inset shows the y-axis on a log scale to highlight changes in the LoD for larger AARs. The largest impact on the LOD is again found for the lowest AARs. At an AAR of ~0.1 (1.1 mm diameter) or larger, the benefit of further increases in the AAR in terms of LoD is only marginal. An AAR of 0.1 gives and LoD equivalent to a PSA density of 5.66×10^{-5} PSAs μm^{-2}. Based on a simple linear projection of the ERL densities given in Figure 2.2, these findings point to a low LoD at femtomolar concentrations. The inset of Figure 2.8 shows above and AAR of 0.1, there are small but continual decreases in the LoD but no more than a single order of magnitude. There is, however, a significant drop in the LoD that occurs at an AAR of 0.99. This decrease is present due to minimal percentage of the surface that is missed by the laser spot pressing the LoD closer to the limit of 1 PSA per address and corresponds to attomolar concentrations LoD.

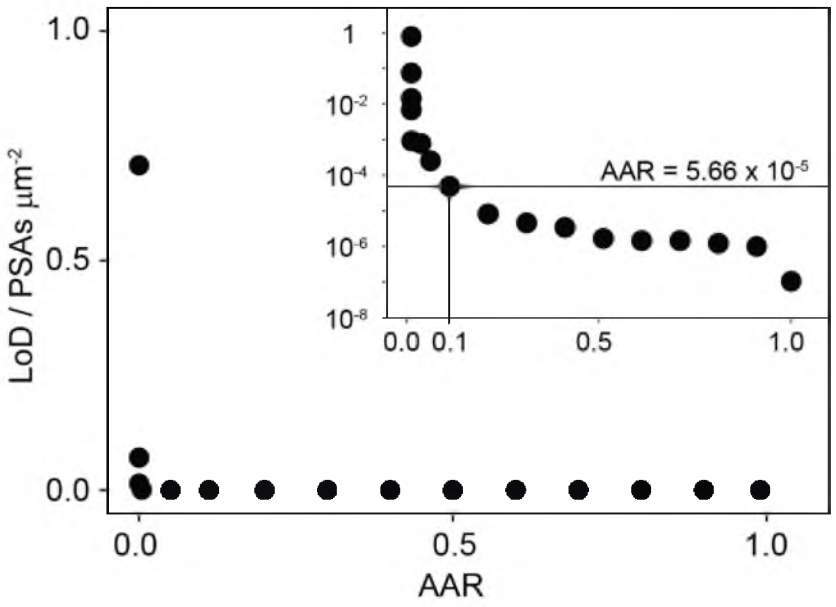

Figure 2.8. Monte Carlo simulation results for LoD. AAR vs. LoD in PSAs μm^{-2} based on 95% confidence that the measurement was above 1 PSA on the substrate. Inset shows the same data with the *y*-axis on the log scale. Simulations for a random distribution of particles on a 3.0-mm circular substrate for various particle densities with 100 $n_{replicate}$ were used for the 95% confidence calculations.

2.3.6 Analysis of SERS Immunoassay Substrates

This section examines the degree of signal variation in the form a high density Raman map for a SERS-based immunoassay substrate. The sample was prepared using the procedure described in the Experimental section. Figure 2.9 presents a 2 × 2 mm Raman map (Figure 2.9a) of a 2-mm diameter capture substrate and the subsequent analysis of the signal distribution (Figures 2.9b-d). The map was constructed by mounting the sample on an *x*-*y* translation stage that was moved in 20 μm steps and analyzing each location with a 10× microscope objective (laser spot diameter of 5.0 μm at 5 mW). These intensities were normalized to the average SERS intensity for the central 4,000 data points [data within an approximate 700 μm diameter (red circle)], which was selected to omit the inclusion of the obvious defects in the sample just beyond the area bound within the circle. The plot has a normalized signal intensity of $1.00 \pm 8.30 \times 10^{-2}$, which was produced from a raw signal with an average and standard deviation of 1223 ± 104 cts s^{-1}. The green color represents the normalized single of 1.0, with orange and red colors depicting higher signals of 1.5 and 2.0, respectively. The blue and violet colors signify the lower signals of 0.5 and no observable signal, respectively. Note that the signal intensity outside of the defined address area are comparable to that of the background.

To examine the signal distribution across the substrate, the data map was converted from Cartesian to polar coordinates and then plotted in Figure 2.9b as the normalized SERS intensity versus radial distance from the center of the address. The average SERS intensity ($\bar{x}$), which was normalized to unity, and the corresponding 95% confidence interval surrounding the mean ($\pm 1.96 \times s$) are represented by the solid and dashed black lines, respectively. A least squares fit to the data was also performed by converting the signal to

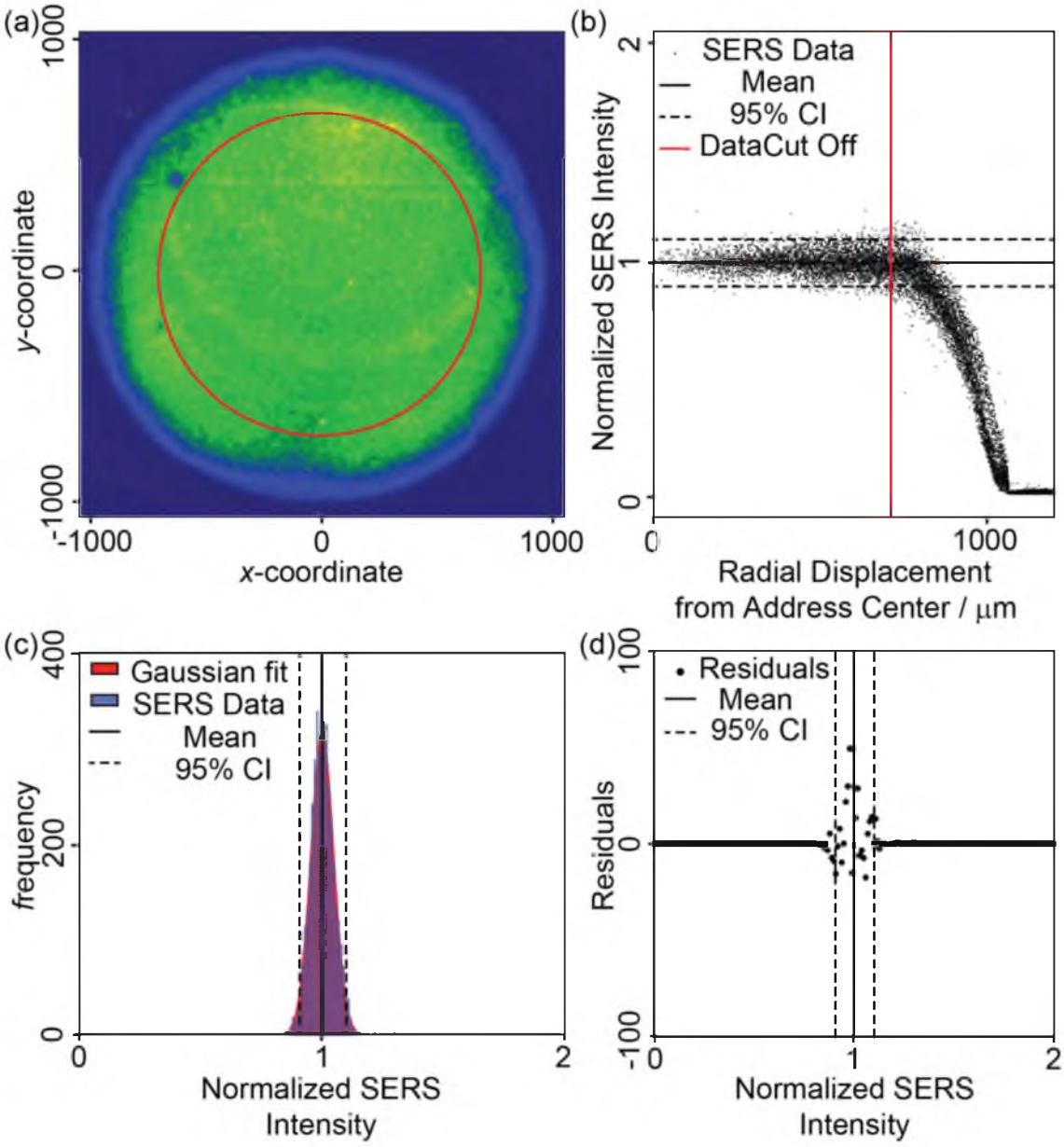

Figure 2.9. SERS immunoassay substrate analyzed with (a) high density Raman color contrast mapping of the normalized signal intensity. Green represents the mean signal from the central 4,000 data points (within the red circle). Warmer and cooler colors indicate higher and lower signal intensities, respectively. (b) Normalized SERS signal is shown in polar coordinates to highlight differences in the signal distribution from the center to the outer edge of the address. (c) The central 4,000 data points represented in a histogram with the data are binned into 0.01 normalized increments with a linear least squares fit to a normal distribution. (d) Residuals for the least squares fit to a normal distribution. The solid black lines represent a normalized signal of one, the dashed black lines indicate the 95% CI, and red lines indicate the 4,000 data point cutoff.

a histogram (Figure 2.9c) in 0.01 normalized intensity steps. The residuals for a least squares fit to the histogram (Figure 2.9d) do not have a notable pattern, indicating a reasonable representation of the data.

To quantify the contribution of the signal variance from sampling error, s_s^2, the signal variance from the instrument, s_i^2, was determined by collecting 100 spectra from the on a freshly polished glassy carbon substrate and analyzing the peak height from the 1332 cm^{-1} band. A normalized signal of $1.00 \pm 3.02 \times 10^{-2}$, which equals a s_i^2 of 9.34×10^{-4}, was calculated from the raw signal intensity of 175 ± 6 cts s^{-1}. The overall variance, s_O^2, was calculated from Equation 2.1 as 5.97×10^{-3} or $1.00 \pm 8.30 \times 10^{-2}$. The value for s_s^2 was determined to be 6.39 times the value of s_i^2. The higher signal variance for the analysis of the same substrate indicates addressing the sampling issue will lead to more improvements in the signal than from improving the variance due to the instrument.

The SERS substrate in Figure 2.9 was also analyzed with a 50× microscope objectives (AAR = 6.3×10^{-8}, 0.5-μm diameter laser spot at 0.5 mW) to assess the impact of sampling area on the measurement results. These data are shown in Figure 2.10. The high density SERS maps collected from the two experiments are normalized because of the large differences in signal intensity due to the collection efficiencies for the 10× and 50× microscope objectives. The average and standard deviation for 100 randomly selected laser spots within the central portion of the addresses produced signals of 1235 ± 108 (1.00 ± 0.09 when normalized) and 4782 ± 862 cts s^{-1} (1.00 ± 0.18 when normalized) for the 10× (5.0 mW) and 50× (0.5 mW) objectives, respectively. The laser power was lowered to 0.5 mW in the 50× objective measurements due to saturation of the CCD at higher laser powers. Differences in the signal are indicated by the $\mathcal{D}_{\text{Avg}}$, s, and normal distribution of

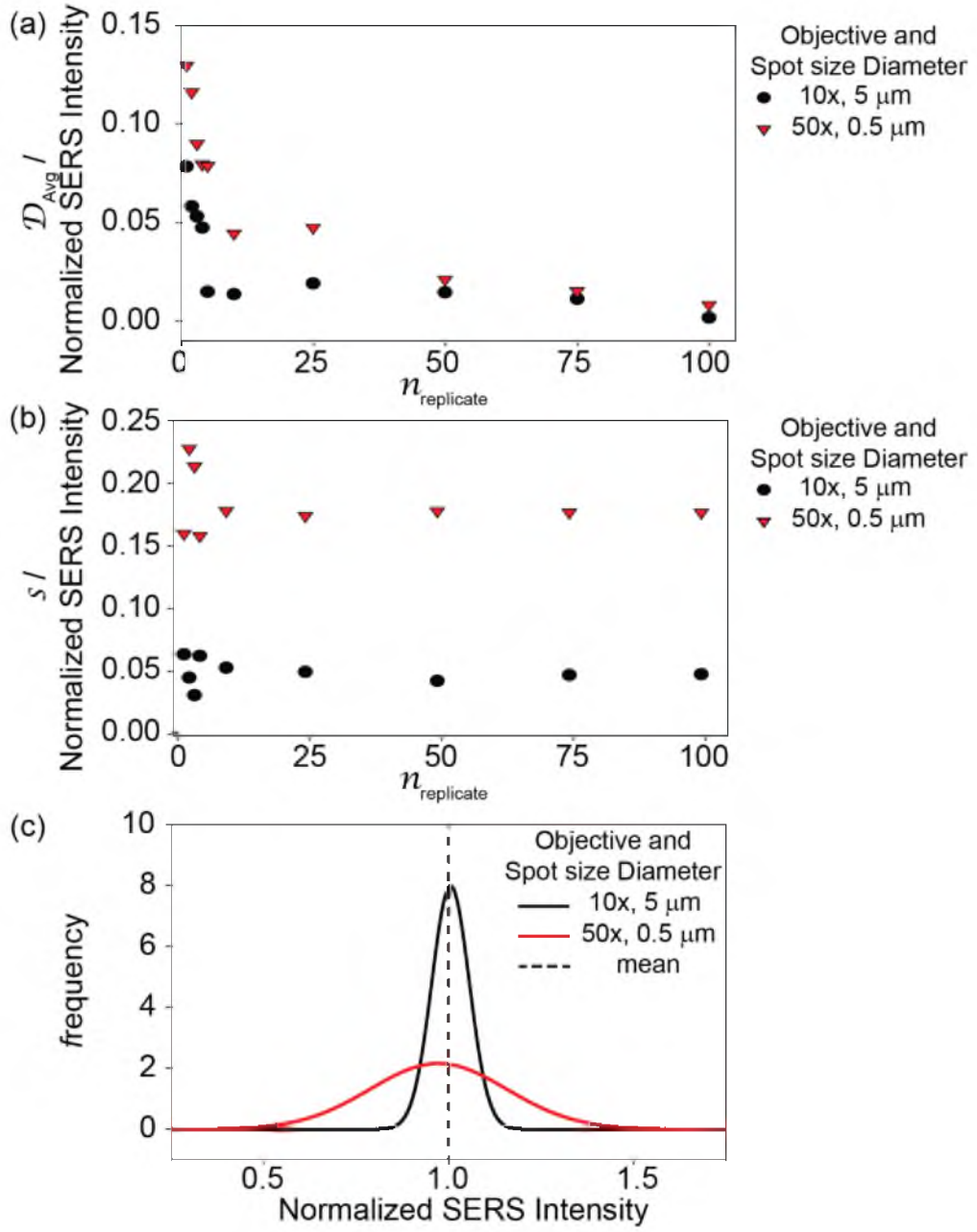

Figure 2.10. Raman analysis of ERL-based SERS-based immunoassay substrate for the detection of H-IgG at 10.0 ng mL^{-1}. The impact of $n_{replicate}$ on the (a) accuracy expressed as $\mathcal{D}_{Avg}$, and (b) precision expressed as s for the two different spot size. (c) Normalized distributions of the signal from 100 $n_{replicate}$ measurements on the same substrate for analysis diameters of 5 and 0.5 μm.

the data.

Empirical analysis demonstrates the benefits of using an objective with a larger spot size for increased accuracy and precision in the measurements. While sensitivity of the sample size is less significant, the differences are likely present due to the increased density of ERLs on the substrate (Figure 2.2) relative to the PSA density of 1.415 PSAs μm^{-2} investigated in a majority of the simulations. However, the data does indicate that undersampling the surface with the 50× objective introduces a fundamental error associated with the analysis method that impacts the accuracy and precision of the measurements. The results for the minimal required $n_{replicate}$ for accurate analysis is 4 and 51 for the 10× and 50× objective, respectively. The data can also be used to calculate a K_S of 5.5×10^{-2} AAR (470 μm diameter) for a 1% RSD on the 2-mm SERS substrate. Further analysis with a 5% RSD indicates a required AAR of 5.5×10^{-4} (47 μm diameter).

2.4 Conclusions

There is no question as to the benefits of using SERS over classical Raman spectroscopy in terms of detection. However, a deficiency in the reproducibility of the signal enhancement continues to limit its application. This work has shown, both through simulations and experiments, the importance of sample size, as related to the focused laser spot, on reproducibility. Too small of spot size, that is, a classic undersampling problem, results in large deviations in the accuracy and reproducibility of the measurement. By judicious use of the concepts herein, we believe that a key, but unrecognized component to the SERS reproducibility can be readily overcome by carefully considering the impact of sampling on the results. Future work is aimed at delineating the range and scope of the

results presented herein.

2.5 References

(1) Kudelski, A. *Talanta* **2008,** *76,* 1-8.

(2) Kneipp, K.; Haka, A. S.; Kneipp, H.; Badizadegan, K.; Yoshizawa, N.; Boone, C.; Shafer-Peltier, K. E.; Motz, J. T.; Dasari, R. R.; Feld, M. S. *Appl. Spectrosc.* **2002,** *56,* 150-154.

(3) Porter, M. D.; Lipert, R. J.; Siperko, L. M.; Wang, G.; Narayanan, R. *Chem. Soc. Rev.* **2008,** *37,* 1001-1011.

(4) Jarvis, R.; Johnson, H.; Olembe, E.; Panneerselvam, A.; Malik, M.; Afzaal, M.; O'Brien, P.; Goodacre, R. *Analyst* **2008,** *133,* 1449-1452.

(5) Vernon, K. C.; Davis, T. J.; Scholes, F. H.; Gómez, D. E.; Lau, D. *J. Raman Spectrosc.* **2010,** *41,* 1106-1111.

(6) Strehle, K. R.; Cialla, D.; Rösch, P.; Henkel, T.; Köhler, M.; Popp, J. *Anal. Chem.* **2007,** *79,* 1542-1547.

(7) Lee, M.; Lee, S.; Lee, J.-h.; Lim, H.-w.; Seong, G. H.; Lee, E. K.; Chang, S.-I.; Oh, C. H.; Choo, J. *Biosens. Bioelectron.* **2011,** *26,* 2135-2141.

(8) Dinish, U. S.; Yaw, F.; Agarwal, A.; Olivo, M. *Biosens. Bioelectron.* **2011,** *26,* 1987-1992.

(9) Fleischmann, M.; Hendra, P. J.; McQuillan, A. *Chem. Phys. Lett.* **1974,** *26,* 163-166.

(10) Jeanmaire, D. L.; Van Duyne, R. P. *J. Electroanal. Chem.* **1977,** *84,* 1-20.

(11) Hu, J.; Zhao, B.; Xu, W.; Fan, Y.; Li, B.; Ozaki, Y. *Langmuir* **2002,** *18,* 6839-6844.

(12) Lim, D.-K.; Jeon, K.-S.; Hwang, J.-H.; Kim, H.; Kwon, S.; Suh, Y. D.; Nam, J.-M. *Nat. Nanotechnol.* **2011,** *6,* 452-460.

(13) Alexander, T.; Cullum, B.; Carter, J. C. In *Applications of Surface-enhanced Raman Spectroscopy (SERS) for Biosensing: An Analysis of Reproducible, Commercially Available Substrates*, Optics Easr, International Society for Optics and Photonics: 2005; p 600703.

(14) Li, W.; Camargo, P. H.; Lu, X.; Xia, Y. *Nano Lett.* **2008,** *9,* 485-490.

(15) Liu, X.; Shao, Y.; Tang, Y.; Yao, K.-F. *Sci. Rep.* **2014,** *4,* 5835.

(16) Tripp, R. A.; Dluhy, R. A.; Zhao, Y. *Nano Today* **2008,** *3,* 31-37.

(17) Lyvers, D. P.; Moon, J.-M.; Kildishev, A. V.; Shalaev, V. M.; Wei, A. *ACS Nano* **2008,** *2,* 2569-2576.

(18) Jeon, T. Y.; Park, S.-G.; Lee, S. Y.; Jeon, H. C.; Yang, S.-M. *ACS Appl. Mater. Interfaces* **2013,** *5,* 243-248.

(19) Driskell, J. D.; Kwarta, K. M.; Lipert, R. J.; Porter, M. D.; Neill, J. D.; Ridpath, J. F. *Anal. Chem.* **2005,** *77,* 6147-6154.

(20) Dufek, E. J.; Ehlert, B.; Granger, M. C.; Sandrock, T. M.; Legge, S. L.; Herrmann, M. G.; Meikle, A. W.; Porter, M. D. *Analyst* **2010,** *135,* 2811-2817.

(21) Granger, J. H.; Granger, M. C.; Firpo, M. A.; Mulvihill, S. J.; Porter, M. D. *Analyst* **2013,** *138,* 410-416.

(22) Grubisha, D. S.; Lipert, R. J.; Park, H.-Y.; Driskell, J.; Porter, M. D. *Anal. Chem.* **2003,** *75,* 5936-5943.

(23) Ni, J.; Lipert, R. J.; Dawson, G. B.; Porter, M. D. *Anal. Chem.* **1999,** *71,* 4903-4908.

(24) Park, H.-Y.; Lipert, R. J.; Porter, M. D. In *Single-particle Raman Measurements of Gold Nanoparticles Used in Surface-enhanced Raman Scattering (SERS)-based Sandwich Immunoassays*, Optics East, International Society for Optics and Photonics: 2004; pp 464-477.

(25) Yakes, B. J.; Lipert, R. J.; Bannantine, J. P.; Porter, M. D. *Clin. Vaccine Immunol.* **2008,** *15,* 227-234.

(26) Yakes, B. J.; Lipert, R. J.; Bannantine, J. P.; Porter, M. D. *Clin. Vaccine Immunol.* **2008,** *15,* 235-242.

(27) Im, H.; Bantz, K. C.; Lindquist, N. C.; Haynes, C. L.; Oh, S.-H. *Nano Lett.* **2010,** *10,* 2231-2236.

(28) Wang, Y.; Becker, M.; Wang, L.; Liu, J.; Scholz, R.; Peng, J.; Gösele, U.; Christiansen, S.; Kim, D. H.; Steinhart, M. *Nano Lett.* **2009,** *9,* 2384-2389.

(29) Wells, S. M.; Retterer, S. D.; Oran, J. M.; Sepaniak, M. J. *ACS Nano* **2009,** *3,* 3845-3853.

(30) Zhang, Q.-X.; Chen, Y.-X.; Guo, Z.; Liu, H.-L.; Wang, D.-P.; Huang, X.-J. *ACS Appl. Mater. Interfaces* **2013,** *5,* 10633-10642.

(31) Liu, H.; Zhang, L.; Lang, X.; Yamaguchi, Y.; Iwasaki, H.; Inouye, Y.; Xue, Q.; Chen, M. *Sci. Rep.* **2011,** *1,* 112.

(32) Erlebacher, J.; Aziz, M. J.; Karma, A.; Dimitrov, N.; Sieradzki, K. *Nature* **2001,** *410,* 450-453.

(33) Orendorff, C. J.; Gole, A.; Sau, T. K.; Murphy, C. J. *Anal. Chem.* **2005,** *77,* 3261-3266.

(34) Wang, T.; Hu, X.; Dong, S. *J. Phys. Chem. B* **2006,** *110,* 16930-16936.

(35) Willets, K. A.; Van Duyne, R. P. *Annu. Rev. Phys. Chem.* **2007,** *58,* 267-297.

(36) Ko, H.; Singamaneni, S.; Tsukruk, V. V. *Small* **2008,** *4,* 1576-1599.

(37) Lu, Y.; Liu, G. L.; Lee, L. P. *Nano Lett.* **2005,** *5,* 5-9.

(38) Xu, S.; Ji, X.; Xu, W.; Li, X.; Wang, L.; Bai, Y.; Zhao, B.; Ozaki, Y. *Analyst* **2004,** *129,* 63-68.

(39) Shafer-Peltier, K. E.; Haynes, C. L.; Glucksberg, M. R.; Van Duyne, R. P. *J. Am. Chem. Soc.* **2003,** *125,* 588-593.

(40) Paxton, W. F.; Kleinman, S. L.; Basuray, A. N.; Stoddart, J. F.; Van Duyne, R. P. *J. Phys. Chem. Lett.* **2011,** *2,* 1145-1149.

(41) Simpson, L.; Melendres, C. *Electrochim. Acta* **1996,** *41,* 1727-1730.

(42) Leona, M.; Stenger, J.; Ferloni, E. *J. Raman Spectrosc.* **2006,** *37,* 981-992.

(43) Jorgensen, B. *The Theory of Dispersion Models*; Chapman & Hall: London, 1997.

(44) Watt, J. H.; Van den Berg, S. A. *Research Methods for Communication Science*; Allyn & Bacon: Boston, 1995.

(45) Barlow, R. J. *Statistics: A Guide to the Use of Statistical Methods in the Physical Sciences*; John Wiley & Sons: New York, 1989.

(46) Diamandis, E. P.; Christopoulos, T. K. *Immunoassay*; Academic Press: San Diego, 1996.

(47) Youden, W. *Ind. Eng. Chem. Res.* **1951,** *43,* 2059-2062.

(48) Harvey, D. *Modern Analytical Chemistry*; McGraw-Hill: New York, 2000.

(49) Youden, W. *Statistical Techniques for Collaborative Tests*; Association of Official Analytical Chemists: Washington, 1967.

(50) Cohen, E. R. *Meas. Sci. Technol.* **1998,** *9,* 1015.

(51) Ingamells, C.; Switzer, P. *Talanta* **1973,** *20,* 547-568.

(52) Zeisler, R. *J. Res. Nat. Bur. Stand.* **1986,** *91,* 75-85.

(53) Haiss, W.; Thanh, N. T.; Aveyard, J.; Fernig, D. G. *Anal. Chem.* **2007,** *79,* 4215-4221.

(54) Pinker, S. *The Better Angels of Our Nature: Why Violence Has Declined*; Viking Press: New York, 2011.

(55) Armbruster, D. A.; Pry, T. *Clin. Biochem.* **2008,** *29,* S49-52.

CHAPTER 3

UNDERSTANDING THE IMPACT OF NANOPARTICLE SEDIMENTATION ON THE PRODUCTION OF A SURFACE-ENHANCED RAMAN SCATTERING-BASED ASSAY

3.1 Introduction

Nanoparticles (NPs) have unique optical,[1-5] photothermal,[6-8] and magnetic[9-11] properties of importance in a range of fundamental and technical areas.[12-16] The research detailed herein is focused on understanding the impact of the transport process which controls the delivery of NPs in aqueous suspensions that are used as labels in heterogeneous immunoassays (e.g., surface-enhanced Raman scattering (SERS),[17-19] giant magnetoresistance (GMR),[20, 21] atomic force microscopy (AFM),[19] and aggregation-based detection methods[22, 23]).

Brownian motion indicates that the transport of NPs in a stable suspension should be controlled by diffusion.[24] However, repeated attempts to confirm that this point-of-view applies to the AuNPs (60-nm gold core) that we use as tags for captured antigens proved unsuccessful. We have found that suspensions composed of gold nanoparticle (AuNP)-based labels, used in our SERS immunoassay platform, indicate that AuNP accumulation surpasses predictions for transport controlled by diffusion.

The inability to verify that diffusion controlled the transport of AuNPs indicate that a range of other possible mechanisms, previously viewed as not significant, were operative. Experiments described in this chapter therefore examined the sensitivity of AuNP suspensions relative to stability in terms of aggregation and sedimentation. For this purpose, a range of surface modified AuNPs were constructed and characterized, with zeta potential, dynamic light scattering (DLS), and UV-Vis spectrophotometry used for suspension characterization. The possible impact of sedimentation which proved to be a dominate contributor to AuNP transport, was measured by optically monitoring settling rates that were than analyzed by the Mason-Weaver equation to calculate terminal sedimentation velocities.[25] Experiments were also carried out to further establish the impact of sedimentation by examining the differences in the signal generated in our SERS-based assay by positioning the capture substrate in different orientations to separate the contributions of diffusion and sedimentation on NP transport. These results, along with those that demonstrate the improvements in the quality of measurements not affected by sedimentation, are described.

3.2 Theory

3.2.1 NP Transport Kinetics

Transport kinetics for an NP suspension can be broken into three primary categories: gravitational settling, agglomeration, and fluid dynamics. We have assumed that the transport of NPs in a stagnant solution proceeds minimal particle-particle interactions. The transport of NPs in stagnant solution can then be defined by the combination of diffusional and sedimentation transport.

The Stokes-Einstein equation for diffusivity is given as:

$$D = \frac{k_B T}{6\pi\eta r} \tag{3.1}$$

where the diffusion coefficient D ($m^2\ s^{-1}$), k_B is the Boltzman constant (1.3807×10^{-23} J K^{-1}), T is temperature (K), η is the dynamic viscosity of the suspending fluid (kg $m^{-1}\ s^{-1}$), and r is the particle radius (m). Equation 3.1 describes the diffusion of a spherical particle in stagnant solution.

The root mean square distance $\langle\overline{x^2}\rangle$ traveled by an ensemble of particles in a one-dimension is given as:

$$\langle\overline{x^2}\rangle = 2Dt \tag{3.2}$$

This equation also describes the amount of time required for an ensemble of particles to travel a given root mean square distance. The relationship holds true for all directions, so $\langle\overline{x^2}\rangle = 2Dt$, $\langle\overline{y^2}\rangle = 2Dt$, and $\langle\overline{z^2}\rangle = 2Dt$. Equation 3.2 indicates that displacement from the origin increases with the square root of time.

NPs are also potentially susceptible to settling due to gravitational forces. The rate of particle settling is influenced by buoyancy, drag, and gravity. Stoke's Law describes the terminal settling velocity of a particle in a solution:

$$v_{sed} = \frac{2g(\rho_p - \rho_m)r^2}{9\eta} \tag{3.3}$$

where g is the acceleration due to gravity (m s^{-2}), ρ_p is the particle density (kg m^{-3}), and ρ_m is the media density (kg m^{-3}). Equation 3.3 shows that the rate of particle settling increases with both particle density and the square of the particle radius.

Equations 3.1 and 3.3 can be combined if NPs: (1) do not interact in the suspension solution, and (2) are affected by a uniform force, such as gravity. Under these assumptions, NP transport can be described by the Mason-Weaver equation:[25]

$$\frac{\partial C}{\partial t} = D\frac{\partial^2 C}{\partial z^2} + v_{sed}\frac{\partial C}{\partial z} \tag{3.4}$$

where C is the concentration of particles in the suspension (mol), t is time (s), and $+z$ is defined as the direction opposing the gravitational force. Equation 3.4 can also be written with the sedimentation velocity (v_{sed}) expressed as the product of the sedimentation coefficient (s) and gravitational force (g). This partial differential equation describes the movement of the particles in suspension as a function of both time and position relative to the $-z$ direction, which reflects the net transport of the NPs due to the settling caused by gravitational forces.

As constructed, this system is governed by the continuity equation in that the concentration of NPs throughout the suspension is assumed to change only as a function of the height of the suspension due to competition between gravity-induced sedimentation and the tendency of diffusion to restore uniformity. The continuity equation can be written

as:

$$\frac{\partial C}{\partial t} = -\frac{\partial J}{\partial z} \tag{3.5}$$

where J is the flux of the nanoparticles in the suspension relative to the z direction. Equation 3.5 can then be written to account for the change in concentration in a volume element, dV, with respect to the flux of points through the area, dS, bounding the volume element and is given in Equation 3.6:

$$\frac{\partial}{\partial t}\int_V C\, dV = -\int_S J \cdot \boldsymbol{n}\, dS \tag{3.6}$$

where $\boldsymbol{n}$ is the normal unit vector from the surface in the z direction. To use a finite difference method to solve Equation 3.6 the flux is discretized into a one-directional domain in the z-direction. The concentration of particles with in each finite volume element (ΔV) is given by the difference in the flux of particles entering ($J_{z,in}$) and leaving ($J_{z,out}$) each volume element:

$$\int_S J \cdot \boldsymbol{n}\, dS = J_{z,out} - J_{z,in} \tag{3.7}$$

The flux is therefore directly dependent on the length of the finite volume element (Δz), reducing the volume integral term of Equation 3.5 to:

$$\frac{\partial}{\partial t}\int_{V} C dV = \frac{\partial C}{\partial t}\Delta z \tag{3.8}$$

The integral conservation law can be used to rearrange the Equation 3.8 into a time evolution equation that is defined by the flux in the z-direction as given in Equation 3.9.

$$\frac{\Delta C_{element}}{\Delta t} = -\frac{J_{i,out} - J_{i,in}}{\Delta z} \tag{3.9}$$

where *i* indicates the element position.

The suspension height (H) was then discretized using a computational cell-centered method in which the particle concentration within each volume element is uniform. The flux at each of the surfaces of a volume element is then given, as in the Mason-Weaver derivation, by Equation 3.10.

$$J_i = -C v_{sed} - D\frac{\Delta C}{\Delta z} \tag{3.10}$$

The diffusion term is approximated using a second-order, central difference formula:

$$\frac{\Delta C}{\Delta z} = \frac{C_{i+1} - C_i}{\Delta z} \tag{3.11}$$

The model was solved with the no-flux boundary conditions, $J_{z=0,H} = 0$, and the discretized conservation equation for each volume element at each time step is given by:

$$\frac{\Delta C_i^n}{\Delta t} = -\frac{J_{i+1/2}^n - J_{i-1/2}^n}{\Delta z} \tag{3.12}$$

where *n* indicates the time step being evaluated.

The finalized form of the Mason-Weaver equation was numerically solved using a commercial software package (MATLAB R2012b, MathWorks Inc., Nattick, MA), using experimentally determined parameters where appropriate. Values for the terminal sedimentation velocity and the absolute suspension height were varied in an iterative process to determine the best fit parameters for experimental values based on a least squares approximation. Results for the model will be presented in Section 3.4.4.

3.3 Experimental

3.3.1 Reagents and Materials

Gold nanoparticles [60-nm diameter, 2.1 x 10^{10} particles/mL] were synthesized by BBI International (BBI) and obtained from Ted Pella. Dithiobis(succinimidyl propionate) (DSP), StartingBlock, modified Dulbecco's phosphate-buffered saline (PBS) packs (10 mM, pH 7.4), and borate buffer (BB) packs (50 mM, pH 8.5), are Thermo Scientific (Wilmington, DE) products. Tween 20 (T20), sodium chloride, and hydrogen peroxide (30%) from Fisher Scientific. Bovine serum albumin (BSA), acetonitrile (ACN), and sulfuric acid were obtained from Sigma-Aldrich (St. Louis, MO). Poly(dimethyl siloxane) (PDMS, SlyGuard), 200-proof ethanol (ACS grade, Pharmco-AAPER), octadecanethiol (ODT, Fluka), Contrad 70 (Decon), and optical adhesive 61 (Norland) were obtained from their respective venders or VWR (West Chester, PA). Human IgG (Pierce) and antihuman

IgG (Pierce) were purchased from Fisher Scientific. 5-5'-dithiobis(succinimidyl-2-nitrobenzoate) (DSNB) was synthesized by an earlier procedure.[17] All reagents were used as received.

3.3.2 NP-based SERS Immunoassay Platform

The NP-based SERS immunoassay platform is based on a solid-phase sandwich immunoassay and is depicted in Scheme 3.1. In this type of assay, a surface is first modified with a layer of capture antibodies (Abs). The surface is then exposed to a solution containing an antigen (Ag), which is selectively extracted from the solution by the capture Abs. Next, a rinse step removes excess solution and other materials from the surface. Finally, the substrate is exposed to a solution containing a label that selectively tags the captured Ags and another rinse step removes excess reactant.

To adapt the assay for SERS readout a thin (~200 nm) layer of smooth gold is used as the substrate and the labels, referred to earlier as ERLs, are composed of AuNPs coated with a Raman reporter molecule (RRM) and a layer of tracer Abs. For this study, the ERLs were prepared with a 60-nm AuNP core modified with the RRM DSNB and tracer Abs (antihuman IgG). The ERLs produce a SERS signal that is proportional to the amount of antigen in a solution.

3.3.3 Preparation of the Capture Substrate

Detailed procedures for fabricating the capture substrate have been described previously.[26] Briefly, template stripped gold (TSG) was used as the base for the capture substrate. The process for preparing TSG produces an atomically smooth, glass-supported

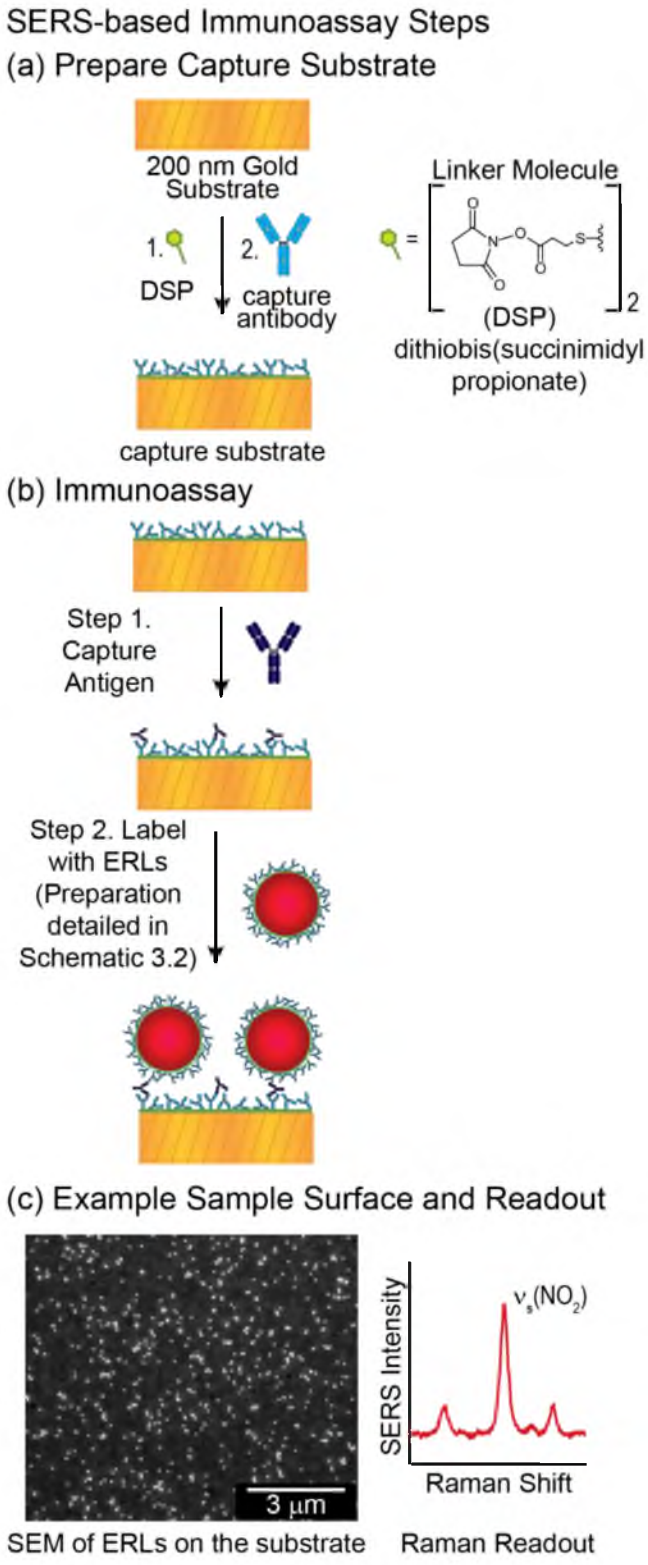

Scheme 3.1. NP-based SERS sandwich immunoassay platform.

gold surface that facilitates imaging captured NPs. To prepare TSG, 200 nm of gold (99.9% purity) was deposited onto a 4" p-type silicon <100> wafer via vapor deposition using an Edwards 306A resistive evaporator. The glass squares, cut as 1 × 1 cm sections from carefully cleaned microscope slides, were then affixed to the surface of the exposed gold with optical adhesive 61. After curing for 4.0 h under UV light, the glass squares were detached from the surface by applying light pressure to the edge of the squares. This step exposes the underlying atomically smooth gold substrate.

The gold substrate was then immediately modified by using microcontact printing to form a circular hydrophobic boundary with a PDMS stamp that had a 2-mm diameter hole in its center, the stamp was inked with a layer of 2.0 mM ethanolic ODT that was subsequently dried by N_2. The unmodified 2-mm address is modified with a 1-mM solution of DSP in ethanol (14 to 16 h), and the substrates were removed from the DSP solution, rinsed with 200 proof EtOH, and thoroughly dried with N_2. Capture Abs were then immobilized via electrostatic interactions with a 20 μL droplet of 2.5 μg/mL solution in 10 mM PBS with 0.1% T20 (PBST) by a 7-h incubation step carried out in a humidity controlled (97% relative humidity) environment at room temperature. The substrates were rinsed with 2 mL of PBST immediately before moving to the Ag capture step.

3.3.4 Preparation of Extrinsic Raman Labels (ERLs)

ERLs were prepared from 60-nm (nominal) diameter citrate-capped AuNPs. The AuNPs are the core for the ERLs and were modified with a RRM and a tracer antibody to produce a Raman-active and immunologically specific label. ERLs are designed to produce a strong Raman signal for assay readout and have selective recognition of a desired antigen.

Along these lines, DSNB was designed to provide two functional components: (1) a disulfide moiety that produces a chemisorbed thiolate monolayer on the surface of the AuNP and (2) a nitro group that has an intrinsically strong Raman scattering cross section centered at 1336 cm^{-1} based on the symmetric nitro stretch.

The production steps for ERLs are summarized in Scheme 3.2. Initially, the AuNPs suspension was adjusted to contain 2.0 mM BB by adding 40 μL of 50 mM BB to 0.96 mL of AuNP suspension. The AuNPs were then modified by adding 10.0 μL of DSNB to 1.0 mL of the buffered AuNP suspension. The resulting thiolate monolayer was allowed to assemble at room temperature onto the surface for 7 h on a horizontal rotator plate. Then 10.0 μL of a 2.5 μg/mL solution of purified antihuman IgG (α-HIgG) Abs were added to the suspension and allowed to react at room temperature for 16 h on a horizontal rotator. The surface of the modified AuNPs was then blocked by incubating BSA in a 1.0% (w/v) BSA solution (2.0 mM BB) at room temperature for 7 h on a horizontal rotator.

Excess and unreacted materials were removed from the suspension via three centrifugation, decanting, and resuspension steps. The centrifugation step was performed at 2026*g* for 10 min to settle the modified AuNPs on the bottom of the centrifuge tube. The supernatant was decanted, leaving the modified AuNPs behind in a minimal volume (~40 μL). The modified AuNPs were resuspended with 1.0 mL of 1.0% (w/v) BSA in 2.0 mM BB. These steps were repeated with new aliquots of the AuNP solution, with a final set of preparation steps designed to yield an AuNP concentration ~16× (~3.2 x 10^{11} particles mL^{-1}) its initial level with a NaCl concentration of 0.15 M to mimic physiological conditions. This suspension was used in all of the assays, whereas an ERL concentration of ~2 × 10^{10} particles mL^{-1} were employed in the particle characterization stages.

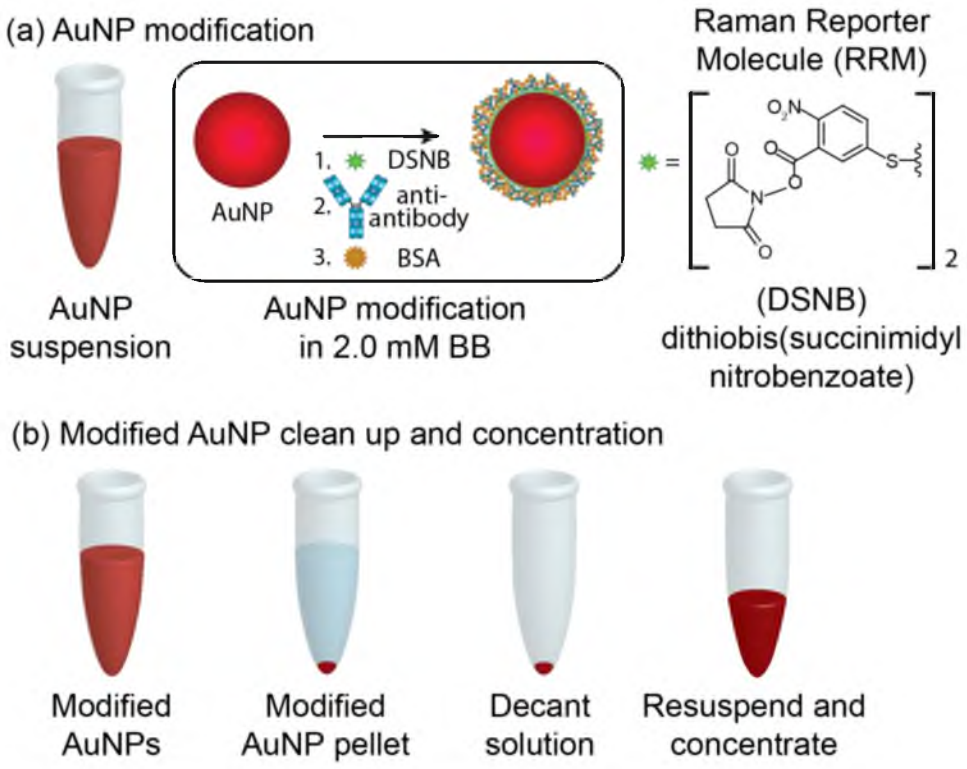

Scheme 3.2. ERL preparation.

Concentrations of BSA in the suspension solutions is defined by the number of BSA monolayers available relative to the NP surface area. This is done due to the discovery of the ERL stability being related to the ratio of BSA monolayers relative to the total AuNP surface area (dependent on the AuNP concentration) rather than the solution based concentration.

The BSA quantities in the Results section are expressed as the number of BSA monolayers in suspension solution relative to the AuNP surface area. First, the AuNP surface area is calculated assuming all particles are 60-nm diameter spherical particles. Second, the number of BSA molecules per an AuNP was determined by taking the Stokes radius of BSA as 3.48 nm[27] and assuming that the molecules arrange on the surface as hexagonally closest packed circles, which give a 90.96% coverage of the surface area.[28] These assumptions indicate that a single AuNP has ~270 BSA molecules on the surface and is equal to 1 BSA monolayer. The AuNP stock suspension measured as 2.1×10^{10} particles mL^{-1} via UV-Vis analysis[29] and the number of BSA monolayers in the final ERL suspension can be calculated as 1.28×10^{5}.

3.3.5 SERS-based Immunoassay and ERL Labeling Protocol

The immunoassay was performed by incubating the capture substrate with a 20.0-μL drop of H-IgG diluted in 10 mM PBS with 0.1% Tween 20 (PBST) to yield 1.0 and 5.0 ng/mL concentrations. The H-IgG was incubated on the surface of the substrate for 7 h in the upright position in a humidity controlled environment at room temperature. The samples were then rinsed three times with 2.0 mM BB with 0.1% (v/v) Tween 20:150 mM NaCl. A 20.0 μL drop of freshly prepared ERLs was then placed on the surface and the

substrate was incubated in the upright or inverted position for intervals from 30 s to 16 h in a humidity chamber at room temperature. The assay substrate was rinsed three times with 2.0 mL 2.0 mM BB with 0.1% (v/v) Tween 20:10.0 mM NaCl. The samples were allowed to dry under ambient conditions. Note that due to handling variations the incubation times of H-IgG steps are accurate to ± 1 min of the indicated time and the ERL steps are accurate to ± 5 s of the indicated incubation times.

3.3.6 Zeta Potential and Dynamic Light Scattering (DLS) Measurements

Zeta potential is the measure of the electrokinetic potential, commonly referred to as the surface potential, that provide insights into the charge on the particle surfaces and how the charge influences electrostatic interactions between suspended NPs. Surface potentials greater than ±30 mV are usually sufficient to be considered electrostatically stabilized for these types of suspensions, as long as the presence of ionic components (for example, NaCl) in the suspension are taken into account.[30]

DLS determines the average hydrodynamic diameter of modified suspended NP.[31] Average hydrodynamic diameter results are plotted based on the intensity based measurement of the z-average and standard deviations from five measurements of the same suspension and the distributions of particle diameters are discussed where necessary (in Section 3.4.3). These measurements were used to examine the possible aggregation of the NPs and how it may effect suspension stability.[32]

The surface potential and the hydrodynamic diameter for the AuNP suspensions were determined using a Malvern Zetasizer Nano-ZS. Comparative measurements were

made with the as-received AuNPs. Modified AuNPs (prepared before adjusting the suspension solution with 0.15 M NaCl) and ERLs (fully prepared ERLs in 0.15 M NaCl) were characterized at a concentration of ~2 x 10^{10} particles mL^{-1}.

Measurements were collected for a duration of 24 h with a 1 h incremental breaks between measurements for a total of 23 measurements. The suspension properties were measured five times at each point. Data presented is shown in Section 3.4.3 as the average and resulting standard deviation for each measurement.

3.3.7 UV-Vis Measurements

UV-Vis spectra of AuNP suspensions were collected on a Cary UV-Vis-NIR 3000, which was used to collect data in the visible spectrum between 350-700 nm in 15 increments. As-received AuNPs were analyzed without any modifications at the stock concentration 2.1 x 10^{10} particles mL^{-1}. Modified AuNP and ERL suspensions were run at concentrations similar to the stock concentration of ~2 x 10^{10} particles mL^{-1} with the specified number of BSA monolayers. A specially adapted reduced volume quartz cuvette with a 2-mm wide solution chamber and a 5mm path length was employed (Figure 3.1). The cuvette was filled with 145 μL of freshly prepared and evenly dispersed suspension, tightly sealed with several layers of parafilm to minimize evaporation. The height of the liquid in the cuvette was ~14.5 mm. A 2.0-mm high sample window was positioned 1.5 mm below the top of the liquid suspension. The window was defined by masking with a flat black paint. Note that the positioning of the sample window at the top of the liquid reduces the analysis time of each experiment, which typically range for 80 h. The UV-Vis spectra were collected every 15 min until the NPs had completely moved out of the

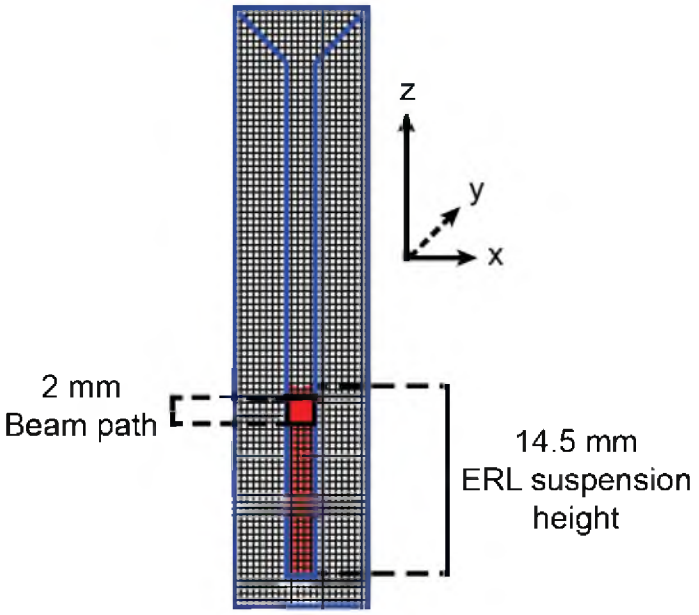

Figure 3.1. Quartz cuvette setup for UV-Vis measurements designed to monitor the diffusion and sedimentation based transport of AuNPs within a given sample window.

observation window.

3.3.8 Instrumentation and Data Analysis

Raman spectra were obtained using either a modified NanoRaman spectrometer (Concurrent Analytical, Loveland, CO)[33] or a DXR Raman microscope (Thermo Scientific). The modified NanoRaman spectrometer has three primary components: laser excitation source (He:Ne laser, 22mW), spectrograph (f/2.0 Czerny Tunrer imaging spectrometer (6-8 cm^{-1}) resolution and a Kodak 0401E charge coupled device (CCD) thermoelectrically cooled to 0°C), and fiber optic probe. Raman spectra were collected by irradiating the sample surface with a 20-μm diameter laser spot at 3.0 mW and a 1-s integration time. The laser power was found to vary no more than ±0.1 mW after warmup. Sample data was collected at 10 separate locations on each substrate. All spectra were baseline corrected. The height intensity of the symmetric nitro stretch, $\nu_s(NO_2)$, at 1336 cm^{-1} was used for quantification.

High density Raman maps of the sample substrates were colleced using a Thermo Scientific DXR Raman microscope. This instrument consists of four primary components: laser excitation source (HeNe laser, 8 mW), spectrograph (CCD detector thermoelectrically cooled to -65 °C), fiber optic probe, and optical and Raman compatible objectives. The optical/Raman microscope was fitted with a 5x Olympus MPlan N objective that gave a 5-μm diameter laser spot size. The instrument has a motorized sample stage (5" × 3" travel dimensions in the X and Y directions, respectively, with a ±1-μm step size resolution), allowing for automated high density data collection. Spectra were obtained at 50-μm steps across the sample at 3.00 ± 0.01 mW laser power and a 50-μm slit width spectrograph

aperture.

3.4 Results and Discussion

3.4.1 As-received AuNP Properties

Modified AuNPs (DSNB, tracer Ab, and BSA modified AuNPs) and ERL (DSNB, tracer Ab, and BSA modified AuNPs with 0.15 M NaCl in the suspension solution) suspensions were characterized using zeta potential, DLS, UV-Vis spectrophotometry, and sedimentation-based simulations as described in Sections 3.4.2 to 3.4.4. This section summarizes the result found for characterization of as-received AuNP suspensions for comparative purposes. Zeta-potential for the AuNPs averaged over the 24-h observation period was −57 ± 1 mV. The plot of the hydrodynamic diameter distribution had a mean and standard deviation of 59 ± 27 nm that changed in 24 h to 56 ± 22. UV-Vis spectrophotometry was also used to determine the average AuNP size as well as the suspension concentration.[29] The extinction maximum occurred at 535 nm, equating to an average AuNP diameter of 58 nm, and a concentration of 2.1×10^{10} particles mL^{-1}. Fits to the Mason-Weaver simulations (see Section 3.4.4) yielded a size of 56 nm and a terminal sedimentation velocity of 3.5×10^{-8} m s^{-1}.

3.4.2 Modified AuNP and ERL Suspensions: Zeta Potential Analysis

Zeta-potential measurements for the modified AuNP and ERL suspensions were collected over a 24-h period. The results show that the zeta-potential (Figure 3.2a) for the modified AuNPs are all consistently lower in magnitude relative to the as-received AuNPs.

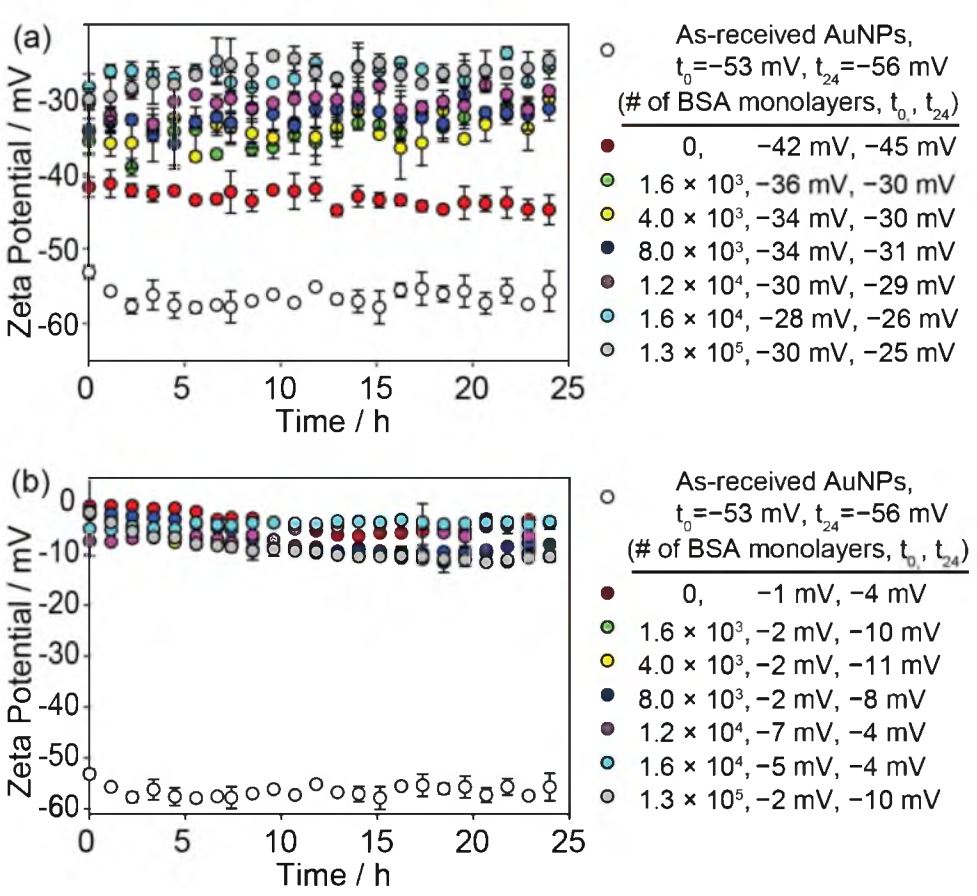

Figure 3.2. Zeta potential measurements of (a) modified AuNP, and (b) ERL suspensions. Zeta potential measurements for as-received AuNPs are shown for reference. Values for zeta potential at the start (t_0) of the analysis and at the end (t_{24}) are shown in the figure legend.

The modified AuNPs without BSA have an average zeta-potential of −43 ± 1 mV over the same time period. The zeta-potential moves to more positive values with the addition of BSA. The change with the lowest level of BSA (1.6×10^3 BSA monolayers equivalent) is initially 34 ± 2 mV mV evolving to a slightly more positive value (30 ± 1 mV mV) in 24 h. The addition of higher levels of BSA 4.0×10^3 to 1.3×10^5 monolayer equivalents pushes the zeta-potential by at most another 7 mV changing by +2-3 mV in 24 h. These data indicate an electrostatic destabilization of the modified AuNPs with increases in the level of BSA.

After adding NaCl to a final concentration of 0.15 M, the zeta-potentials for the ERL suspensions decreased to −12 mV (Figure 3.2 b). These zeta-potentials again signify a possible decrease in the charge-based stability of the ERLs. However, the addition of a charge carrier (NaCl) to the solution can alter the accuracy of these measurements, limiting their predictive value.[30, 34]

3.4.3 Modified AuNP and ERL Suspensions: DLS Analysis

DLS measurements indicate an increase in the hydrodynamic diameter of the as-received AuNP after modification with DSNB and tracer Abs, as well as after the addition of BSA. The DLS data in Figure 3.3 indicates a 13 nm increase in hydrodynamic diameter to 70 ± 1 nm after the addition of DSNB and the tracer antibody in comparison to the as-received AuNPs (57 ± 1 nm). The increase in diameter is consistent with that expected for the addition of a small molecule (DSNB) and Ab (~10 nm diameter).[35] The hydrodynamic diameter after the addition of BSA results in a further increase in hydrodynamic diameter, which, for all BSA levels, slowly approaches ~77 nm in 24 h. This

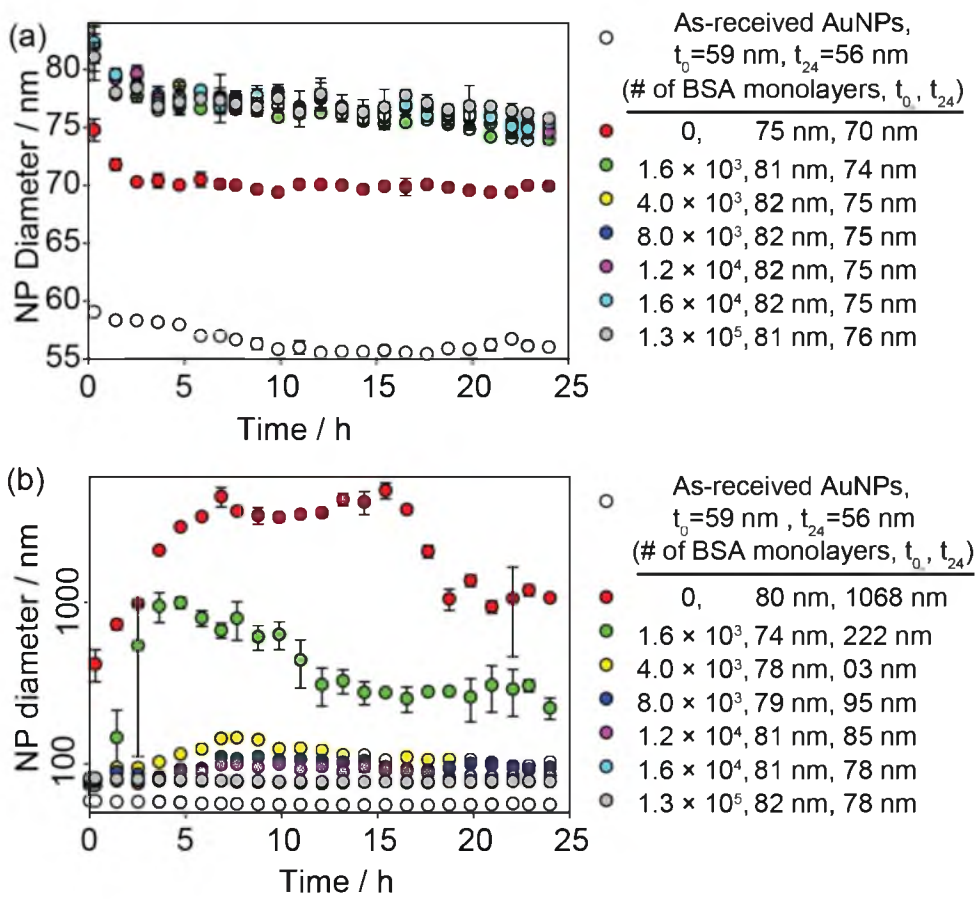

Figure 3.3. DLS measurements of the intensity-based average hydrodynamic diameter for (a) modified AuNP suspensions, and (b) ERL suspensions. Average hydrodynamic diameters for as-received AuNPs are shown for reference. Values for zeta potential at the start (t_0) of the analysis and at the end (t_{24}) are shown in the figure legend.

is consistent with the 3.5 nm diameter BSA.[27]

ERL suspensions have a much larger variation in the measured size stability with respect to the amount of added BSA. Without BSA, the suspension is highly unstable; with respect the average hydrodynamic diameter increases from by approximately a factor ~5to ~50 during the 24 h measurement. The dramatic increase triggers warnings from the instrument, for example, poor data quality and sedimentating particles, and the resulting micron-wide diameter distributions clearly signal aggregate formation. We note that the drop in diameter after ~16 h arises from the loss NP aggregates due to sedimentation. Sedimentation is also indicated by a clear suspension at the end of the measurement.

3.4.4 NP Transport by Diffusion and Sedimentation

This Section quantifies the sedimentation of ERLs using UV-Vis spectrophotometry and an iterative least squares approximation of the Mason-Weaver model solved using MATLAB. First, the accuracy of the Mason-Weaver simulation for NP transport due to diffusion and sedimentation was tested by monitoring transport for the as-received AuNP, which have an average diameter of 59 nm from DLS and 58 nm per the position of the optical extinction maximum. The AuNPs were transferred into the quartz cuvette, after acid cleaning, shown in Figure 3.1.

The spectrophotometer was programed to collect spectra from 440-580 nm (3-nm resolution) every 15 min for 80 h (the data is shown for 1 h increments). The results of these measurements are shown in Figure 3.4, after normalization of the spectrum at time zero. Note that the extinction decreases for the first 60 h at which time the extinction has reached an immeasurable level. The calculated normalized AuNP concentrations versus

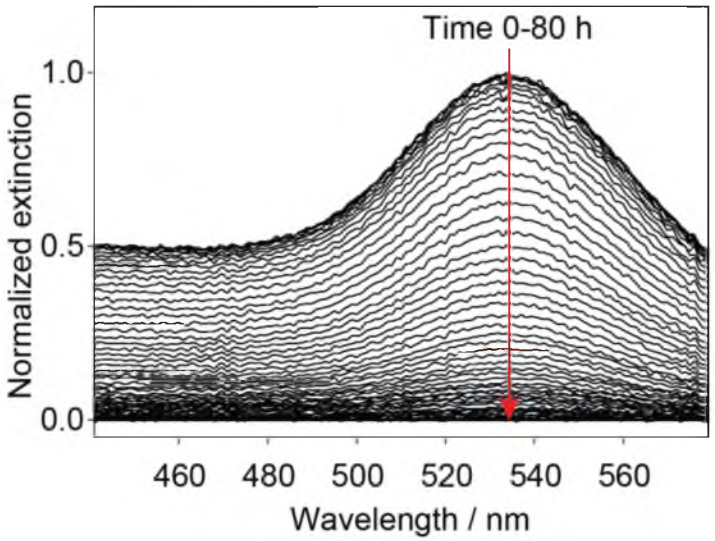

Figure 3.4. UV-Vis spectra of stagnant suspension as-received 60-nm AuNPs with the specialized sample cuvette described in Figure 3.1. Data is shown for 1 h intervals for an 80-h duration. The spectra were baseline corrected and normalized based on final and initial suspension measurements, respectively.

the 80-h duration of the measurement are shown in Figure 3.5 by the blue open circles. The normalized concentrations were determined using the progression of the spectral data at 535nm, the extinction maximum.

Next, an iterative least squares approximation to the Mason-Weaver simulation was performed by inputting the values of the Boltzmann constant (1.38×10^{-23} kg m^2 s^{-2} K^{-1}), dynamic fluid viscosity (8.9×10^{-4} kg m^{-1} s^{-1}), AuNP density (1.92×10^4 kg m^{-3}),[36] density of water (9.9×10^2 kg m^{-3}), gravitational acceleration (9.81 m s^{-2}), temperature (298.15 K), suspension height (1.45×10^{-2} m), and the UV-Vis window location (from 1.30×10^{-2} to 1.45×10^{-2} m) relative to the suspension (1.10×10^{-2} m to 1.10×10^{-2} m). Based on the anticipated diameter of the as-received AuNPs, the model iterated the results for 45 to 65 nm AuNPs in 1 nm steps. The simulation results produces profiles for the net transport of AuNP of different diameter as a function of time. The net flux shows a decrease in AuNP concentration for the duration of the first ~60 h of analysis, in general agreement with the experimental results. Application of a least squares approach gave the best fit for the AuNPs in the suspension of 56 nm, which agrees well with the diameters found by two different experimental measurements and support the reliability of the Mason-Weaver simulation. It is also worthwhile to note that the shape of the AuNP sedimentation curve produced by the simulation matches that measured experimentally and indicates that the sedimentation rate monitored by the designated observation window has three distinct regions. There is an initial region that remains constant for ~5 h. This is followed by a second region (5 to 30 h) in which there is a decrease in the AuNP concentration, and then a final region (30 to 60 h) in which the AuNP concentration undergoes slower decay. This profile can be explained by examining the evolution of the AuNP concentrations

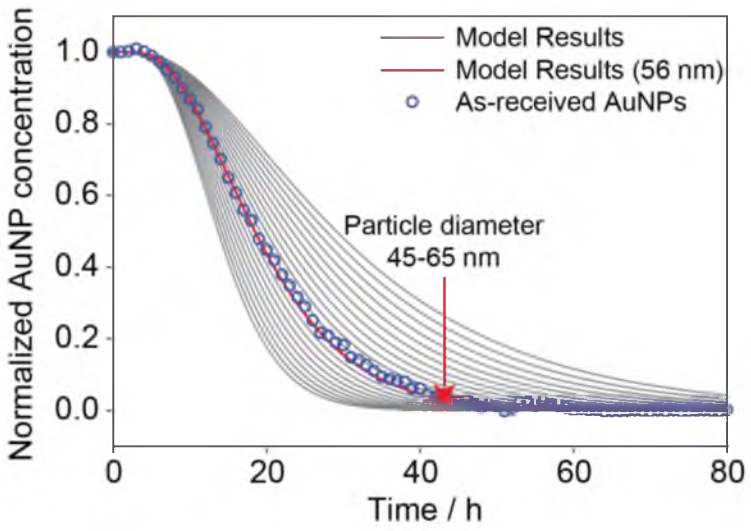

Figure 3.5. UV-Vis experimental data collected for sedimentation of as-received 60 nm AuNPs. Data is the normalized AuNP concentration calculated from data in Figure 3.4. Blue circles represent the experimental data collected while the grey lines indicate simulation results for the Mason-Weaver model. The red line indicates model results for AuNPs with a 56-nm diameter from the least squares approximation to the Mason-Weaver model.

throughout the entire height of the suspension as described by the Mason-Weaver model. These model results are shown by the 3D plots in Figure 3.6. The slow initial onset of sedimentation at the top of the suspension represents the time required for a measurable change in AuNP levels to reach the top of the observation window (13 mm). Up to this point, the number of AuNP moving out of the window roughly equals to the number of AuNPs settling into the window. Once the sedimentation reaches the observation window, a decrease in the AuNP concentration is observed as they settle out of the window at a fairly steady rate. The final section of the curve shows a gradual slowing of the rate of decrease in remaining ~5% of the AuNPs in the suspension. This reflects the concentration gradient caused by the sedimentation of the AuNPs, which increases the diffusion of AuNPs directed upward against gravitational force. The sedimentation model does not actually reach a value of zero for the AuNP even after a 250-h simulation. An incremental decrease in concentration is still underway, but is so small that it is undetectable by the spectrometer.

After the validation of the Mason-Weaver model, experiments were ran for empirical analysis of modified AuNP and ERL suspensions without BSA and at monolayer equivalents of 1.60×10^4, and 1.28×10^5. The normalized AuNP sedimentation curves produced are shown in Figure 3.7. All of the results indicate that the NP transport curves used to determine the terminal sedimentation velocities are dependent on BSA levels.

To obtain a least squares best fit to the Mason-Weaver model in order to quantify the terminal sedimentation velocity, the suspension height terminal sedimentation velocity was varied from 14.5 to 14.3 mm and 1.0×10^{-8} to 6.0×10^{-8} m s^{-1}, respectively. The 0.3 mm variation is the suspension height results from potential changes in the meniscus level,

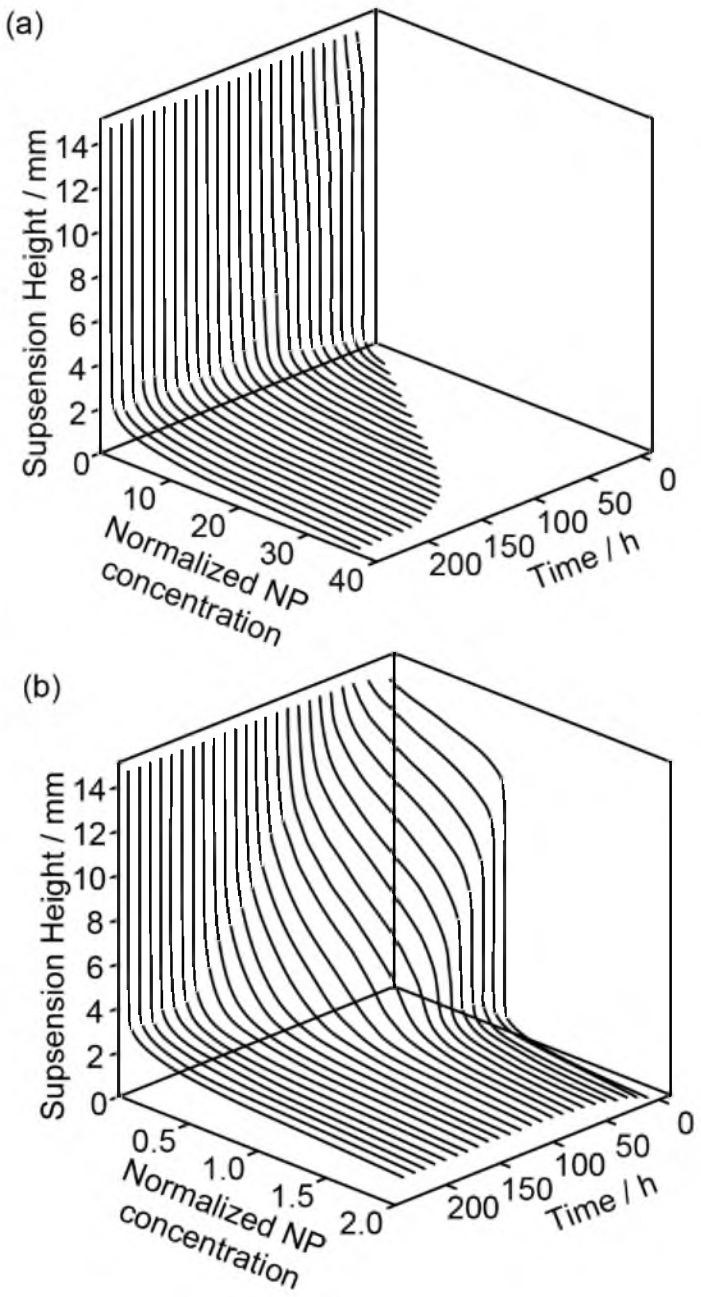

Figure 3.6. Mason-Weaver 60-nm AuNP transport sedimentation model results. The suspension height plotted versus normalized AuNP concentration and time. The suspension starts at time zero, which is a homogenous distribution of AuNPs from the top of the cell to the bottom (not shown). Over time, the distribution of AuNPs in the suspension shifts due to diffusion and sedimentation. The normalized AuNP concentration profile indicates that sedimentation causes the AuNPs to accumulate in the bottom of the suspension at high concentrations.

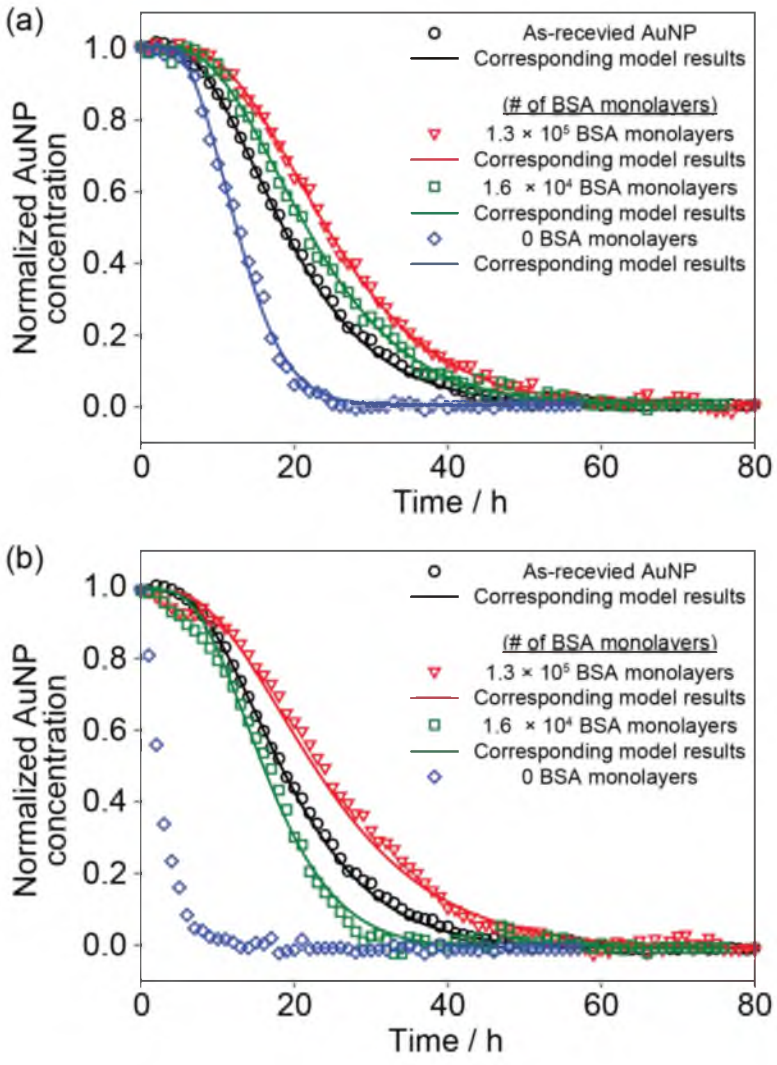

Figure 3.7. Normalized AuNP concentration for 0, 1.60×10^4, and 1.28×10^5 BSA monolayers suspension based on UV-Vis spectra and least squares approximation to the Mason-Weaver solutions for AuNP transport. (a) Modified NPs suspensions show terminal sedimentation velocities of 5.4×10^{-8}, 3.0×10^{-8}, and 2.9×10^{-8} m s^{-1}, respectively. (b) ERL suspensions show terminal sedimentation velocities of not determine, 3.8×10^{-8}, and 2.7×10^{-8} m s^{-1}, respectively. The terminal sedimentation velocities for the ERL suspension with 0 BSA monolayers could not be determined due to a fluctuating AuNP size determination during sedimentation. The BSA levels are expressed as the number of BSA monolayers in suspension. As-received AuNP suspension is shown for reference.

which is impeded from visual inspection due to the cuvette masking used to define the sample window.

The terminal sedimentation velocity of the as-received AuNPs was calculated to be 3.6×10^{-8} m s^{-1}, based on the solution to the Mason-Weaver equation and a particle diameter of 56 nm. The results also show that modified AuNPs have terminal sedimentation velocities that decrease with increasing levels of BSA. The terminal sedimentation velocities for BSA levels of 0, 1.6×10^4, and 1.28×10^5 BSA monolayer equivalents for modified AuNPs are 5.4×10^{-8}, 3.0×10^{-8}, and 2.9×10^{-8} m s^{-1}, respectively, with the latter two terminal sedimentation velocities effectively the same.

The ERL suspensions for 1.6×10^4 and 1.28×10^5 BSA monolayers show similar trends in the velocities of 3.8×10^{-8}, and 2.7×10^{-8} m s^{-1}, respectively. We were unable to fit the data for the ERLs in the absence of BSA due to their size instability as found by the DLS measurements. The ERL suspension with 1.28×10^5 BSA monolayers displays slightly lower terminal sedimentation velocity than the as-received AuNPs, indicating reasonable sedimentation stability. This suspension was used in the NP-based SERS immunoassay results discussed in Sections 3.4.5 and 3.4.6.

The differences in the terminal sedimentation velocities can be used to project a value for the normalized NP concentration increase in the lower 1 μm portion of the solution that would occur near the surface of the capture substrate by the end of a 16-h ERL incubation. Our NP-based immunoassays incubate a 20-μL droplet with the capture substrate. Therefore, the suspension volume was modeled as a 20-μL cylinder with a 2-mm diameter. The Mason-Weaver model predicts that the measured terminal velocities for modified AuNPs with 0, 1.6×10^4, and 1.28×10^5 monolayers equivalents of BSA and

ERL suspensions with 1.6×10^4, and 1.28×10^5 BSA equivalents would have normalized NP concentration increases of 23, 8.3, 7.9, 12, and 7.0, respectively. These numbers are an indicator for the potential number of ERLs settled on a SERS substrate and point to a possible explanation of the level, at least in part, of nonspecific ERL adsorption in these measurements, which is now examined.

3.4.5 ERL Transport to SERS-based Immunoassay Substrate

To determine how the inherent sedimentation of ERLs affects the NP-based immunoassay readout, ERL incubations in upright and inverted positions were compared. With sedimentation following the direction of gravity, upright ERL incubations direct sedimentation to the substrate while an inverted ERL incubation direct the sedimentation away from the substrate. SERS capture substrates with Ag concentrations of 5.0, 1.0, or 0 ng/mL H-IgG were exposed to ERLs in the upright and inverted positions between 30 s to 16 h. ERL suspension used for these experiments was chosen based on the highest stability found earlier with respect to aggregation and sedimentation (a BSA level of 1.38×10^5 monolayer equivalents, at 3.2×10^{11} particles mL^{-1}). Figure 3.8 summarizes the results using average and standard deviations of the signal strength of the 1336 cm^{-1} [$\upsilon_s(NO_2)$] peak of the RRM layer prepared from DSNB.

The data for the three different H-IgG concentrations were examined to determine if a linear $t^{1/2}$ dependence (Figure 3.8c and 3.8d), which indicates diffusional transport, were evident. The $t^{1/2}$ data for the upright incubation (Figure 3.8c) shows clear deviations from linearity, which is supported by the residuals plot in Figure 3.8e. Note that the response measured for the negative control samples (PBST only) also fails to follow a $t^{1/2}$

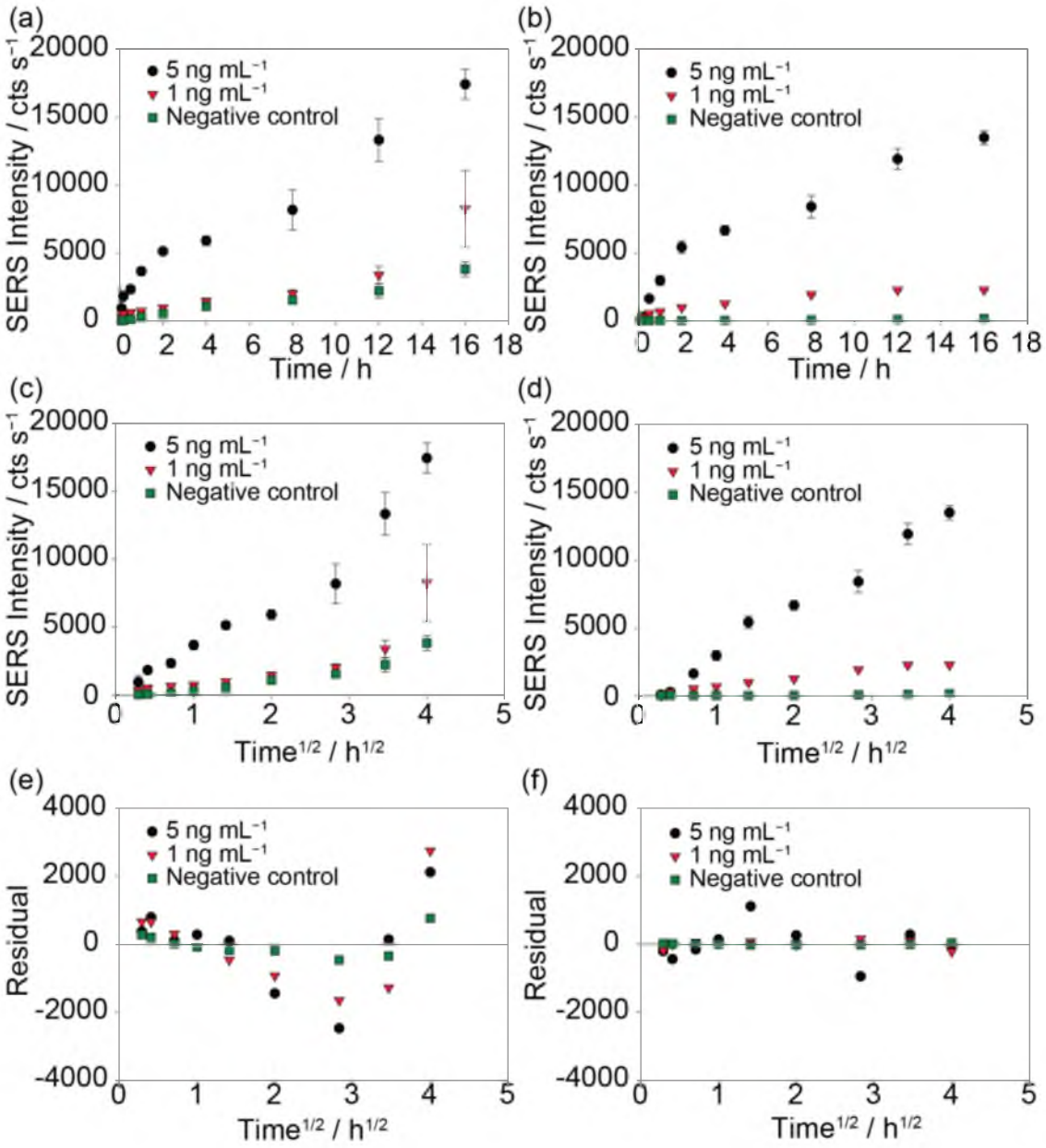

Figure 3.8. SERS-based immunoassay for human IgG in PBST. Dose-response plot for five separate calibration runs for human IgG (1 and 5 ng/mL) and a negative control sample with ERLs incubated in the upright (a) and the inverted (b) incubation positions. Dose-response plot for human IgG calibration versus $t^{1/2}$ for an upright (c) and inverted (d) ERL incubation. Residuals for linear fit to a $t^{1/2}$ dependence for upright (e) and inverted (f) ERL incubations.

dependence.

The same experiments were performed with SERS substrates for the ERL incubation in the inverted position. The results (Figure 3.8d) show a lower SERS signal intensity, and thus a lower accumulation of ERLs. The data (shown in Figure 3.8d and 3.8d) indicates a linear $t^{1/2}$ dependence and thus supports diffusional transport. The most significant decrease in the overall accumulation is observed for the negative control substrates (PBST only), which have an almost immeasurable response at all incubation times. This decrease in nonspecific adsorption clearly demonstrates the detrimental impact of sedimentation in the upright position. The inverted substrates also have smaller coefficients of variance, which indicates a greater reliability as well as the existence of a diffusional dependence on accumulation.

3.4.6 Distribution of SERS Response on the Substrate

SERS maps of two representative sample substrates (5 ng mL^{-1} H-IgG) that were incubated for 16 h with ERLs in the upright or inverted position are shown in Figure 3.9. These maps were produced by collecting spectra in 50 μm steps with a 5-μm diameter laser spot size. The results are visually represented as the signal intensity of the strongest Raman feature at 1336 cm^{-1} that were normalized to the average signal on the substrate. The high density maps highlight the differences in the signal distribution on the SERS substrates produced by the upright versus inverted configurations.

The color plot of the "inverted" SERS data (Figure 3.9a) shows large signal variations across the substrate. These deviations became more evident by converting from Cartesian to polar coordinates so that the normalized signal can be plotted versus the radial

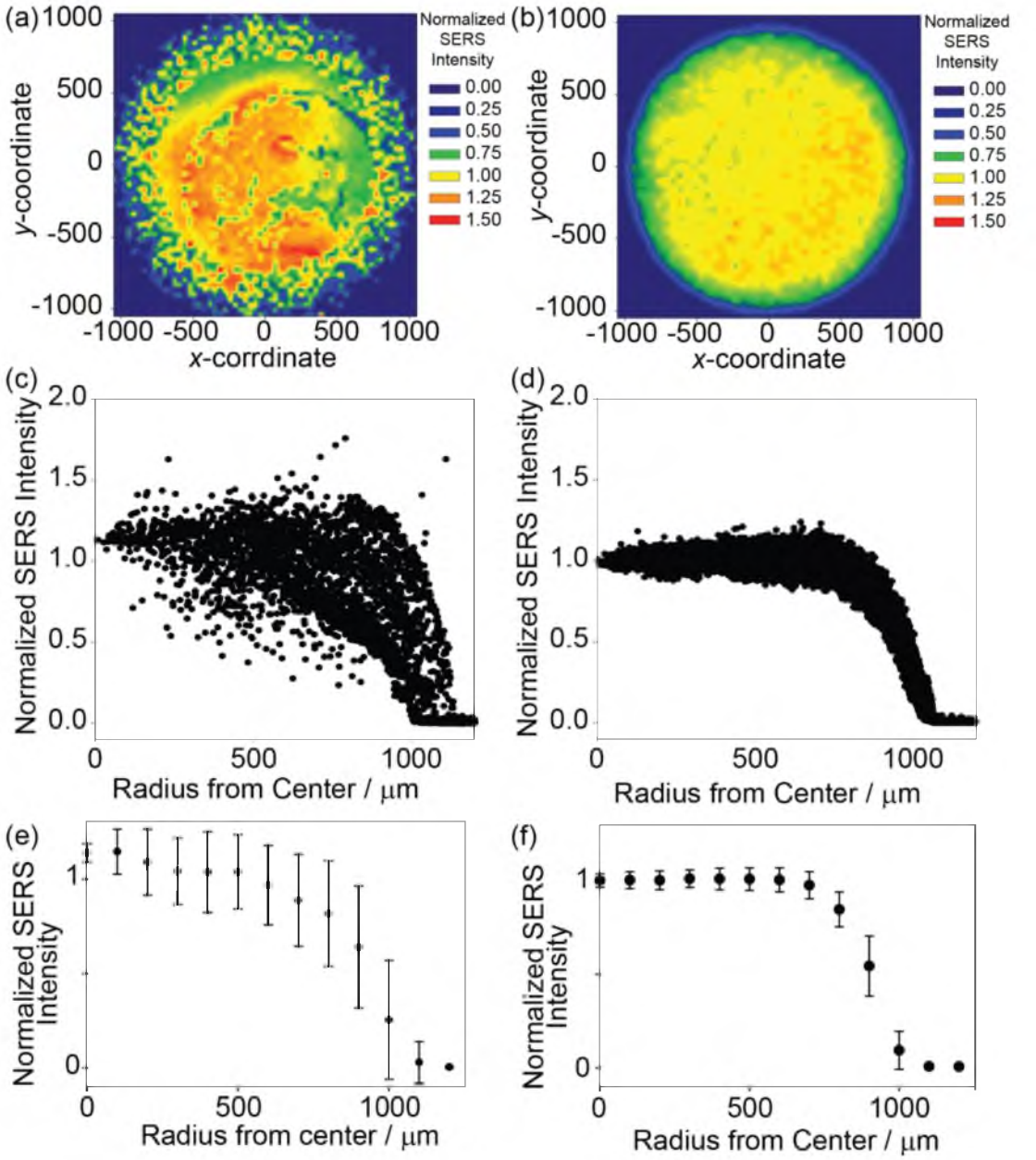

Figure 3.9. High density Raman surface analysis for 5 ng/mL of human IgG immunoassay substrates in upright and inverted ERL incubation position. The high density map consists of 50 ± 1 μm steps on the surface taken at 3 mW of power with a 5× Olympus objective with a 5 μm spot size. (a) Representative sample substrate with a SERS signal intensity normalized to the average SERS signal from the inner 1.6 mm diameter radius of the substrate from an upright and (b) inverted ERL incubation. (c) Normalized signal intensities versus the radial component of polar coordinates showing differences in the signal variation for an upright and (d) inverted ERL incubation. (e) Average and standard deviation of the average normalized SERS intensity for concentric and separate rings for upright and (f) inverted ERL incubation.

distance from the center of the circular address. This data is plotted in Figure 3.9c and 3.9d as the average and standard deviation for 100-μm wide concentric rings moving out from the center of each address. Analysis indicates a large variability in the SERS signal for the upright incubation relative to inverted position.

The inverted ERL incubation shows a relatively even distribution of the SERS signal across the substrate surface. The color plot shows a majority of the surface with a yellow color with some orange on one side and a little green on the other, indicating a small signal gradient, but a relatively consistent signal. The conversion of the data to polar coordinates indicates a tighter variation in the signal.

3.4.7 Equilibrium Between Sedimentation and Diffusion

The data in Section 3.4.7 demonstrates the ability of a method to direct the inherent sedimentation of the ERLs away from the substrate in order to reduce nonspecific adsorption and more evenly distribute ERLs on the surface via diffusional-based transport. Ideally, the AuNP core of the ERL could be altered to increase stability with respect to sedimentation, eliminating the need for inversion during the ERL incubation. To determine the most effective method to reduce sedimentation, particle transport reinvestigated from a mathematical standpoint.

The transport of particles is described in Section 3.4. The net transport of the particles is based on the net flux of particles in the z direction as described by Equation 3.10 $J_z = -Cv_{sed} - D\Delta C/\Delta z$. When the net flux J_z is equal to zero, sedimentation flux (Cv_{sed}) of the NPs equals the negative of the diffusional flux ($D\Delta C/\Delta z$). When this is true, the opposing forces of sedimentation and diffusion are at equilibrium.

A mathematical expression of the particles at equilibrium can be found by substituting Stoke's law from Equation 3.3 $[2g(\rho_p - \rho_m)r^2/9\eta]$ for v_{sed} and Stokes-Einstein equation in Equation 3.1 ($k_BT/6\pi\eta r$) for D into Equation 3.10 J_z after setting to zero.

$$\frac{2g(\rho_p - \rho_m)r^2}{9\eta}C = D\frac{\Delta C}{\Delta z} \tag{3.14}$$

Equation 3.14 can then be integrated when C_1 and C_2 are set to the equilibrium concentrations at positions z_1 and z_2, respectively, to give:

$$ln\left(\frac{C_2}{C_1}\right) = \frac{4\pi g(\rho_p - \rho_m)r^3}{3k_BT}(z_2 - z_1) \tag{3.15}$$

The adjustable variables in the Equation 3.15 are T, r, and the ratio between ρ_m and ρ_p. At equilibrium, where the left side of the equation is equal to zero, T equals infinity, r equals zero, and/or ρ_p and ρ_m are equal.

Considerations of the three possible solutions, for example, T, r, and the ratio between ρ_p and ρ_m are as follows: (1) The temperature of the suspension cannot be logically raised to a high enough point that the suspension solution would continue to be at a liquid state. The Mason-Weaver simulation indicates that even at 373.15 K, the terminal sedimentation velocity of the particles is decreased only by 1%; (2) the mass of the particle can be reduced. There is only a 2-times decrease in the terminal sedimentation velocity of particles with only a 5-nm decrease in the particle radius from 30 nm; and (3)

the density of the particle can be reduced to more closely match the suspension solution density. This has the largest impact when the density of the particle is matched for example, to that of the polystyrene particle; the terminal sedimentation velocities decrease by two orders of magnitude.

Thus, reducing the particle size and decreasing the density of the particle are possible solutions to the reduction in sedimentation. However, the location of the plasmon resonance is important to the strength of the SERS signal. Our SERS-based immunoassay has been developed based on the optical properties of 60 nm AuNPs. A possible solution is to use polystyrene core gold nanoshells or other SERS active materials such as silver or aluminum, which also have lower densities.[37-39]

3.5 Conclusions

This work has demonstrated the importance of gravity-induced sedimentation on the movement of AuNPs (60 nm diameter) on their delivery to the capture substrates used in an immunoassay. Results also indicate that the quality of the analysis of the capture substrates is improved by elimination of sedimentation, and thus the transport of AuNPs to diffusion. Work is underway to develop approaches that will simplify the ability to apply the implications of these findings to our and other NP-based platforms.

3.6 References

(1) Novotny, L.; Hecht, B. *Principles of Nano-optics*; Cambridge University Press: Cambridge, 2012.

(2) Kelly, K. L.; Coronado, E.; Zhao, L. L.; Schatz, G. C. *J. Phys. Chem. B* **2003,** *107,* 668-677.

(3) Daniel, M.-C.; Astruc, D. *Chem. Rev.* **2004,** *104,* 293-346.

(4) Rogach, A. L.; Eychmüller, A.; Hickey, S. G.; Kershaw, S. V. *Small* **2007,** *3,* 536-557.

(5) Reiss, P.; Protiere, M.; Li, L. *Small* **2009,** *5,* 154-168.

(6) Jain, P. K.; Huang, X.; El-Sayed, I. H.; El-Sayed, M. A. *Acc. Chem. Res.* **2008,** *41,* 1578-1586.

(7) Huang, X.; El-Sayed, I. H.; Qian, W.; El-Sayed, M. A. *J. Am. Chem. Soc.* **2006,** *128,* 2115-2120.

(8) Loo, C.; Lowery, A.; Halas, N.; West, J.; Drezek, R. *Nano Lett.* **2005,** *5,* 709-711.

(9) Pankhurst, Q. A.; Connolly, J.; Jones, S.; Dobson, J. *J. Phys. D: Appl. Phys.* **2003,** *36,* R167.

(10) Hyeon, T. *Chem. Comm.* **2003,** 927-934.

(11) Lin, X.-M.; Samia, A. C. *J. Magn. Magn. Mater.* **2006,** *305,* 100-109.

(12) Elghanian, R.; Storhoff, J. J.; Mucic, R. C.; Letsinger, R. L.; Mirkin, C. A. *Science* **1997,** *277,* 1078-1081.

(13) De, M.; Rana, S.; Akpinar, H.; Miranda, O. R.; Arvizo, R. R.; Bunz, U. H.; Rotello, V. M. *Nat. Chem.* **2009,** *1,* 461-465.

(14) Park, J.-W.; Shumaker-Parry, J. S. *ACS Nano* **2015,** *9,* 1665-1682.

(15) Love, J. C.; Estroff, L. A.; Kriebel, J. K.; Nuzzo, R. G.; Whitesides, G. M. *Chem. Rev.* **2005,** *105,* 1103-1170.

(16) Vericat, C.; Vela, M.; Benitez, G.; Carro, P.; Salvarezza, R. *Chem. Soc. Rev.* **2010,** *39,* 1805-1834.

(17) Grubisha, D. S.; Lipert, R. J.; Park, H.-Y.; Driskell, J.; Porter, M. D. *Anal. Chem.* **2003,** *75,* 5936-5943.

(18) Shafer-Peltier, K. E.; Haynes, C. L.; Glucksberg, M. R.; Van Duyne, R. P. *J. Am. Chem. Soc.* **2003,** *125,* 588-593.

(19) Orendorff, C. J.; Gole, A.; Sau, T. K.; Murphy, C. J. *Anal. Chem.* **2005,** *77,* 3261-3266.

(20) Millen, R. L.; Kawaguchi, T.; Granger, M. C.; Porter, M. D.; Tondra, M. *Anal. Chem.* **2005,** *77,* 6581-6587.

(21) Wang, S. X.; Li, G. *IEEE Trans. Magn.* **2008,** *44,* 1687-1702.

(22) Li, H.; Rothberg, L. *Proc. Natl. Acad. Sci. USA* **2004,** *101,* 14036-14039.

(23) Thanh, N. T. K.; Rosenzweig, Z. *Anal. Chem.* **2002,** *74,* 1624-1628.

(24) Jang, S. P.; Choi, S. U. *Appl. Phys. Lett.* **2004,** *84,* 4316-4318.

(25) Mason, M.; Weaver, W. *Phys. Rev.* **1924,** *23,* 412.

(26) Driskell, J. D.; Kwarta, K. M.; Lipert, R. J.; Porter, M. D.; Neill, J. D.; Ridpath, J. F. *Anal. Chem.* **2005,** *77,* 6147-6154.

(27) Axelsson, I. *J. Chromatogr. A* **1978,** *152,* 21-32.

(28) Chang, H.-C.; Wang, L.-C. *arXiv:1009.4322* **2010,** 1-4.

(29) Haiss, W.; Thanh, N. T.; Aveyard, J.; Fernig, D. G. *Anal. Chem.* **2007,** *79,* 4215-4221.

(30) Hunter, R. J. *Zeta Potential in Colloid Science: Principles and Applications*; Academic Press: Cambridge, 2013.

(31) Berne, B. J.; Pecora, R. *Dynamic Light Scattering: With Applications to Chemistry, Biology, and Physics*; John Wiley & Sons: New York, 2000.

(32) Gebauer, J.; Malissek, M.; Simon, S.; Knauer, S.; Maskos, M.; Stauber, R.; Peukert, W.; Treuel, L. *Langmuir* **2012,** *28,* 9673-9679.

(33) Park, H.-Y.; Driskell, J. D.; Kwarta, K. M.; Lipert, R. J.; Porter, M. D.; Schoen, C.; Neill, J. D.; Ridpath, J. F. *Ultrasensitive Immunoassays Based on Surface-enhanced Raman Scattering by Immunogold Labels*; Springer: Berlin, 2006; p 427-446.

(34) Modi, H.; Fuerstenau, D. *J. Phys. Chem. A* **1957,** *61,* 640-643.

(35) Reth, M. *Nat. Immunol.* **2013,** *14,* 765-767.

(36) Cho, E.; Zhang, Q.; Xia, Y. *Nat. Nanotechnol.* **2011,** *6,* 385-391.

(37) Yong, K.-T.; Sahoo, Y.; Swihart, M. T.; Prasad, P. N. *Colloids Surf.* **2006,** *290,* 89-105.

(38) Shi, W.; Sahoo, Y.; Swihart, M. T.; Prasad, P. *Langmuir* **2005,** *21,* 1610-1617.

(39) Chan, G. H.; Zhao, J.; Schatz, G. C.; Duyne, R. P. V. *J. Phys. Chem. C* **2008,** *112,* 13958-13963.

CHAPTER 4

THE DEVELOPMENT OF A TUBERCULOSIS DIAGNOSTIC TOOL USING SURFACE-ENHANCED RAMAN SCATTERING

4.1 Introduction

Despite modern advances in diagnostics and treatment, tuberculosis (TB) persists as the world's second deadliest infectious disease from a single infectious agent.[1, 2] TB ranks second in mortality only to human immunodeficiency virus (HIV)/acquired immune deficiency syndrome (AIDS). TB disease caused by the growth of *Mycobacterium tuberculosis* (*M. tuberculosis*) bacillus. In well-developed countries, TB is normally considered to be a disease of the past, and, as a bacterial infection, is a curable and preventable disease. However, in resource-limited regions of the world, primarily in Asia and Africa, a high incidence of TB infection persists due to outdated diagnostic methods, coinfection with immune suppressing diseases, and limited treatment options. Diagnosis in these high-risk regions depends primarily on sputum smear microscopy and serological tests.[3] The World Health Organization (WHO), however, has issued a warning that these serological tests be avoided due to their inherent inaccuracy, due to the prevalence of immunocompromised patients. The poor performance of these tests pose health risks due

to delays in treatment from a false-negative result or unnecessary/improper treatment from a false-positive result. The ability to reliably test for TB in regions that have limited resources is therefore a crucial step in the efforts to reduce the worldwide mortality rate from TB.[4] This chapter focuses on the development of a new, sensitive, cost-effective, and reliable diagnostic test for TB infection, which has the potential, when paired with early treatment, to reduce the loss of life due to this preventable and curable disease.

The difficulty associated with the accurate diagnosis of *M. tuberculosis* infection in resource-limited regions results from complications associated with the disease and/or available resources. There are three primarily factors: (1) TB is associated with a latent phase of infection in which the immune system of an individual suppresses the bacterial growth. Under normal circumstances, latent TB infection has a 5-10% risk of turning into active infection. However, the risk significantly increases for individuals with a compromised immune system, such as that due to HIV/AIDS;[5] (2) coinfection with HIV/AIDS can also impair the accuracy of detection methods by reducing levels of immunomarkers (e.g., antibodies), changing the normal progression of the disease, and/or altering the expected distribution of the bacterial load within the body; and (3) resource-limited regions with a high TB burden have a serious need for new diagnostic methods that can be used in area where it is needed the most. However, it is also imperative that these testing positive have ready access to antiTB treatment regimes.

Currently, a wide variety of detection methods for TB infection are available that test for one or more of the following: the bacteria, an antigen produced by the bacteria, DNA/RNA sequence specific to the bacteria, or antibodies produced in response to bacterial exposure.[6] The most accurate and reliable method for diagnosing TB infection is

bacterial culture.[7] Most types of biological patient samples (e.g., sputum) can be cultured, can be used to track the response to treatment. However, specialized facilities and incubation times of several weeks are essential to culture and grow *M. tuberculosis*, both of which present significant problems for resource-strapped regions that cannot tolerate the significant financial burden or time delay for diagnosis with this type of testing.

Due to the time and cost limitations associated with bacterial culture, less accurate, but lower cost and more rapid tests for TB detection are often used, including a skin test and sputum smear microscopy.[8] In regions with low TB incidence and lower HIV occurrence, the skin test is the most common first step in diagnosis.[9] The skin test uses an intradermal injection on the forearm of a patient of purified protein derivative (PPD) from *M. tuberculosis*.[10] If antibodies for TB are present, a distinct red induration will appear at the injection sight. This test, however, can only determine if an individual has been exposed to *M. tuberculosis*, but not necessarily the existence of active infection. The test can also be inaccurate if the patient has a compromised immune system and is unable to a produce sufficient number of TB antibodies for a positive reaction to the PPD. These screening shortcomings are particularly in areas undesirable with a high TB incidence and large numbers of the population with undiagnosed HIV.[7]

In resource-limited regions of the world with a high likelihood of exposure to TB and HIV/AIDS infection, sputum smear microscopy is the primary method for detection. Microscopy is a technique developed over 100 years ago as a rudimentary way of detecting and identifying microorganisms.[11-13] A sputum sample, which should contain a large amount of the *M. tuberculosis* bacilli if the patient has pulmonary TB infection, can be used to determine the presence of the bacteria. The bacteria, when present at a high load

(~5,000 to 10,000 bacilli mL^{-1}),[14] are identified by using an acid fast stain to bacteria in the genus *Mycobacterium*, which can, in turn, be visually identified with microscopy. This method is low cost, fast, and widely available. However, sputum smear microscopy requires the presence of a detectable level of bacterial load in the lungs. Smear-negative (i.e., false negative) results are high among many classes of TB-infected patients including children, HIV positive patients, and extrapulmonary patients, due to deviations from the normal progression of the disease.[15]

The need for more reliable and accessible detection methods has played a major role in the development of today's methods for TB diagnosis, including detection by enzyme-linked immunosorbent assays (ELISA),[16, 17] radiometry,[18] and the polymerase chain reaction (PCR).[19] While these methods can be sensitive with antigen detection at 1 ng mL^{-1}, all require advanced facilities and highly trained personnel, which makes them methods impractical for resource-limited regions.

This paper describes a TB immunoassay based on surface-enhanced Raman scattering (SERS) as the readout mechanism. Using SERS, a Raman signal can be typically amplified by a factor of 10^4-10^6;[20] with values as high as 10^{14}reported in a few cases.[21] SERS enhances the Raman signal by means of the inherent plasmonic properties of substrates consisting of asperities of nanometrically-sized coinage metals on a surface.[22] A SERS-active substrate generates localized surface plasmon resonance (LSPR) when an excitation source matches the natural frequency of the conduction electrons of the material,[23] which magnifies the electric field near the surface of the asperity, and therefore effective Raman cross section of a Raman-active molecule adsorbed on the SERS-active substrate. The signal enhancement is a distinct advantage of SERS detection, but other

attributes include using a red-shifted excitation source, which reduces the native fluorescence, and low susceptibility to photobleaching, which reduces signal degradation.

The advantages of SERS detection have led to the development of a SERS-based immunoassay that has proven to be a sensitive and robust system for bioanalytical analysis.[24-28] A variety of different biological agents have been detected with this platform, including proteins, viruses, and microorganisms. The SERS-based immunoassay consists of an atomically smooth gold substrate, biorecognition elements, and gold nanoparticles (AuNPs) labeled with a Raman reporter molecule (RRM). These components are then carefully constructed to create a sandwich immunoassay which is paired with SERS as the readout method.

The SERS-based immunoassay is carried out by first immobilizing a capture antibody on a gold substrate, which is then exposed to a solution of the TB-containing sample. This step binds a TB marker to the capture antibody on the surface. The immobilized antigen is then selectively labeled with an extrinsic Raman label (ERL), which consists of gold NPs modified with a RRM and a tracer antibody. Finally, the tagged antigen is indirectly detected by the SERS signal of the ERL.

The bulk of this paper discusses the development of a SERS immunoassay for the detection of lipoarabinomannan (LAM). LAM is a 14-17 kDa lipopolysaccharide and major component of the cell wall of *Mycobacteria* that is continually shed by the organism. As a result, LAM is a unique and an excellent candidate to serve as an antigenic marker for TB infection. PILAM, which is LAM terminated by phosphor-*myo*-inositol and produced by the relatively fast growth of *M smegmatis*. The nonvirulent nature of this strain of *Mycobacterium* makes it an ideal surrogate for method development.[29, 30]

Two other antigenic markers, α-crystalline protein (ACR) and Rv0363c, are also used herein for the development of a multiplexed assay. ACR is a dominate, 16 kDa heat shock protein produced by *M. tuberculosis* that is possible a marker for latent infection,[31] and Rv0363c is a 36.5 kDa gene that encodes for the glycolysis enzyme fructose-bisphosphate aldolase.[32] The combination of the three markers can be used in a multiplexed platform for the detection of TB. The benefits of using multiple markers have four primary advantages. First, multiplexed detection uses a smaller amount of the patient sample for testing.[33] Second, test efficiency increases due to faster turn-around times associated with parallel analysis. Third, the increased number of markers reduces false positive and false negative results. And fourth, tracking multiple markers is more informative for guiding treatment. However, a marker is only a viable candidate if it is present in patient samples at levels measurable by the detection method.

The research presented in this paper will describe the development of the SERS-based sandwich immunoassay for the detection of TB infection. The findings indicate low limits of detection via SERS detection with antigenic TB markers spiked into biologically relevant media. In order to determine the most effective method for TB diagnosis the results from three types of biological media, multiplexed detection of three antigenic TB markers in serum, and pretreated serum for the detection of PILAM were compared. The performance of the SERS assay for the detection of PILAM in pretreated serum was determined to provide the most useful diagnostic information based on the limit of detection (LoD) and probability of antigenic markers present in the biological matrix.

4.2 Experimental

4.2.1 Reagents and Materials

Dithiobis(succinimidyl propionate) (DSP, > 95%), modified Dulbecco's phosphate buffered saline packs (pH 7.4), borate buffer (BB) packs (pH 8.5), magnesium chloride hexahydrate (ACS grade), potassium chloride (ACS grade), potassium carbonate, SuperBlock and StartingBlock were obtained from Fisher Scientific. Acetonitrile (ACN, Spectroscopy grade), Tween 20, sodium chloride, 70% perchloric acid, and bovine serum albumin (BSA) were purchased from Sigma-Aldrich. Urisub, a synthetic urine matrix, was received from CST Technologies; poly(dimethyl siloxane) (PDMS) from SlyGuard; Epoxy 377 from EPO-TEK; calcium chloride from EM Science; monobasic sodium phosphate (ACS grade) from BDH; dibasic sodium phosphate (ACS grade) from JT Baker; 200-proof ethanol (ACS grade) from Pharmco-AAPER; octadecanethiol (ODT) from Fluka; AuNPs (60-nm ~1×10^{10} particles mL^{-1}) from NanoPartz; and LAM-specific TB antibodies and purified PILAM antigen from B.E.I. resources. ACR and α-ACR (BIIIc4B11B6C5C7), were obtained from Frederick Quinn (Georgia State University, GA) and recombinant protein Rv0363c and rabbit α-Rv0363c from Delphi Chatterjee (Colorado State University, CO). An allergen powder containing galactomannan purchased from Greer Laboratories (Lenoir, NC), heat-killed Escherichia coli O157:H7 was provided by Nancy Cornick (Department of Veterinary Microbiology and Preventive Medicine, Iowa State University, Ames), and heat-killed *Mycobacterium avium* subsp. *paratuberculosis* (MAP) was obtained from BD Diagnostic Systems (Hunt Valley, MD). All of these reagents were used without further purification.

The synthesis of the Raman reporter molecule 5-5'-dithiobis(succinimidyl-2-

nitrobenzoate) (DSNB)[28] and that of citrate-capped 30-nm NPs[34] followed previously described procedures.

4.2.2 Preparation of Extrinsic Raman Labels (ERLs)

For additional information on the background and history of the procedures used for ERL and capture substrate preparation, please refer to previous publications.[26-28] These procedures, shown in Scheme 4.1, were subsequently modified to increase the sensitivity of the measurement. Briefly, ERLs were prepared by first concentrating the 30-nm diameter AuNP suspension as follows. The NPs (4 mL, 1.3×10^{11} particles mL^{-1} as received) were centrifuged at 2,000*g* for 20 min and the clear supernatant was carefully decanted from the sedimented NPs. The NPs were then resuspended in 1 mL of 2 mM BB to yield a final concentration of 5.2×10^{11} particles mL^{-1}. The concentration of the NP suspension was verified using the UV-Vis method developed by Haiss and collaborators.[35] Next, the NPs were incubated with 10 μL of 1.0 mM DSNB in acetonitrile at room temperature and agitated on a horizontal rotator at 2 Hz for 1.5 h.

DSNB was designed to serve three primary functions: (1) disulfide group forms a chemisorbed monolayer on the NP surface via thiolate formation, (2) the succinimidyl groups for amide linkage of biorecognition elements, and (3) the NO_2 groups produce an intrinsically strong and unique signal as a RRM. After DSNB incubating 5 μg of antiLAM monoclonal antibodies (mAb) were added to the suspension and the primary amines on the antibody were allowed to react with the succinimidyl group on DSNB for 1.5 h at room temperature on the rotator, allowing the tracer antibodies to react with the modified NP surface. A 100-μL aliquot of 10% BSA solution, dissolved in 2 mM BB, was subsequently

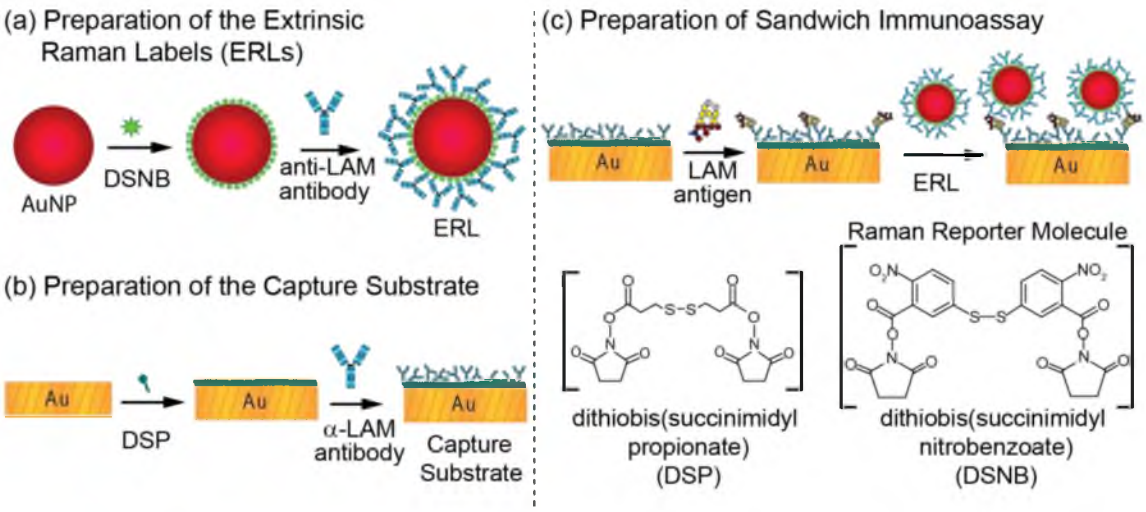

Scheme 4.1. SERS-based Sandwich Immunoassay

added to the NPs to block nonspecific adsorption sites and to stabilize the colloidal suspension. The resulting supernatant was mixed for 1.5 h on the rotator at room temperature, which completed the preparation of the ERLs. Residual reactants were then removed in a three step process. For this, the ERLs were pelleted in a centrifuge tube 2,000*g* for 20 min, the clear supernatant was carefully removed, and the particles were resuspended with 1.0 mL of 1% BSA in 2 mM BB. The centrifugation and resuspension steps were repeated two additional times, with the final resuspension conducted in 0.5 mL of the 1% BSA in 2 mM BB. Finally, the ionic strength of the ERL suspension was adjusted by adding an aqueous NaCl solution to the ERLs to achieve an NaCl concentration of 150 mM. Upon the completion of these processing steps, the ERL concentration was ~4.0×10^{11} particles mL^{-1}.

4.2.3 Preparation of Capture Substrate

The capture substrates were prepared using 1 × 1 cm template stripped gold (TSG).[36] The TSG was modified via microprinting with a PDMS stamp dipped in a 2 mM ethanoic solution of ODT and thoroughly dried before being pressed into conformal contact on the clean TSG surface. The stamp creates an unmodified, 2-mm address in the center of the substrate that is surrounded by a hydrophobic boundary; the address was then modified with an ethanolic DSP solution for 1 h, rinsed with ethanol, and thoroughly dried with N_2(g).

A 2.5-μg mL^{-1} solution of antiLAM mAb 906.7 was prepared by diluting a freshly thawed aliquot of the mAb in 10 mM phosphate-buffered saline containing 0.1% Tween 20 pH 7.4 (PBST). A 20-μL drop of the α-LAM solution was then applied to the DSP-

modified surface and allowed to react for 1 h at room temperature in a humidity-controlled environment (97% relative humidity). ACR and Rv0363c are incubated with either a 20 μL droplet of 100 μg mL^{-1} α-ACR or α-Rv0363c, each on separate TSG substrates. These substrates were rinsed three times by immersion in 2 mL of PBST in a 24-well microplate, removing the rinse buffer with an aspirator between rinses. Next, the substrate was exposed for 1h to 20 μL of StartingBlock, a commercially available blocking agent, for 1 h, followed by rinsing three times with 2 mL of PBST using the just described procedure.

4.2.4 Antigen Capture and Labeling

The capture substrates were then exposed to 20 μL of PILAM spiked into a buffered solution or one of three sample matrices: PBST, Urisub, simulated CSF, or human serum. Each of these spiked samples were prepared at an antigen level of at 1.0 mg mL^{-1} and then serially diluted each matrix to different concentrations. Antigen capture incubated the capture substrate in an inverted position for 1.0 h in a humidity chamber. The substrates were rinsed three times with 2 mL of 2 mM borate buffer containing 150 mM NaCl and 0.1% Tween 20 (BBT). A 20-μL aliquot of the freshly prepared ERLs was then pipetted onto each substrate, and incubated in an inverted position for 16 h at room temperature in a humidity chamber. The samples were then rinsed three times with 2 mL of BBT, followed by three times with deionized H_2O. The samples were dried under ambient conditions and analyzed by SERS.

4.2.5 Biological Samples and Serum Pretreatment

Urine, CSF, and serum were used as biologically relevant sample matrices to assess the utility of the SERS diagnostic platform for the detection of PILAM. Relative to serum, urine, and CSF are similar simple biological samples that consist primarily of electrolytes and a few proteins. Artificial urine and CSF were used to ensure a consistency of these two matrices. Synthetic urine was acquired from a commercial source, whereas artificial CSF was prepared in the laboratory. The artificial CSF solution contained 148 mM sodium chloride, 3 mM potassium chloride, 1.4 mM calcium chloride, 0.8 mM magnesium chloride, 0.8 mM sodium phosphate dibasic, and 0.2 mM sodium phosphate (monobasic).[37] The antigen-spiked sample for each matrix was then tested without further pretreatment.

Mixed antigen solutions for multiplexed detection were prepared by spiking antigen solution into serum and subsequent exposure to a capture substrate. Studies performed in serum did not provide LoDs at levels low enough (1 ng mL^{-1})[8] to meet our preliminary detection goals.

Investigation of the markers lead to the discovery that PILAM complexes with proteins and the structural stability of the molecule. Denaturing agents then allow for the removal of interfering proteins in the serum while leaving the PILAM structurally intact. PILAM spiked into serum was treated with two different methods to compare the benefits of protein removal methods

The first serum treatment was performed by heating a 500-µL serum sample for 30 min at 95 ^{0}C, followed by centrifugation at 12,000*g* for 30 min. The resulting clear supernatant was then used for analysis. Raman spectra were collected with a 3-s integration time using Raman instrumentation described herein. The second method involved

perchloric acid pretreatment and neutralization following this simple five-step procedure. To start (Step 1), 2.0 μL of $HClO_4$ (70%) was added to 100.0 μL of each calibration/patient serum sample in a small centrifuge tube. The sample was immediately vortexed for 10 s which brought the pH to ~2 and formed a milky suspension. The sample was then centrifuged at 13,000*g* for 5 min (Step 2), and 75 μL of the resulting supernatant were transferred to a second small centrifuge tube (Step 3). The sample was then neutralized to pH 7.5 with 6.0 μL of an aqueous solution of K_2CO_3 (2.0 mM) (Step 4). The samples were then cooled to 4^0C for 30 min and subsequently allowed to warm to room temperature (~20 min) before being pipetted (20 μL) onto the capture substrate (Step 5). Perchloric acid treated serum samples were analyzed on a SERS immunoassay using 60-nm AuNPs for the base of the ERL.

4.2.6 Raman Instrumentation

The Raman instrument used for data collection is a modified NanoRaman from Concurrent Analytical (Loveland, CO). The instrumentation has three primary components: laser excitation source, spectrograph, and fiber optic probe. The light source is a 22-mW, 632.8-nm HeNe laser. The spectrograph consists of an f/2.0 Czerny Turner imaging spectrometer with 6-8 cm^{-1} resolution and a Kodak 0401E charged coupled device (CCD) thermoelectrically cooled to 0 °C. The instrument was modified by upgrading the fiber optics with SMA connectors and stainless steel protection sheaths and micropositioning alignment collimators from Thor labs.

4.3 Results and Discussion

4.3.1 Antibody Screening

The development of the assay initially involved screening of a number of candidate antibodies specific for their ability to capture the *M. tuberculosis* antigen LAM after immobilization on TSG substrates. This test panel was selected by Professor Delphi Chatterjee and coworkers at Colorado State University (CSU) based on Western Blot analysis. The antibodies selected for screening included those from series 900 and subclones of line 906: 906.1, 906.7, and 906.41.[38, 39] All 906 line antibodies bind to an epitope region specific to the mycobacterium biomarker LAM was primed with whole *Mycobacterium lepae* and given several boosters of crude LAM. The antibodies were used to produce both the capture substrate (produced with capture antibodies) and the ERLs (produced with tracer antibodies). Assessment of the performance of purified monoclonal antibodies was conducted by analyzing SERS data from a 5-μg mL^{-1} sample of PILAM purified from *M smegmatis* spiked in PBST and a blank sample consisting of only PBST. The assay was carried out according to the procedure shown in Schematic 4.1. In short, the capture substrate was prepared with a 2.5 μg mL^{-1} solution of capture antibody, which was first blocked with StartingBlock and then exposed to the sample. The bound antigen from the sample was then labeled with ERLs which consisted of 30-nm gold NPs modified with DSNB and the tracer antibody. Each possible combination of capture and tracer antibodies was analyzed (Figure 4.1) to determine which combination would be most effective in the SERS assay platform, based on sensitivity and LoD.

The DSNB spectral features are shown in Figure 4.1a for the assay performed with the 906.7 antibody as both the capture and tracer antibodies at a PILAM concentration of

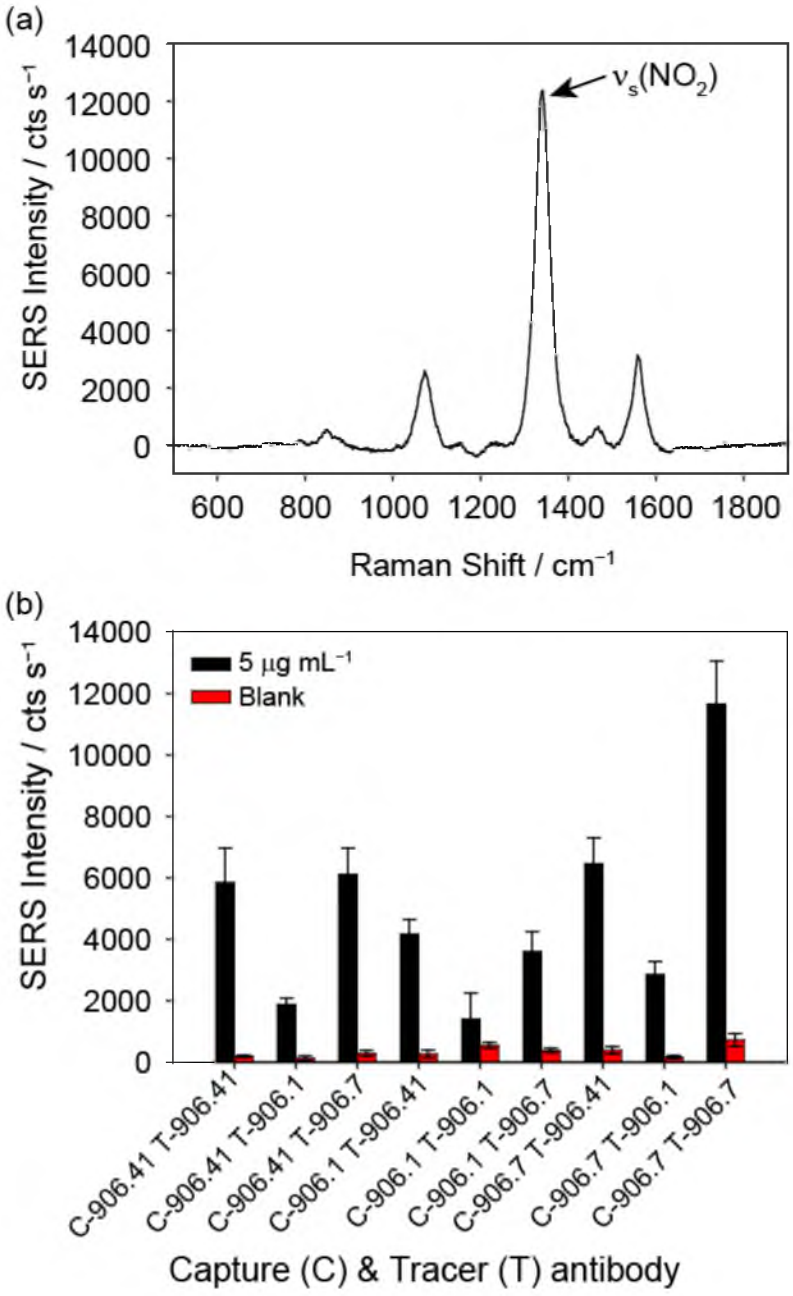

Figure 4.1. A representative spectrum for the SERS sandwich immunoassay and results from an antibody screening studies for detection of PILAM. (a) Shows a SERS spectrum indicating spectral features assigned to the molecule DSNB. The spectrum corresponds to data collected for the 906.7 antibody as the capture and tracer antibodies at 5 µg mL^{-1} of LAM. (b) SERS intensities for immunoassays screening a combination of 906 antibody series 906.1, 906.7, and 906.41 reacted with 5 µg mL^{-1} of PILAM in PBST and blank PBST samples. The data used for screening studies were collected by measuring the peak height from the $\nu_s(NO_2)$ stretch at 1336 cm^{-1} in counts per second (cts s^{-1}).

5 μg mL^{-1}. Band assignments for the spectra have been described in detail previously but will be briefly reviewed here.[25, 28] The strongest spectral feature is produced by the symmetric nitro stretch ($\nu_s(NO_2)$) at 1336 cm^{-1}. The other bands correspond to the scissoring mode for the nitro group at 851 cm^{-1} and two aromatic ring modes at 1062 and 1554 cm^{-1} shown in Figure 4.1a.[25] Note that the Raman spectrum for the immunoassay is composed only of spectral features that can be attributed to DSNB, there are no contributing peaks from the biological elements used in the immunoassay platform.

The peak height produced by the strongest DSNB feature [$\nu_s(NO_2)$ centered at 1336 cm^{-1}] in the sample spectrum is used to quantitate the concentration of antigen in the sample. The intensity of the symmetric nitro stretch for each of the data points was determined by collecting data from five locations on each of the five assay substrates; the results are given as the average for each set of data. Analysis of the data focused on identifying which combination of antibodies produced the highest SERS signal for the 5-μg mL^{-1} sample and the lowest relative signal for the blank sample.

The results shown in Figure 4.1b clearly demonstrate that the heterogeneous assay using 906.7 antibody as both the capture and tracer antibody gives the highest SERS intensity at 1336 cm^{-1}. To determine more clearly which combination of antibodies would be the most effective, the projected limits of detection (projected LoDs) were calculated for all combinations and summarized in Table 4.1. The projected LoD is defined as its blank signal plus three times the standard deviation. The analysis shows that the lowest projected LoD was obtained when using the 906.41 antibody as both the capture and tracer antibodies. The highest signal strength was observed for 906.7 as the capture and tracer antibodies 906.7 used as the capture and tracer antibodies also represents the second lowest

Table 4.1. SERS Immunoassay Compatibility Testing for Capture and Tracer Antibodies

Antibodies	Raman Intensity [LAM], 5 μg mL^{-1}	Blank	projected LoD, ng mL^{-1}
C-906.41 T-906.41*	5855 ± 1118	193 ± 40	106
C-906.41 T-906.1	1892 ± 190	135 ± 79	677
C-906.41 T-906.7	6117 ± 857	290 ± 96	246
C-906.1 T-906.41	4183 ± 486	270 ± 126	481
C-906.1 T-906.1	1407 ± 847	550 ± 98	1718
C-906.1 T-906.7	3606 ± 639	385 ± 72	337
C-906.7 T-906.41	6471 ± 831	393 ± 120	296
C-906.7 T-906.1	2858 ± 422	166 ± 53	294
C-906.7 T-906.7**	11664 ± 1392	726 ± 205	281

C – Capture antibody immobilized on the Au capture substrate
T – Tracer antibody immobilized on the extrinsic Raman label
* Shows the lowest projected LoD
**Shows the highest signal and second lowest LoD

projected LoD. Based on the large signal for the 5 μg mL^{-1} and on the anticipation of reduced nonspecific adsorption upon further development of the system, 906.7 antibodies were selected for use as both the capture and tracer antibodies for the remainder of the studies.

4.3.2 PILAM Spiked into PBST

Development of the SERS immunoassay for the detection of PILAM began by using PBST as a simple sample matrix that was spiked with PILAM concentrations ranging from 1.0×10^2 pg mL^{-1} to 2.5 ng mL^{-1}. The capture substrate was prepared using 906.7 antiLAM antibodies. The spiked samples were exposed to the capture substrate for 1 h in an inverted position. The substrates were then rinsed and exposed to the ERLs modified with the 906.7 antiLAM antibodies for 16 h in an inverted position. The resulting SERS spectra were collected from two sets of sample substrates by measuring five locations on each assay substrate and a 3-s read time. These data were analyzed using the peak height of the strongest Raman band produced by the symmetric nitro stretch at 1336 cm^{-1} after baseline correction (Figure 4.2). SERS data show an increase in the signal at 1336 cm^{-1} with increasing concentrations of PILAM. The concentration-dependent increase in the dose-response curve follows a linear dependence for PILAM over the tested range of PILAM concentrations. The LoD is indicated on the graph by the red dashed line, which is estimated in PBST to be 76 pg mL^{-1} or 4.5 pM.

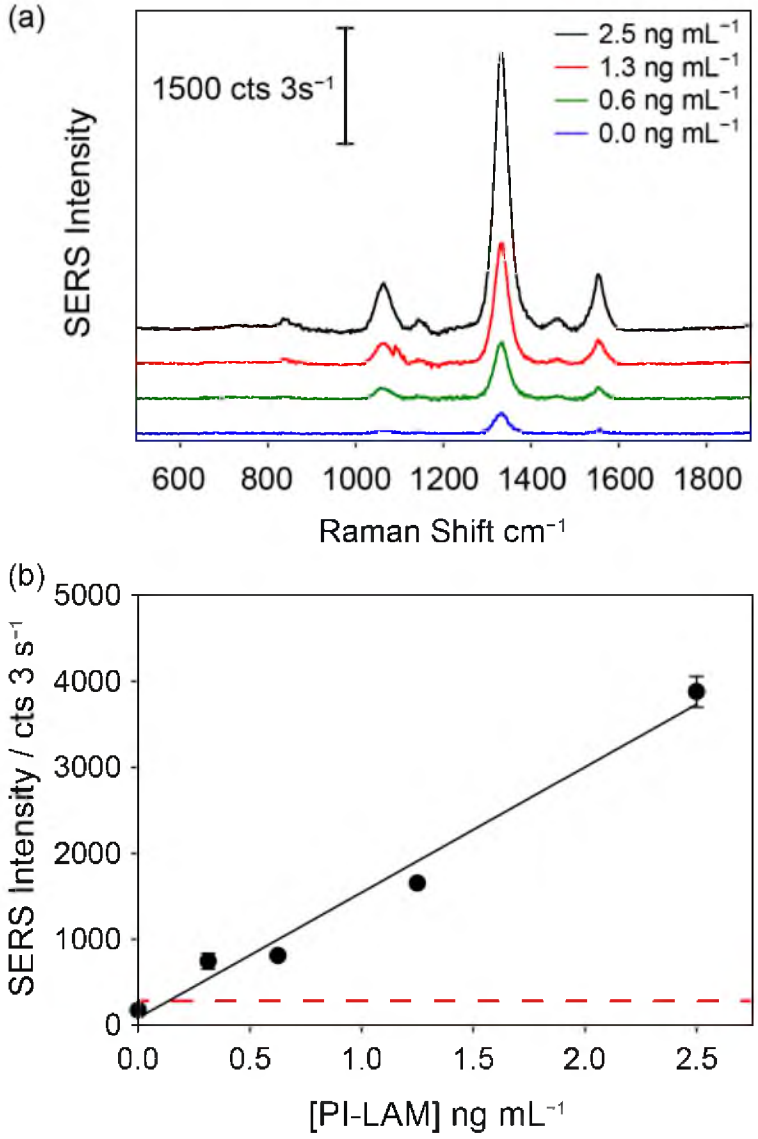

Figure 4.2. Spectra and calibration curve for PBST spiked with LAM using the 906.7 antibody as both the capture and tracer antibody. (a) Raman spectra for SERS-based immunoassay for PBST spiked with LAM. (b) Corresponding calibration curve with analysis of peak height at 1336 cm^{-1} for SERS-based immunoassay for PBST spiked with LAM with a 3 s integration time. The solid line represents the linear least-squares regression of the data with a corresponding fit of $y = 1458x + 85$ ($R^2 = 0.98$). The red dashed line represents the LoD determined as the blank signal plus three times the standard deviation, which was calculated to be 76 pg mL^{-1} or 4.8 pM.

4.3.3 PILAM Spiked in Biologically Relevant Samples

Development of a reliable and reproducible assay for TB requires that the detection platform can accurately establish whether bacteria are present in a host. The sample analyzed is therefore collected from the host, which is a more complex sample matrix. Past work has shown that LAM can be present in the urine, CSF, and serum as a result of the bacteria sloughing off the lipopolysaccharide of *M. tuberculosis*.[40-42] However, it is still uncertain as to the levels expected to be present in these samples. There are also complications in dealing with components that can interfere with the performance of the assay in the biological samples. Electrolytes, proteins, antibodies, antigens, hormones, and possible exogenous substances (e.g., drugs and microorganisms) can be present in the patient samples and can influence the performance of the assay. To determine the practicality of TB detection in urine, CSF, and serum samples, PILAM was spiked into Urisub, a synthetic urine, an artificial CSF solution, and TB-negative human serum.

Serial dilutions of the different solution matrices from 0 to 5 ng mL^{-1} were prepared for use in the SERS immunoassays. These results are shown in Figure 4.3. The results indicate that the Urisub and artificial CSF have comparable performance in the SERS assay than that in PBST with LoD that are below 1 ng mL^{-1}. It is important to note that Urisub and artificial CSF are protein-free surrogates were used in substitution of true biological samples. The use of true biological samples may cause signal depletion that is expressed in the serum samples. However, the results for the assay in serum indicated no detectable signal for PILAM at the given concentrations. SERS signal is observed for PILAM in serum at higher concentrations and is discussed later in this chapter. Data analysis was performed as previously described. The LoD was determined by calculating the blank signal plus three times the standard deviation and determining the intercept with the

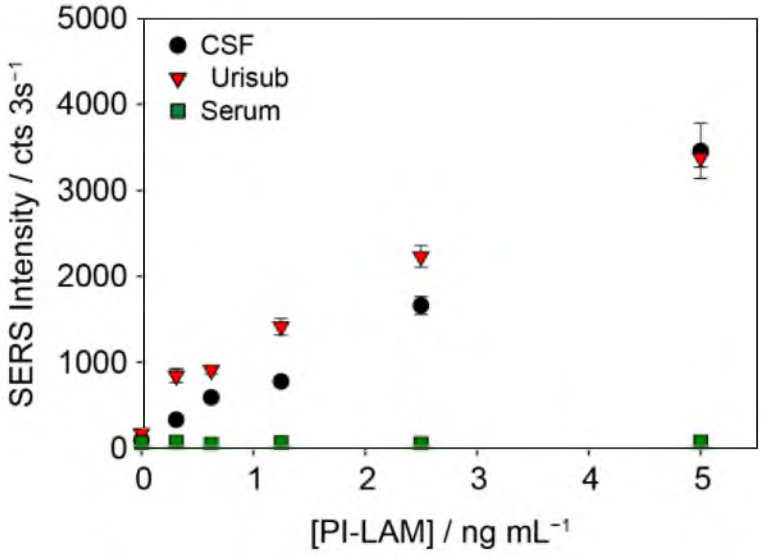

Figure 4.3. Dose response curves for SERS-based immunoassay with CSF, Urisub, and serum spiked with LAM. The linear least-squared regression for the different sample matrices are as follows: $y = 702x + 175$ ($R^2 = 0.91$) for CSF, $y = 660x + 95$ ($R^2 = 0.99$) for Urisub, and no linear range for serum, with limits of detection at 100 pg mL^{-1} for CSF and Urisub. Average and standard deviation of the displayed measurements come from two substrates measured at five different locations.

corresponding linear calibration. The analysis shows that the urine and CSF data exhibit a strong correlation to results produced for PILAM spiked in PBST. The urine and CSF samples have a slightly reduced sensitivity but have minimal sample variability. The LoDs for the untreated artificial urine and CSF were both determined to be 100 pg mL^{-1} or 5.9 pM in comparison to the LoD for PBST, which is calculated on the same order of magnitude as 76 pg mL^{-1} or 4.5 pM. The analysis of the serum samples shows a complete loss of detectable signal at the given concentrations but does start to be detectable at higher concentrations (data not shown). The reduction in the signal is attributed to potential complex formation with the serum components, passivation of the capture substrate due to the high concentrations of proteins in solution, and/or increased solution viscosity reducing diffusion.

4.3.4 Multiplexed Detection of Three Antigenic TB Markers in Serum

Improvements in diagnostics in biological samples can also be achieved by increasing the number of biomarkers that are measured in parallel. SERS-based analysis for ACR and Rv0363c were performed in a similar fashion as the experiments previously outlined for PILAM detection. To test the viability of a multiplexed SERS-based detection platform, the assay was run with spatially separated capture substrates exposed to a mixed antigen solution and an ERL suspension specific for a single antigen. Due to the speed of Raman readout, spatially separated substrates can be analyzed within a few seconds.

Results for the multiplexed detection for the TB markers PILAM, ACR, and Rv0363c are shown in Figure 4.4. The results indicate that there is minimal cross reactivity

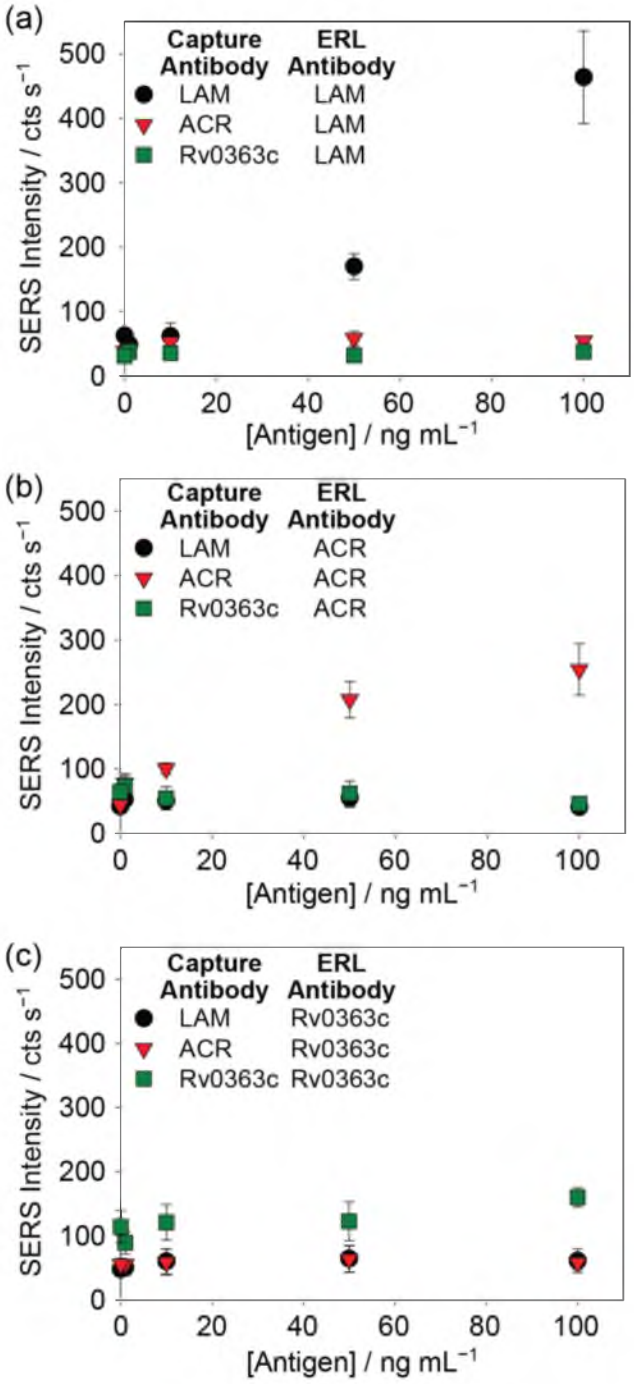

Figure 4.4. SERS calibration curves for mixed antigen solutions spiked into serum. (a) LAM ERLs selectively binding only the LAM capture substrate. (b) ACR ERLs selectively binding to the ACR capture substrate. (c) Rv0363c ERLs showing minimal selective binding to the Rv0363c capture substrate. Each data point is the average and standard deviation of two substrates analyzed at five separate locations each.

between the different antigenic markers. This is indicated by the limited amount of SERS signal for noncorresponding capture substrates and ERLs immunoassays. In Figure 4.4a the black circles correspond to the match between the LAM capture substrate and LAM ERLs. The data for the detection of PILAM show an increase in SERS signal with increased antigen concentration while the capture substrates for ACR and Rv0363c indicate no detectable signal. A similar trend in the data is observed for ACR ERLs with the quantifiable detection of ACR and minimal cross reactivity with the other antigens. Rv0363c ERLs shows limited sensitivity to Rv0363c spiked in serum but are detectable above the background at 100 ng mL^{-1}. Results for the multiplex detection are indicated as limit of quantification (LoQ) due to the decreased linear range in the data. The LoQ is defined as the concentration with the smallest detectable signal that is above the black and all of the noncorresponding substrates at all concentrations. From this definition, the LoQ for LAM is 50 ng mL^{-1} (3.6 nM), ACR is 10 ng mL^{-1} (0.6 nM), and Rv0363c is 100 ng mL^{-1} (2.7 nM). While these are reasonably low LoQs, a goal of 1 ng mL^{-1} LoD is the goal for prompting further development of the assay.

4.3.5 Pretreatment of Serum Samples Spiked with PILAM

Of the three antigenic markers, LAM is unique as a lipopolysaccharide instead of a protein. The structure is therefore free of secondary and tertiary protein components that are held together with hydrogen and electrostatic bonds. These types of bonds are more susceptible to cleavage due to exposure to chemicals and/or a harsh environment,[43] which can cause denaturation and agglutination of proteins. The covalent bonds that hold together the structure and shape of LAM allow the molecule to be more resistant to chemical and

heat treatment. Exposure to denaturing agents causes agglutination of serum proteins and inactivation of the bacteria without damaging the structure or epitope regions on PILAM. Centrifugation of the treated sample allows for extraction of a small volume of a clear solution than can be used in the SERS immunoassay.

The heat and perchloric acid treatment of the serum samples is a process that takes less than one hour, and has been described in detail in the experimental section. The remaining clear supernatant from the serum samples containing PILAM was placed on separate capture substrates and subsequently exposed to an ERL suspension. After a final rinse and drying step of the immunoassay, the fully prepared samples were analyzed. Data analysis was performed in the same manner as previously described by quantitatively measuring the relative signal strengths of the Raman spectra at 1336 cm^{-1} (Figure 4.5). The LoD was determined by calculating the blank signal plus three times the standard deviation of the signal. The LoD for the heat-treated serum was determined to be 150 pg mL^{-1} or 8.8 pM; the LoD of and perchloric acid treatment was calculated as 10 pg mL^{-1} or 1.0 pM. These results are comparable to results of the buffered PILAM. The heat-treated samples have a lower analytical sensitivity and the perchloric acid treated samples have a higher analytical sensitivity. However, both methods indicate dramatic and significant improvements in the LoD from the untreated serum, which displays no detectable signal in the same concentration range. The progression in the SERS immunoassay results for PILAM from raw serum to treated serum indicates the importance of serum pretreatment in the detection of the antigenic marker PILAM.

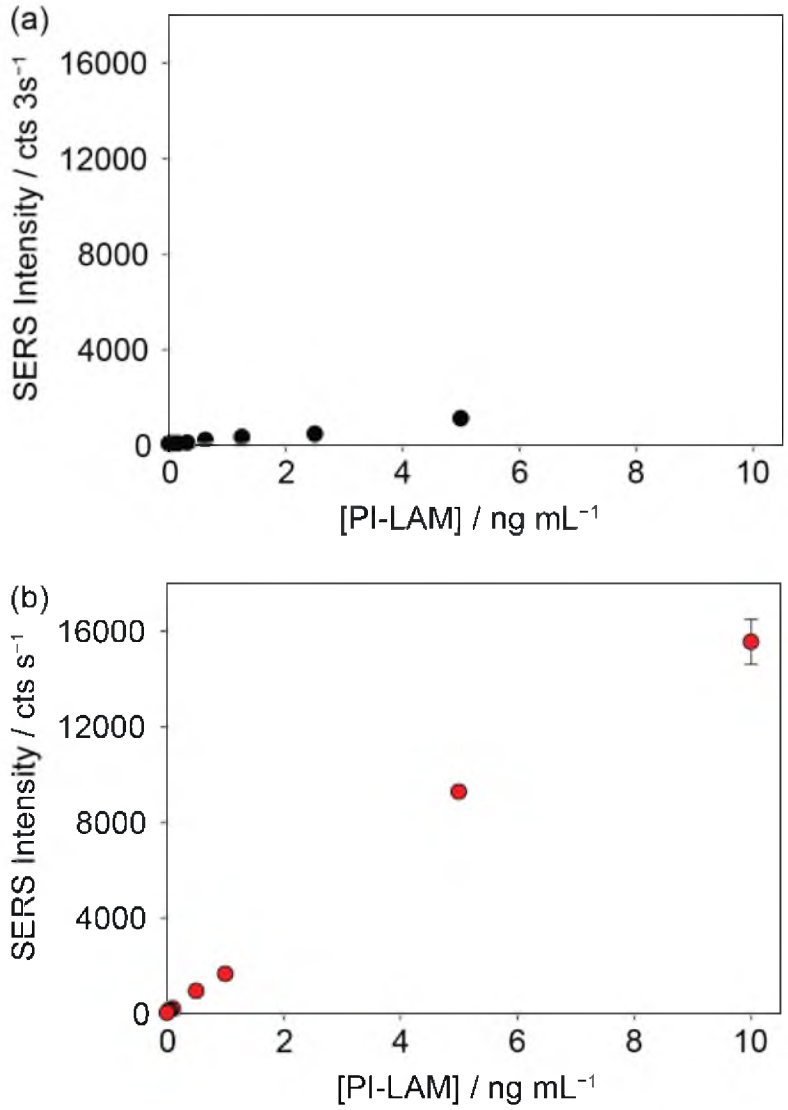

Figure 4.5. SERS dose-response curves for (a) heat and (b) perchloric acid treated serum containing PILAM. The linear least squares regression for the heat and perchloric acid treated serum samples displayed a linear response of $y = 203x + 69$ ($R^2 = 0.98$) with LoDs of 150 pg mL^{-1} (8.8 pM). The linear least squares regression for the heat and perchloric acid treated serum samples displayed a linear response of $y = 1665x + 30$ ($R^2 > 0.99$ with LoDs of 10 pg mL^{-1} (1.0 pM).

4.4 Conclusions

A new SERS-based detection method for TB has been developed. For this work the antigenic TB marker LAM was used as an indicator for TB infection. LAM is an ideal antigenic marker for TB infection due to the large amount of LAM that is produced by the bacteria that is sloughed off of the surface of *M. tuberculosis*. LAM produced by the Mycobacterium, *M. smegmatis*, was used in the studies due to the simplification of sample handling. The sandwich immunoassay developed for the detection of LAM displays a clinically significant LoD (below 1 ng/mL)[17] for PILAM in a variety of biologically relevant sample matrices using the SERS sandwich immunoassay. The analysis of LAM spiked into PBST, urine, and CSF all showed comparable results with a consistent and reliable LoD below 100 pg mL^{-1} or 5.9 μM. While it is possible to perform multiplexed detection of LAM, ACR, and Rv0363c with an LoQ of 50, 10, 100 ng mL^{-1} or 3.6, 0.6, 2.7 nM, respectively, lower levels of detection were pursued. The unique structure of LAM allows for pretreatment of the sample that removes a majority of the proteins from solution. Heat treatment produces an LoD for PILAM in serum of ~150 pg mL^{-1} or 8.8 pM, while perchloric acid treatment and subsequent and neutralization yields an LoD of 10 pg mL^{-1} or 1.0 pM.

The development of a reliable, cost effective, and field-deployable detection method for TB will help increase the chances of early diagnosis and reduced delay time in the start of therapeutic treatment. The detection of PILAM in spiked biological samples was performed in 17 h and can be analyzed with robust instrumentation for point-of-care detection. The implementation of new, reliable, and practical diagnostic methods could help save millions of lives worldwide.

4.5 References

(1) *Global Tuberculosis Report 2012;* World Health Organization: Geneva, 2012.

(2) Nester, E.; Aderson, D.; Roberts, C. E.; Nester, M. *Microbiology: A Human Perspective*. 5th ed.; McGraw-Hill: Boston, 2007; pp 593-595.

(3) Albanese, A.; Chan, W. C. W. *ACS Nano* **2011,** *5,* 5478-5489.

(4) Keeler, E.; Perkins, M. D.; Small, P.; Hanson, C.; Reed, S.; Cunningham, J.; Aledort, J. E.; Hillborne, L.; Rafael, M. E.; Girosi, F. *Nature* **2006,** *444,* 49-57.

(5) Brock, I.; Weldingh, K.; Lillebaek, T.; Follmann, F.; Andersen, P. *Am. J. Respir. Crit. Care Med.* **2004,** *170,* 65-69.

(6) Dorman, S. E. *Clin. Infect. Dis.* **2010,** *50,* S173-S177.

(7) Pai, M.; O'Brien, R. *Sem. Resp. Crit. Care M* **2008,** *29,* 560-568.

(8) Arias-Bouda, L. M. P.; Nguyen, L. N.; Ho, L. M.; Kuijper, S.; Jansen, H. M.; Kolk, A. H. *J. Clin. Microbiol.* **2000,** *38,* 2278-2283.

(9) *Tuberculosis (TB);* Centers for Disease Control and Prevention, U. S. Government Printing Office: Atlanta, 2012.

(10) Park, S.; Lee, B.; Cho, S.; Kim, W.; Lee, B.; Kim, S.; Kim, J. *Tuber. Lung Dis.* **1993,** *74,* 317-322.

(11) Apers, L.; Mutsvangwa, J.; Magwenzi, J.; Chigara, N.; Butterworth, A.; Mason, P.; Van der Stuyft, P. *Int. J. Tuberc. Lung Dis.* **2003,** *7,* 376-381.

(12) Githui, W.; Kitui, F.; Juma, E. S.; Obwana, D. O.; Mwai, J.; Kwamanga, D. *East Afr. Med. J.* **1993,** *70,* 263-266.

(13) Levy, H.; Feldman, C.; Sacho, H.; van der Meulen, H.; Kallenbach, J.; Koornhof, H. *Chest* **1989,** *95,* 1193-1197.

(14) Behr, M.; Warren, S.; Salamon, H.; Hopewell, P.; De Leon, A. P.; Daley, C.; Small, P. *Lancet* **1999,** *353,* 444-449.

(15) *Improving the Diagnosis and Treatment of Smear-negative Pulmonary and Extrapulmonary Tuberculosis Among Adults and Adolescents: Recommendations for HIV-prevalent and Resource-constrained Settings;* World Health Organization: Geneva, 2007.

(16) Boehme, C.; Molokova, E.; Minja, F.; Geis, S.; Loscher, T.; Maboko, L.; Koulchin, V.; Hoelscher, M. *Trans. R. Soc. Trop. Med. Hyg.* **2005,** *99,* 893-900.

(17) Davson, H. *Physiology of the Ocular and Cerebrospinal Fluid*; Elsevier: Amsterdam, 1956.

(18) Middlebrook, G.; Reggiardo, Z.; Tigertt, W. D. *Am. Rev. Respir. Dis.* **1977,** *115,* 1066-1069.

(19) Torres-Chavolla, E.; Alocilja, E. C. *Biosens. Bioelectron.* **2011,** *26,* 4614-4618.

(20) Kneipp, K.; Kneipp, H.; Itzkan, I.; Dasari, R. R.; Feld, M. S. *Chem. Rev.* **1999,** *99,* 2957-2976.

(21) Ni, J.; Lipert, R. J.; Dawson, G. B.; Porter, M. D. *Anal. Chem.* **1999,** *71,* 4903-4908.

(22) Palonpon, A.; Ichimura, T.; Verma, P.; Inouye, Y.; Kawata, S. *Appl. Phys. Express* **2008,** *1,* 092401.

(23) Willets, K. A.; Van Duyne, R. P. *Annu. Rev. Phys. Chem.* **2007,** *58,* 267-297.

(24) Wang, G.; J., L. R.; Jain, M.; Kaur, S.; Chakraboty, S.; Torres, M. P.; Batra, S. K.; Brand, R. E.; Porter, M. D. *Anal. Chem.* **2011,** *83,* 2554-2561.

(25) Dufek, E. J.; Ehlert, B.; Granger, M. C.; Sandrock, T. M.; Legge, S. L.; Herrmann, M. G.; Meikle, A. W.; Porter, M. D. *Analyst* **2010,** *135,* 2811-2817.

(26) Yakes, B. J.; J., L. R.; Bannantine, J. P.; Porter, M. D. *Clin. Vaccine Immunol.* **2008,** *15,* 227-234.

(27) Driskell, J. D.; Kwarta, K. M.; Lipert, R. J.; Porter, M. D.; Neill, J. D.; Ridpath, J. F. *Anal. Chem.* **2005,** *77,* 6147-6154.

(28) Grubisha, D. S.; Lipert, R. J.; Park, H. Y.; Driskell, J.; Porter, M. D. *Anal. Chem.* **2003,** *75,* 5936-5943.

(29) Mishra, A. K.; Driessen, N. N.; Appelmelk, B. J.; Besra, G. S. *FEMS Microbiol. Rev.* **2011,** *35,* 1126-1157.

(30) Snapper, S.; Melton, R.; Mustafa, S.; Kieser, T.; WR Jr, J. *Mol. Microbiol.* **1990,** *4,* 1911-1919.

(31) Yuan, Y.; Crane, D. D.; Simpson, R. M.; Zhu, Y.; Hickey, M. J.; Sherman, D. R.; Barry, C. E. *Proc. Natl. Acad. Sci.* **1998,** *95,* 9578-9583.

(32) Xolalpa, W.; Vallecillo, A. J.; Lara, M.; Mendoza-Hernandez, G.; Comini, M.; Spallek, R.; Singh, M.; Espitia, C. *Proteomics* **2007,** *7,* 3332-3341.

(33) Granger, J. H.; Granger, M. C.; Firpo, M. A.; Mulvihill, S. J.; Porter, M. D. *Analyst* **2013,** *138,* 410-416.

(34) Turkevich, J.; Stevenson, P. C.; Hillier, J. *Discuss. Faraday Soc.* **1951,** *11,* 55-75.

(35) Moskovits, M. *Rev. Mod. Phys.* **1985,** *57,* 783.

(36) Stamou, D.; Gourdon, D.; Liley, M.; Burnham, N. A.; Kulik, A.; Vogel, H.; Duschl, C. *Langmuir* **1997,** *13,* 2425-2428.

(37) *Commercial Serodiagnostic Tests for Diagnosis of Tuberculosis: Policy Statement*; World Health Organization: Geneva, 2011.

(38) Gaylord, H.; Brennan, P.; Young, D.; Buchanan, T. *Infect. Immun.* **1987,** *55,* 2860-2863.

(39) Hunter, S. W.; Gaylord, H.; Brennan, P. *J. Biol. Chem.* **1986,** *261,* 12345-12351.

(40) Hamasur, B.; Bruchfeld, J.; Haile, M.; Pawlowski, A.; Bjorvatn, B.; Källenius, G.; Svenson, S. B. *J. Microbiol. Methods* **2001,** *45,* 41-52.

(41) Haiss, W.; Thanh, N. T.; Aveyard, J.; Fernig, D. G. *Anal. Chem.* **2007,** *79,* 4215-4221.

(42) Patel, V. B.; Singh, R.; Connolly, C.; Kasprowicz, V.; Zumla, A.; Ndungu, T.; Dheda, K. *PLOS ONE* **2010,** *5,* e15664.

(43) Scopes, R. K. *Protein Purification: Principles and Practice*; Springer: Berlin, 2013.

CHAPTER 5

LOW-LEVEL DETECTION OF THE ANTIGENIC TUBERCULOSIS MARKER LIPOARABINOMANNAN IN HUMAN SERUM BY GOLD NANOPARTICLE LABEL AND SURFACE-ENHANCED RAMAN SCATTERING

5.1 Abstract

Diagnostic tests for tuberculosis (TB) are critical for patient care and global infection control. This paper describes the development and preliminary clinical accuracy assessment of a heterogeneous immunoassay that integrates an innovative serum pretreatment process with the detection capabilities of surface-enhanced Raman scattering (SERS) for the low-level detection of mannose-capped lipoarabinomannan (ManLAM). ManLAM is a 17.3 ± 5 kDa lipoglycan and a major component of the cell wall of *Mycobacterium tuberculosis* (*M. tuberculosis*), the causative agent of TB. ManLAM is also a major virulence factor in the infectious pathology of this disease and has been found in the urine, serum, sputum, and cerebral spinal fluid of infected patients. As a result, ManLAM has been one of the most investigated antigenic markers for TB diagnostics. The effectiveness of ManLAM as a marker, however, has remained unproven for reasons not well understood. To this end, we have found that the apparent sequestering of ManLAM

by its association with components in serum, and potentially other body fluids, has a strongly detrimental impact on the ability to detect the presence of this maker when performing an immunoassay. Herein we show that a simple serum pretreatment procedure can be used to disrupt the complexation of ManLAM with other serum components, enabling its detection at levels ~250x lower than that in untreated serum when using a SERS-based immunoassay. We have also carried out a preliminary assessment of the clinical accuracy of this approach using serum from 24 TB-positive patients (culture-confirmed) and 10 healthy controls. ManLAM was measurable in 21 of the 24 TB-positive specimens, but was not detectable in any of the 10 control specimens. More to the point, the levels of ManLAM measured in all 21 TB-positive specimens were well below the limit of detection for serum prior to pretreatment. Albeit for a small sample set, these findings translate to an exceptional level of clinical accuracy, that is, a clinical sensitivity of 87.5% and a clinical specificity of 100%. Taken together, these results not only provide much needed evidence for the clinical utility of ManLAM as a TB biomarker, but also demonstrate the potential of our overall approach to serve as a new diagnostic test for this disease. These findings, along with their possible implications vis-à-vis the difficulties found in earlier attempts to use ManLAM in TB diagnostics, are briefly discussed.

5.2 Introduction

Advances in tuberculosis (TB) diagnostics stand as one of the top priorities in global health.[1-3] TB is the world's second deadliest infectious disease. The challenges associated with combatting this disease are magnified by the suppression of immunological responses in individuals co-infected with human immunodeficiency virus (HIV) and the

emergence of drug-resistant strains of the causative agent of TB, *Mycobacterium tuberculosis* (*M. tuberculosis*).[4] The World Health Organization (WHO) estimates that there were 9.6M active cases of TB in 2014 and 1.5 million associated deaths; the majority (~80%) of these cases occurred in resource-limited countries.[4]

If diagnosed early, TB can be cured.[5] Early detection is also vital in containing the spread of the disease. However, sputum smear microscopy (SSM), the test most widely available in resource-limited areas of the world, cannot reliably detect early-stage infection.[6] Serological diagnostics, which rely on the detection of secondary markers of the disease (e.g., antibodies), have also proven ineffective in patients with an immune system compromised by HIV coinfection.[7-9] Nucleic acid amplification tests (NAATs) can be of immense value in early diagnosis,[9, 10] but have yet to be engineered and tested in formats that meet the rigor of the requirements for deployment in TB-endemic settings (e.g., low cost, short turn-around time, and ease of use).[10, 11]

In recognition of these challenges, there has been a refocus in TB diagnostics towards the direct detection of primary antigenic markers for *M. tuberculosis* in serum and other body fluids.[12, 13] This strategy parallels a proven approach for the early stage diagnosis of malaria and other diseases.[14] The potential merits of applying this approach TB include: (1) high clinical accuracy (i.e., high clinical sensitivity and clinical specificity);[1] (2) direct quantifiable evidence of the disease; (3) diagnosis of smear-

[1] Clinical sensitivity (SN) and clinical specificity (SP) measure diagnostic test accuracy. SN is defined as the percentage of infected individuals correctly identified by the test as infected; it is expressed as: [TP/(TP+FN)]100, whereas TP is the number of true positive tests and FN and is number of false negative tests. SP is the percentage of uninfected subjects correctly identified by a test as being uninfected; it is given as: [TN/(FP+TN)]100, whereas TN is the number of true negatives and FP is the number of false positives (FP). An ideal test has a SN and SP of 100%.

negative pulmonary infection; and (4) lack of dependence on a functioning immune system.[12, 13] Assays using serum and other body fluids may also be useful in diagnosing extrapulmonary TB;[7, 15] this form of TB accounts for ~10% of the globally infected population and is often found in children and HIV coinfected adults, rendering detection beyond that tractable in sputum specimens.[15, 16]

Several mycobacterial antigens have been found in serum and other body fluids (e.g., urine, sputum, and cerebral spinal fluid) of TB-infected patients.[12] The most widely investigated antigen for potential use as a marker in TB diagnostics is the mannose-capped lipoarabinomannan (ManLAM), a highly branched lipoglycan (17.3 ± 5 kDa)[17] unique to only mycobacteria.[8, 9, 13, 18-32] The strong interest in ManLAM reflects several factors. First, ManLAM is a major virulence factor in the infectious pathology of TB.[33] ManLAM suppresses immunological responses to bacterial infection, which include phagosome maturation, apoptosis, and interferon-gamma signaling in macrophages.[34] Second, ManLAM is a loosely associated but large fractional component (~40%) of the mycobacterial cell wall.[19, 35] It is, therefore, easily shed, potentially in large amounts, by metabolically active or degrading organisms into the circulation system of an infected patient. Nonetheless, the effectiveness of ManLAM as a TB marker remains unproven in spite of extensive investigations.[26]

Lipoarabinomannan has three unique structural components.[36] Two of these components, the mannosyl phosphate inositol anchor and the mannan backbone, are common to all mycobacteria. The third component, the capping region, is species dependent [e.g., the phosphoinositol-capped LAM of the nonpathogenic *M. smegmatis* (PILAM) and the mannose-capped ManLAM of pathogenic *M. Leprae*, *M. Bovis*, and *M.*

tuberculosis]. The underlying basis for the use of ManLAM therefore rests on the simple logic that if found in an individual in a TB-endemic region of the world, the likelihood of the infection originating from TB is extremely high.[4]

There is another important obstacle to the detection of this antigenic marker – its presence in the circulatory system both in its free and complexed forms.[19, 22, 37-39] The latter, referred to hereafter as complexed ManLAM, arises from its complexation with proteins and other components in body fluids. It is therefore reasonable to expect that the detection of ManLAM may be compromised due to the impact of steric effects on the binding and/or labeling of ManLAM in heterogeneous immunoassays.[26, 37]

The basis of the work described in this chapter reflects our hypothesis that the diagnostic strength of ManLAM for TB can be significantly improved by applying a simple, but vital, sample pretreatment step to disrupt ManLAM complexation before running the immunoassay. To test this hypothesis, we developed a sandwich immunoassay for the detection of ManLAM that combines gold nanoparticle (AuNP) labeling, ManLAM monoclonal antibodies (ManLAM mAbs), and readout by surface-enhanced Raman scattering (SERS). This approach draws on the continued focus of our[40-42] and other laboratories[43-45] on exploiting the strengths of SERS for low-level quantification of disease makers.[46-49] Herein, we show that the application of a simple pretreatment (acidification) process can significantly improves the limit of detection (LoD) of ManLAM in serum by ~250x over that for untreated serum. We also carried out a preliminary assessment of the clinical accuracy of this approach in tests of 24 TB-positive patients (culture-confirmed) and 10 healthy controls. As detailed, these findings demonstrate the potential of our approach to serve as an important addition to the TB diagnostics toolbox. Prospects and

challenges in extending this approach for use in clinical and other point-of-care settings, along with possible applications to other TB markers and different types of patient specimens and diseases, are also briefly discussed.

5.3 Experimental

5.3.1 Assay Format

Figure 5.1, overviews the details of our SERS-based immunoassay,[48] which sandwiches ManLAM between an extrinsic Raman label (ERL) and a capture substrate. ERLs are prepared by modifying 60-nm AuNPs with a thiolate monolayer that forms by the spontaneous adsorption of the disulfide-bearing Raman reporter molecule (RRM) 5-5'-dithiobis(succinimidyl-2-nitrobenzoate) (DSNB). This step is followed by the deposition of a layer of ManLAM mAbs, which forms by the adsorption of the mAb onto the hydrolyzed surface of the RRM.[50] This construction places the Raman scattering centers of the RRM monolayer in close proximity to the AuNP surface in order to maximize the SERS signal.[51, 52] The smooth, glass-supported gold (~200 nm thick) capture substrate is also coated with ManLAM mAbs adsorbed on the thiolate monolayer formed from the spontaneous adsorption of dithiobis(succinimidyl propionate) (DSP).[50] As a result, the presence of captured ManLAM in a sample is indirectly signaled by the characteristic Raman spectrum of the RRM, and the amount of ManLAM is indirectly quantified by the strength of its most intense spectral feature [i.e., its symmetric nitro stretch, $\nu_s(NO_2)$, centered at 1336 cm^{-1}].

It is worthwhile to note some of the considerations that we have adopted in moving SERS forward as a reliable analytical measurement tool in diagnostics. This relates, in

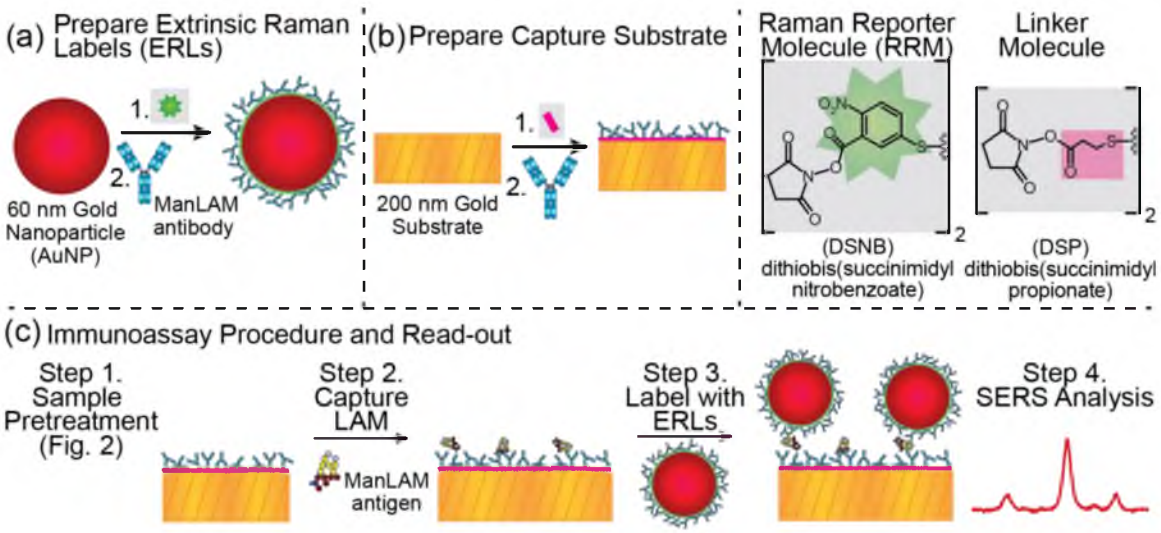

Figure 5.1. The three main components of the SERS-based immunoassay approach for LAM detection: (a) ERL preparation; (b) capture substrate preparation; and (c) major assay steps. The first two procedures are completed prior to the assay. The assay is carried out by incubating a treated (see Experimental Section) serum sample (20.0 μL) at room temperature with the capture substrate. The samples are then rinsed, exposed to ERLs (20.0 μL), rinsed again, dried under ambient conditions, and analyzed by SERS.

large part, to designing an assay in which the enhanced response for SERS is reproducibly managed.[53] In our case, reproducibility is controlled by: (1) the size and shape distribution of the gold nanoparticles that constitute the ERL core, (2) the ability to form a monomolecular layer of RRMs and mAbs on the ERLs; and (3) the use of a smooth gold capture substrate. The latter component is particularly important due to the plasmonic coupling between the gold core of the ERL and the gold support[54] of the capture substrate. We also use UV-Vis spectrophotometry, per the method by Haiss, and collaborators,[55] to maintain a fixed concentration of ERLs in the suspension used to tag the captured antigen. We add that Class A volumetric flasks were used in all appropriate solution preparations and that all reagent and antigenic solutions were deposited on the capture substrate using calibrated pipettes (Pipette Repair Service, Midlothian, VA).

5.3.2 Extrinsic Raman Labels (ERLs)

The preparation[48] and plasmonic signal optimization[54] of ERLs and the synthesis of DSNB[42] have appeared elsewhere. The preparative steps are summarized in Figure 5.1a. First, an aqueous suspension of 60-nm (nominal diameter) AuNPs (NanoPartz, Loveland, CO) in 2.0 mM borate buffer (BB, pH 8.5, Thermo Scientific) was mixed for 1.5 h with DSNB (10.0 mM in acetonitrile, spectroscopy grade, Sigma-Aldrich) at 4°C. This step yielded a DSNB-derived thiolate monolayer on the AuNP surface that forms via disulfide cleavage. Next, a small aliquot (10.0 μL at 100 μg/mL) of the ManLAM mAb CS906.7 (BEI Resources, Manassas, VA)[56] was added to the suspension, which was incubated for 1 h at 4°C; the selection of this mAb is detailed below. This step was followed by pipetting 100-μL of 10% (w/v) bovine serum albumin (BSA, 2.0 mM BB, Sigma-Aldrich) into this

suspension and then incubating the resulting suspension at room temperature for 1 h. BSA serves as a blocking agent and a stabilizer of the colloidal suspension. This suspension was subsequently centrifuged at ~2,000*g* for 10 min, and the clear supernatant was carefully removed. The ERL pellet was resuspended in 1.0 mL of 1% BSA in 2.0 mM BB, and the centrifugation and resuspension steps were repeated two more times, with the final resuspension using 0.25 mL of 2% BSA in 2.0 mM BB with 150 mM NaCl (Thermo Scientific) to achieve an ERL concentration of 8.0 x 10^{10} particles/mL. In work in preparation for submission elsewhere,[57] measurements of the amounts of DSNB and mAbs coated on the ERLs varied by ±5.0 and ±10.2%, respectively.

5.3.3 Capture Substrate

Capture substrates (Figure 5.1b) were prepared with 1x1 cm glass squares that supported a 200-nm layer of template stripped gold (TSG).[58] A 2-mm diameter address was created in the center of the substrate by octadecanethiol (ODT, Fluka) microprinting with polydimethylsiloxane (PDMS, Dow Corning SlyGuard).[59] The ODT layer produced a hydrophobic boundary around an uncoated 2-mm address, which was modified for 1 h with an ethanolic solution of DSP (1.0 mM, Thermo Scientific). Next, the DSP-derived monolayer was reacted with a 20.0 µL drop of capture antibody (2.5 µg/mL, CS906.7 ManLAM mAbs) for 1 h to form a layer of ManLAM mAbs on the hydrolyzed surface. The substrate was then rinsed three times with phosphate-buffered saline containing 0.1% Tween 20 (PBST, pH 7.4, Fisher Scientific); blocked with 20.0 µL of StartingBlock (Thermo Scientific) for 1 h; rinsed three more times with PBST; and exposed (Figure 5.1c) to 20.0 µL of a ManLAM-containing sample. After 1 h, the sample was rinsed three times

with 2 mL of 2.0 mM BB (150 mM NaCl and 0.1% Tween 20), exposed to 20.0 μL of the ERL suspension, and incubated for 16 h. Finally, the sample was rinsed with 2 mL of 2.0 mM BB, containing 10.0 mM NaCl and 0.10% Tween 20, and dried under ambient conditions for ~1 h prior to SERS interrogation.

5.3.4 ManLAM mAb Selection

Three ManLAM mAbs (IgG_3 subclass) were screened for effectiveness in our SERS assay (Figure 5.1). We note that the same antibodies were screened in the work detailed in the companion paper,[60] using PILAM as the antigen. These mAbs, which are designated as CS906.1, CS906.7, and CS907.41, were first prepared and characterized for reactivity at Colorado State University in 1987.[56] Each of their possible nine combinations was tested for the capture and/or the ERL tagging of PILAM by measuring the SERS response of PBST spiked with 5.0 μg/mL of PILAM. The levels of nonspecific ERL adsorption were also determined for PBST devoid of PILAM. These results of the nine tests with spiked PILAM indicated that the signal measured using the CS906.7 mAb for both the capture and labeling of PILAM was about two times stronger than any of the other eight mAb combinations. ManLAM detection required higher levels than found for PILAM, which indicates a higher affinity for PILAM by CS906.7. In contrast, the responses for the nine mAb combinations for the PBST blanks were barely distinguishable from each other by statistical analysis. Based on these results, the CS906.7 mAb was used as the capture and labeling mAb in all subsequent experiments. We note that the epitope structures of either PILAM or ManLAM that are recognized by CS906.7 have not been characterized. However, the structure of PILAM and ManLAM is consistent with the

presence of a multiplicity of structurally similar antigenic determinants that could react with CS906.7.[56]

5.3.5 Instrumentation and Sample Readout

The Raman spectrometer used was a modified NanoRaman system (Concurrent Analytical, Loveland, CO).[61] This instrument has three primary components: laser excitation source, fiber optic probe, and spectrograph. The light source is a 22-mW, 632.8-nm HeNe laser with a spectrograph consisting of an f/2.0 Czerny Tuner imaging spectrometer with 6-8 cm^{-1} resolution and a Kodak 0401E charged coupled device (CCD) thermoelectrically cooled to 0°C.

SERS readout was performed after the samples had fully dried under ambient conditions (~1 h). Raman spectra were collected at a 1-s integration time by irradiating a 20-μm spot on the sample surface at a laser power of 3.0 mW. The laser power was checked periodically in each run and varied by no more than 0.1 mW. Upon assay completion, 10 different locations on each sample with from triplicate samples were analyzed. All spectra were baseline corrected and the height of the $\nu_s(NO_2)$ of the RRM adlayer on the ERLs was used for quantification.

5.3.6 Control and TB-Patient Serum

The serum used for the development of the assay and the generation of calibration curves (i.e., serum spiked with ManLAM) was prepared using human serum [Human AB Serum (Mediatech, Inc., Manassas, VA)]. The vendor prepares this product, referred to hereafter as negative human serum, by pooling and sterilizing donor plasma collected at

centers across the United States. This serum was stored at –30°C and slowly thawed in the laboratory to ambient temperature immediately prior to use. All calibration data are presented as the average and standard deviation of the collected spectra (i.e., a spectrum from 10 different locations per sample from triplicate samples).

The TB-positive sera were collected from patients in South Africa who were enrolled in the Tuberculosis Trials Consortium Study Group 22 (TBTC-22) with culture-confirmed cavitary TB.[62] This study group participated in a randomized clinical trial that was designed to test the effectiveness of the antiTB drugs rifapentine and isoniazid in treating pulmonary TB in adult, HIV-negative patients. These deidentified samples were procured by Colorado State University from the Centers for Disease Control and Prevention (CDC) after TBTC-22 approval. This specimen set consisted of 24 different serum samples (deidentified), each at a volume of ~100 μL. We do not have information with regard to treatment status (e.g., drug regimen or time course of treatment) for any of these specimens. However, tests for immunoblot reactivity confirmed the presence of ManLAM antibodies in all TB-positive specimens, but not in any of the healthy controls (data not shown). These results suggest that there was a high likelihood that ManLAM antigen would also be present in the TBTC-22 study serum specimens.

Healthy, nonendemic control sera, referred to hereafter as healthy controls, were obtained from U.S.-born residents of Colorado. These non-Bacillus Calmette–Guérin (BCG)-vaccinated residents gave informed consent to participate in a study of reactivity to *M. leprae* and *M. tuberculosis* antigens.[63] These residents had no known exposure to TB or leprosy and did not work in a mycobacterial laboratory.

All patient specimen orders and healthy control collections were performed under

approved IRB protocols at Colorado State University. All assay steps were carried out in a biosafety cabinet contained in a BSL-2 (enhanced) laboratory.

5.3.7 Serum Pretreatment

As detailed in the companion paper,[60] the detection of PILAM directly from serum yielded signal strengths that were negatively affected by complex formation[37-39] and much weaker than those for PILAM spiked into PBST at similar levels. We therefore adapted a classic pretreatment procedure[64] designed to disrupt complexation via protein denaturation. This procedure, which was applied herein for ManLAM for the same reasons, consists of five steps as outlined previously in Figure 5.2. It begins (Step 1) by adding 2.0 μL of $HClO_4$ (70%, Sigma-Aldrich) to 100.0 μL of each calibration/patient sample in a small centrifuge tube, which brings the pH to ~2 and forms a milky suspension. After vortexing for 10 s and centrifuging at 13,000*g* for 5 min (Step 2), 75.0 μL of the resulting supernatant were transferred to a second centrifuge tube (Step 3) and neutralized to pH 7.5 with 6.0 μL of an aqueous solution of K_2CO_3 (2.0 mM, Fisher Scientific) (Step 4). The samples were then cooled to 4 °C for 30 min to accelerate $KClO_4$ precipitation, warmed to room temperature (~20 min) before being pipetted (20.0 μL) onto the capture substrate (Step 5).

We note that ManLAM is acid-labile.[65-67] We have found, however, that such degradation appears to not have an effect on the reproducibility of the dose-response plots presented later in Chapter 5. Experiments to quantify the potential impact of the serum pretreatment process on the recovery of ManLAM are planned.

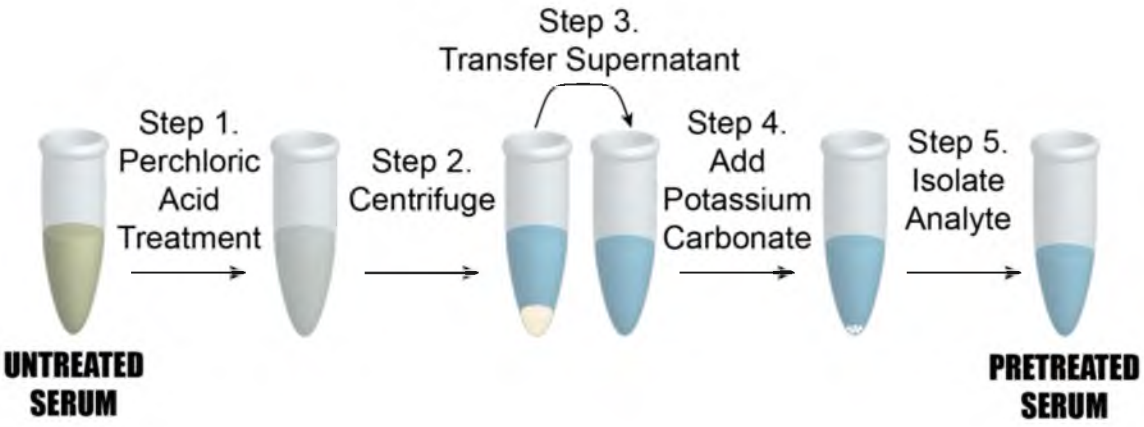

Figure 5.2. Step-by-step schematic of pretreatment procedure employing perchloric acid to free mannose-capped lipoarabinomannan (ManLAM) from complexation with proteins and other components in human serum. A 100-µL aliquot of human serum is treated with perchloric acid and vortexed to ensure proper mixing. Next, the protein precipitation in spun down and the protein pellet discarded. Finally, the supernatant containing ManLAM is treated with potassium carbonate to neutralize the perchloric acid. This step produces a precipitate results in a much cleaner sample matrix in the supernatant.

5.3.8 Data Analysis

Due to the small volumes received for the TB-positive and TB-negative serum specimens (~100 μL), the patient serum samples were run as duplicates. As a consequence, the levels of ManLAM in all patient samples are reported as averages and uncertainties as the range of the values from reading 10 sites per sample from 2 separate substrates prepared from a single specimen.

The serum blank specimens had an average response of 64 cts/s, with a standard deviation of 11 cts/s. We employed a confidence interval of >99% to define the LoD, which yielded a signal on the calibration curve that matched the blank response (64 cts/s) plus three times its standard deviation (± 11 cts/s) for a cutoff of 97 cts/s. Patients were identified when using our SERS-based assay as "TB-positive" if the level of ManLAM was statistically measurable above the LoD. The fit to the data for the pretreated calibration samples used a linear least squares approach for the data spanning the blank serum samples up to serum samples spiked at 100 ng/mL ($y = 12.9x + 64.1$). For samples with signals beyond the linear portion of the dose-response plot (that is, ManLAM concentrations above ~100 ng/mL), a second order polynomial fit ($y = -0.00727x^2 + 13.5x + 64.1$) was used for quantification.

5.4 Results and Discussion

5.4.1 Preliminary Findings

As a starting point for this work, we conducted a set of studies to assess the effectiveness of our assay strategy by spiking PILAM derived from *M. smegmatis*, which is often used as a model in mycobacterium research for PILAM because of its

nonpathogenic nature and its fast growth in culture,[68-70] into negative human serum. *M. smegmatis* shares more than 2000 homologs with *M. tuberculosis*; and the cell wall structure is similar for both.[69] That work, detailed in the companion paper,[60] demonstrated the impact of complex formation on the detection of PILAM spiked at low levels into human serum, and pointed to component(s) in serum with a molecular weight (>100kDa) as likely culprits.

5.4.2 ManLAM Measurements in Untreated and Pretreated Human Serum

The first assessment of the potential merits of our integrated approach focused on a comparison of assays that analyzed ManLAM after spiking it into untreated, negative human serum and then subjecting the spiked serum samples to the acid pretreatment protocol per Figure 5.2. The SERS spectra and dose-response plot for the untreated samples are shown in Figure 5.3. Theses samples included serum banks and serum spiked with ManLAM in concentrations from 0 to 10 μg/mL. There are three important points to draw from these spectra (Figure 5.3a). First, all of the observable spectral features can be assigned to functional groups of the monomolecular coating of the RRM on the ERLs (for example, $\nu_s(NO_2)$ at 1336 cm^{-1} and aromatic ring mode at 1558 cm^{-1} of the DSNB-derived coating).[48] None of the vibrational modes of the ManLAM mAb layer on the ERLs are detectably enhanced. Second, the strengths of the spectral features increase with increasing amounts of ManLAM spiked into serum. This dependence follows expectations for a sandwich immunoassay. Third, there is evidence for a small, but measureable, level of ERL adsorption in the spectrum for the negative control. We attribute this observation to the

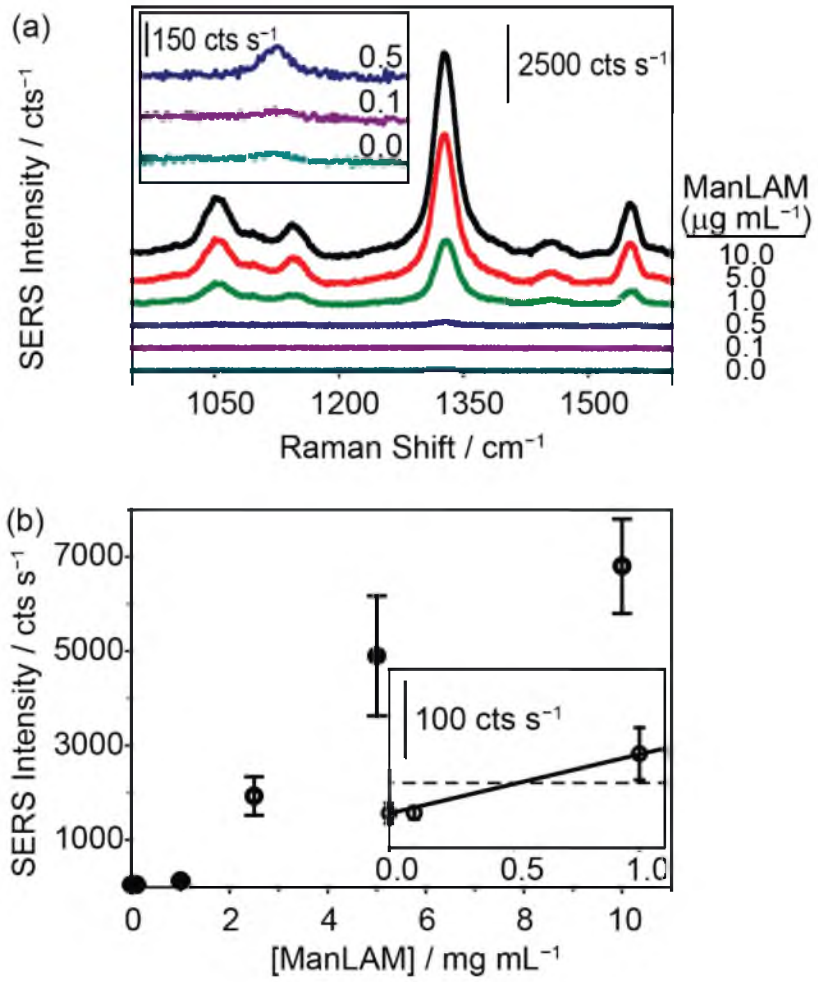

Figure 5.3. SERS-based immunoassay for ManLAM spiked into untreated serum. (a) SERS spectra from a calibration run using ManLAM-spiked negative human serum: (i) 10.0 (ii) 5.0; (iii) 2.5; (iv) 1.0; (v) 0.10; and (vi) 0.0 μg/mL. The spectra are offset vertically for visualization. (b) Dose-response plot from averaging triplicate calibration runs (20.0 μL) for ManLAM spiked from 0.10 to 10.0 μg/mL into human serum and a negative control sample. The LoD was estimated to be ~0.5 μg/mL (30 nM). It was determined as the signal for the blank sample plus three times its standard deviation via the data shown in the inset ($y = 83.2x + 48.1$; $R^2 = 0.99$.) The signal at the cutoff for the LoD is indicated by the dashed black line in the inset.

effectiveness of the blocking agent and other preparative procedures (Experimental Section) to reduce nonspecific adsorption.

The dose-response plot for ManLAM in untreated serum is shown in Figure 5.3b.It was constructed from the average signal for the strongest feature in the SERS spectrum, $\nu_s(NO_2)$, from 10 different locations per sample and triplicate samples for each calibration point. The response at low levels of ManLAM follows a linear dependence. Though not shown, the response at higher ManLAM concentrations begins to level off (~5 μg/mL) as binding sites on the capture substrate approach saturation, plateauing at ~10 μg/mL. The LoD, calculated as the response on the calibration line that matches the blank signal plus three times its standard deviation, is ~500 ng/mL. This value is ~100x greater than the LoD found for PILAM from *M. smegmatis*, which is phosphoinositol-capped, using the same set assay conditions.[60] As noted earlier, this difference is attributed to the lower affinity of the CS906.7 mAb for ManLAM versus that for PILAM.

Following the hypothesis that the complexes formed between ManLAM and serum constituents sterically inhibit binding to the capture mAb, the next set of assays analyzed the ManLAM-spiked sera after completing the acid-treatment procedure illustrated in Figure 5.2. Indeed, this assertion is in accord with a growing body of evidence for the presence of complexes for ManLAM in human serum,[19, 22, 23, 37-39, 71] the most recent being the strong association of ManLAM with high density lipoproteins (HDLs).[37] The impact of pretreatment is immediately evident in the results presented in Figure 5.4, which shows that the spectral responses for the pretreated samples are much stronger than those of the untreated samples. This difference is particularly evident when comparing the responses for a ManLAM concentration of 100 ng/mL. With the untreated sample, the response at

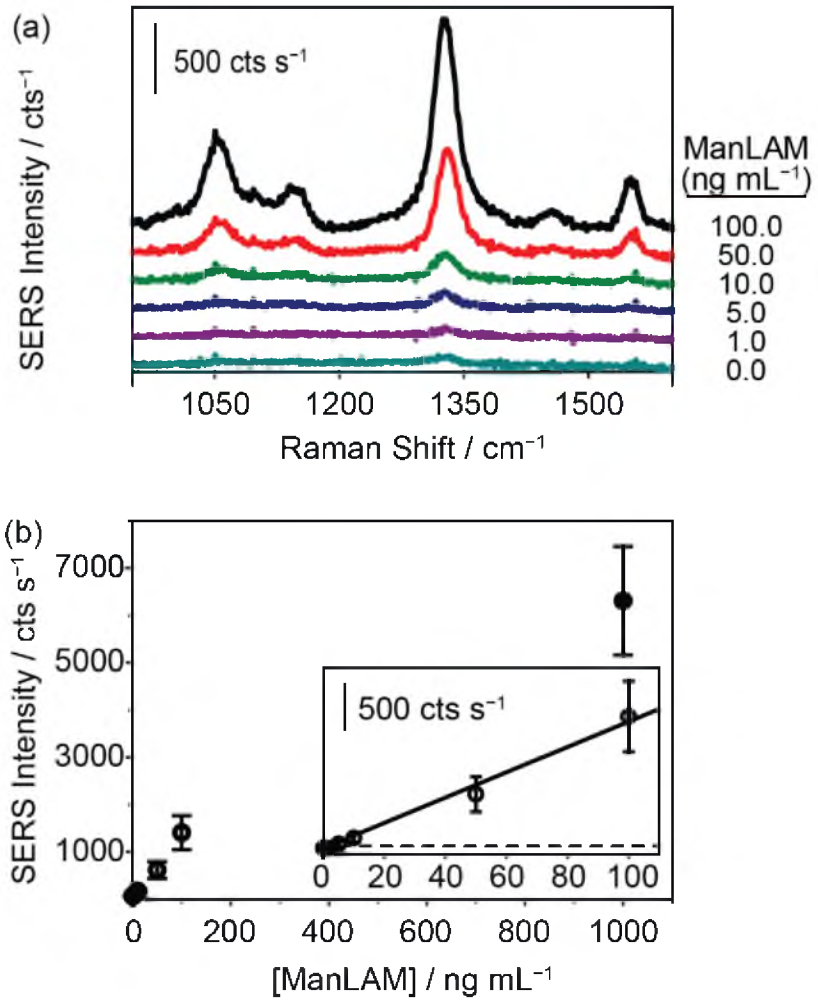

Figure 5.4. SERS-based immunoassay for ManLAM in pretreated human serum. (a) SERS spectra using ManLAM-spiked into negative human serum followed by pretreatment: (i) 100.0 (ii) 50.0; (iii) 10.0; (iv) 5.0; (v) 1.0; and (vi) 0.0 ng/mL. The spectra are offset vertically for visualization. (b) Dose-response plot for triplicate calibration runs (20.0 μL pretreated serum samples) for ManLAM spikes from 1.0 to 1000 ng/mL and a negative (pretreated serum) control sample. The LoD was estimated to be ~2 ng/mL (~0.1 nM). It was determined as the signal on the calibration plot that matches the blank signal plus three times its standard deviation via the data shown in the inset ($y = 12.9x + 64.1$; $R^2 > 0.99$). The signal at the cutoff for the LoD is indicated by the dashed black line in the inset.

100 ng/mL is indistinguishable from that of the serum blank, whereas the signal for the acid pretreated specimen is slightly above 1400 cts/s. Another comparison shows that the signal for the untreated ManLAM sample at 1 μg/mL (~130 cts/s) is close to the response (~170 cts/s) for the pretreated sample at a 100x lower ManLAM level, 0.010 μg/mL.

The dose-response plot, obtained from triplicate samples for each calibration point runs for ManLAM spiked into negative human serum and then acid pretreated, is shown in Figure 5.4b. Like the data for ManLAM spiked into human serum without pretreatment (Figure 5.3), the response at low ManLAM levels follows a linear dependence and plateaus (data not shown) at higher amounts of ManLAM as mAb binding sites on the capture substrate begin to saturate. The LoD from an analysis of these data is ~2 ng/mL or ~250x below that in serum prior to pretreatment.

These results have another potentially important implication with respect to understanding the huge discrepancies observed in other studies that have examined the clinical accuracy of ManLAM from the urine of TB-infected patients. If we assume that the complexed form of ManLAM has a molecular weight above 100 kDa per the companion paper,[60] then the ~30 kDa cutoff for passage by the filtration mechanisms of the kidneys would preclude passage of the complex into urine. ManLAM would then only be a viable diagnostic maker in urine specimens from patients suffering from renal failure. Such a train of thought is consistent with the increased performance levels reported in tests for ManLAM in the urine of HIV co-infected individuals.[13, 19-21, 30, 31, 72, 73]

5.4.3 TB-Patient Assay

To test further the hypothesis that an effective pretreatment method significantly improves the utility of ManLAM as a diagnostic TB marker, we analyzed 24 TB-positive (identifiers #1 to #24) and 10 healthy control (identifiers #25 to #34) serum specimens. The post pretreatment results for the assays of the 34 specimens are presented in Figures 5.5 and 5.6 and in Table 5.1. The small specimen volumes precluded the opportunity to compare the responses of these samples before and after pretreatment. Figure 5.5 summarizes these measurements by using histograms to represent the average signal strength of the $\nu_s(NO_2)$ spectral feature measured for each sample, and includes a delimiter (dashed black line) for the LoD (2 ng/mL) of the SERS assay. Figure 5.6 consists of a small set of specimen spectra for illustrative purposes; it includes spectra for two of the healthy control samples (#25 and #30) and four of the TB-positive samples (#5, #6, #10, and #12).

As evident in Figure 5.5, ManLAM was detectable using our overall approach in 21 of the 24 TB-positive samples. ManLAM was not found in three of the TB-positive samples (i.e., # 5, #7, and #15) or in any of the 10 healthy control specimens (i.e., ManLAM < 2 ng/mL). Importantly, these results yield a clinical sensitivity of 87.5% and a clinical specificity of 100%, both of which are rivaled only by NAAT tests.

Further inspection of these data per Table 5.1 points to three generalizable ranges for the ManLAM levels found in these patient serum specimens. First, a few of the TB-positive samples have ManLAM (#11, #12, #17, #18, and #22) greater than 100 ng/mL. Second, a few other samples (#2, #3, #6, #13, and #19) have ManLAM detectable levels above the LoD but below 20 ng/mL. Third, ManLAM levels in the majority of samples (#1, #4, #8, #9, #10, #14, #16, #20, #21, #23, and #24) is between 20 and 100 ng/mL. While

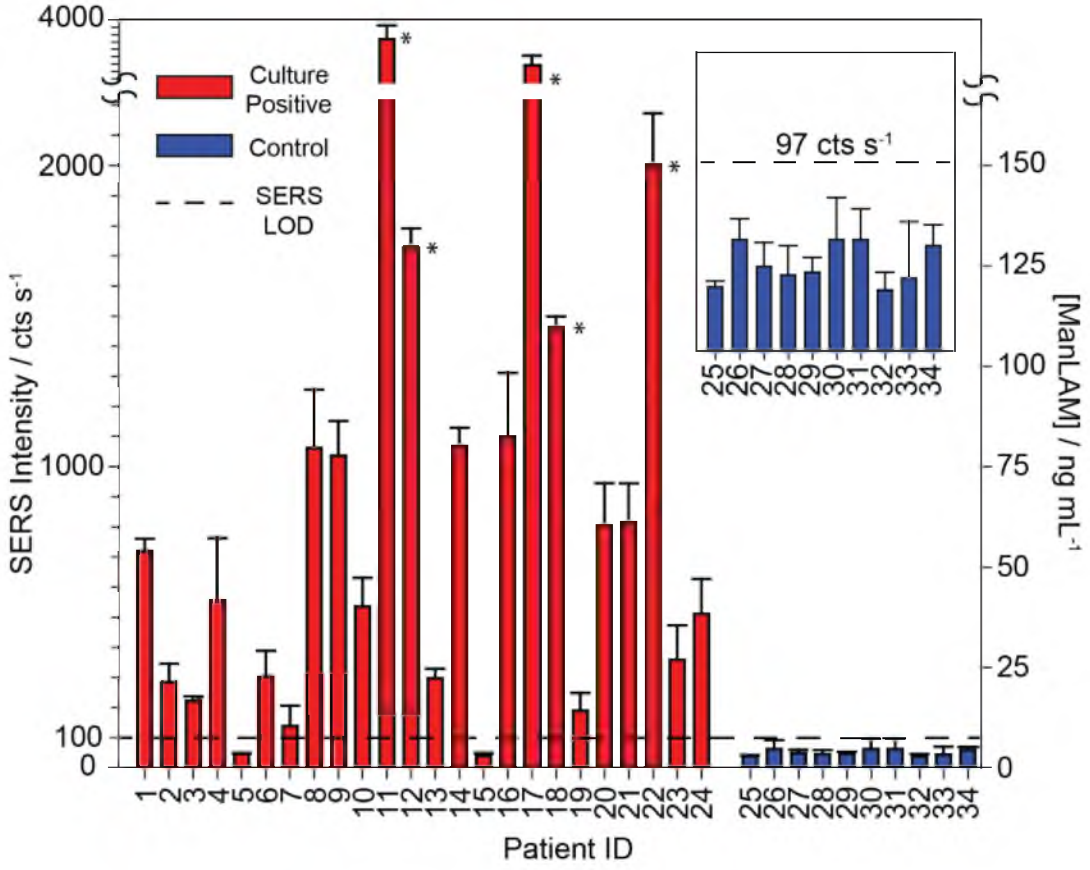

Figure 5.5. SERS analysis of patient serum (pretreated) for the quantification of ManLAM represented in a bar chart. The black dashed-line delimiter represents the SERS LoD. The red bars indicate patient specimens that have been determined as TB+, based on culturing, and the blue bars represent patient specimen that are TB-, based on culturing. The average SERS signal is calculated from the peak height of the $\nu_s(NO_2)$ from baseline-corrected SERS spectra, and all error bars represent the standard deviation of the response at ten different locations on duplicate samples.

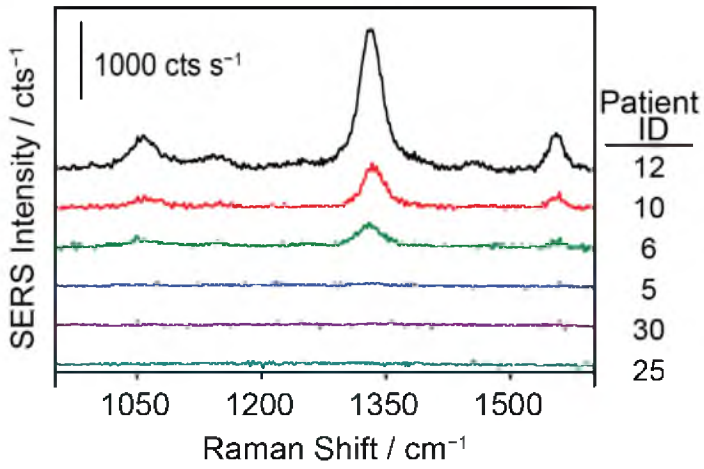

Figure 5.6. Representative SERS spectra from patient serum (pretreated) samples. Samples #25 and # 30 are healthy control serum specimens. Samples #5, #6, #10, and #12 are TB positive patient serum specimens. Sample #5 represents a patient sample below the LoD.

Table 5.1. Patient Sample Identification with Corresponding SERS Responses and Levels of Mannose-capped Lipoarabinomannan.

Sample ID	SERS / cts s^{-1}	ManLAM / ng mL^{-1}
1	728 ± 41	52 ± 3
2	282 ± 61	17 ± 5
3	219 ± 16	12 ± 1
4	553 ± 208	38 ± 16
5	43 ± 3	ND
6	301 ± 86	18 ± 7
7	131 ± 67	ND
8	1059 ± 194	77 ± 15
9	1034 ± 116	75 ± 9
10	533 ± 96	36 ± 7
11	3710 ± 208	328 ± 16
12	1728 ± 61	129 ± 5
13	295 ± 31	18 ± 2
14	1065 ± 61	78 ± 5
15	37 ± 9	ND
16	1096 ± 214	80 ± 17
17	3349 ± 173	288 ± 13
18	1460 ± 36	108 ± 3
19	187 ± 60	10 ± 5
20	803 ± 139	57 ± 11
21	814 ± 129	58 ± 10
22	2001 ± 170	157 ± 13
23	356 ± 115	23 ± 9
24	509 ± 146	35 ± 11
25	36 ± 4	ND
26	60 ± 15	ND
27	47 ± 11	ND
28	42 ± 14	ND
29	44 ± 7	ND
30	59 ± 27	ND
31	60 ± 21	ND
32	35 ± 8	ND
33	41 ± 27	ND
34	56 ± 11	ND

Notes: The calculated ManLAM levels are derived from the linear fit equation from the calibration curve ($y = 12.9x + 64.1$) for ManLAM ranging from 0-100 ng/mL in pretreated human serum. SERS responses corresponding ManLAM >100 ng/mL are calculated from a second order polynomial fit. ($y = -0.00727x^2 + 13.5x + 64.1$) ND (not detected), that is, ManLAM below the LoD in human serum of 2 ng/mL.

not able to offer any correlations between ManLAM levels and the stage of disease progression, the ability to quantify small differences in ManLAM levels in TB-patient sera suggests that our approach may be useful in monitoring treatment responses, in determining the optimal duration of therapy, and in assessments of new drug treatment regimens and vaccines.[74-76]

These data also show that the responses for 3 of the TB-positive patient samples (#5, #7, and #15) were not distinguishable from those of the calibration blank or any of the controls. The inability to detect ManLAM in these specimens is attributed to one or a combination of three possibilities: (1) ManLAM was present in these three specimens at levels below the LoD of the assay; (2) these patients may have had a positive response to one of the drug treatments used in the TBTC-22 clinical trial; and (3) these specimens may have degraded during storage and/or shipment prior to receipt or from freeze/thaw cycling when realiquoted for distribution.

Finally, these data show that the responses for all 10 healthy control samples were commensurate with that of the serum blank used in the construction of the calibration plot. The spectra for sample #25 and #30 in Figure 5.6 are representative of those for the remaining healthy control samples. Moreover, we were unable to detect the presence of nonspecific ERL adsorption in these samples even after increasing the signal acquisition time from 1 to 60 s (data not shown).

Taken together, these results support the potential value of our integrated approach for the detection of TB. Experiments to validate more fully the performance of this methodology by analyzing a much larger specimen sample set and to evaluate other types of patient specimens (e.g., noncavitary lung disease, TB patients coinfected with HIV,

children and those with extrapulmonary infections) are being planned. We also believe that one of the obstacles in the detection of ManLAM in other body fluids (e.g., urine and cerebral spinal fluid) is likely to be a consequence of very low concentrations of unbound antigen due to complexation. Efforts to more fully determine the mechanistic underpinnings of pretreatment and quantify recovery efficiencies are underway. We are also developing plans to evaluate the impact of pretreatment on ManLAM determinations by ELISA and other diagnostic platforms.

5.5 Conclusions and Prospectus

These results begin to demonstrate the potential of ManLAM to serve as a long sought-after antigenic marker for TB and of our technological approach to become an exciting addition to the TB diagnostics toolbox. It is important, however, to ground these preliminary results with a reality check in terms of the many-faceted obstacles faced by TB diagnostics in meeting the global challenges in fighting this disease.

First and foremost is the challenge to prove the effectiveness of our ManLAM assay through an extensive series of validation studies. While the results herein point to a potential technical solution for a test for active infection, an extensive series of validation studies must be carried out. Both the number of specimens and types of specimens must be markedly increased. Examples of the types of specimens include those from patients who are TB-positive and HIV- positive; have cavitary, noncavitary, and extrapulmonary TB; and have been BCG (bacilli Calmette-Guerin) vaccinated. Longitudinal studies are also needed to validate the effectiveness of the test in for determining the stage of disease progression and in providing means to monitor the response to treatment. The goal of these

validation studies is to quantify the clinical sensitivities and clinical specificities of ManLAM for each of these manifestations of TB, which requires specimens that are well characterized in terms of clinical symptoms, comparative data from other TB tests, (e.g., culture and molecular tests), and exacting patient health histories. Interestingly, the 2006 Global Health Diagnostics Forum, which was convened by the Bill and Melinda Gates Foundation, estimated that a rapid and globally accessible diagnostic test for active TB infection which has a clinical sensitivity ≥85% and a clinical specificity of ≥97% could help save ~400,000 lives each year.[77] Our small data set suggests that we may be able to reach these metrics, but it remains to be seen if this level of effectiveness can be realized with ManLAM alone or if a multiplexed test to include other antigenic markers for TB will be required. Interestingly, the latter possibility can be addressed by drawing on the extensibility of our[78] or other[11, 79, 80] platforms. There have also been recent efforts aimed at improving ManLAM detection by developing more specific and higher affinity antibodies,[81] which may again lower the LoD, and therefore further improve clinical accuracy. We also note that there are a few other promising platforms for ManLAM detection,[82] but any attempt to draw comparisons of performance is not possible as the capture and labeling reagents are not the same.

Another challenge revolves around accessibility in the regions of the world where the test is needed the most. The only platforms today that have a high clinical accuracy are microbial culturing and a NAAT test,[10] but both have a cost, complexity, and/or specimen type limitation that impedes widespread use in resource-limited settings.[7] Within this context, there are several development issues that need to be addressed with respect to instrumentation, sample processing, and reagent packaging and stability before potentially

transitioning our approach from the research laboratory to field settings. More so, issues differ depending upon whether the test will be conducted in settings with reliable infrastructure (e.g., hospital clinic) in terms of power, sample refrigeration/freezing, and technical skills, or if the intent is to create a field-deployable (e.g., point-of-need) test in which case the infrastructure and technical capabilities may be limited. In either case, approaches to streamline sample preparation and readout, instrument and test standardization and calibration, reagent packaging and handling, and overall ease of use must be addressed.

5.6 References

(1) Phillips, L. *Nature* **2013,** *493,* 14.

(2) Pai, M.; Kalantri, S.; Dheda, K. *Expert Rev. Mol. Diagn.* **2006,** *6,* 423-432.

(3) Dorman, S. *Int. J. Tuberc. Lung Dis.* **2015,** 504-516.

(4) *Global Tuberculosis Report;* World Health Organization: Geneva, 2015.

(5) Zumla, A.; Raviglione, M.; Hafner, R.; Fordham von Reyn, C. *N. Engl. J. Med.* **2013,** *368,* 745-755.

(6) Steingart, K. R.; Ng, V.; Henry, M.; Hopewell, P. C.; Ramsay, A.; Cunningham, J.; Urbanczik, R.; Perkins, M. D.; Aziz, M. A.; Pai, M. *Lancet Infect. Dis.* **2006,** *6,* 664-674.

(7) Steingart, K. R.; Flores, L. L.; Dendukuri, N.; Schiller, I.; Laal, S.; Ramsay, A.; Hopewell, P. C.; Pai, M. *PLOS Medicine* **2011,** *8,* e1001062.

(8) Patel, V. B.; Singh, R.; Connolly, C.; Kasprowicz, V.; Zumla, A.; Ndungu, T.; Dheda, K. *PLOS ONE* **2010,** *5,* e15664.

(9) Perkins, M. D.; Cunningham, J. *J. Infect. Dis.* **2007,** *196,* S15-S27.

(10) Theron, G.; Pooran, A.; Peter, J.; van Zyl-Smit, R.; Mishra, H. K.; Meldau, R.; Calligaro, G.; Allwood, B.; Sharma, S. K.; Dawson, R. *Eur. Respir. J.* **2012,** *40,* 161-168.

(11) Liong, M.; Hoang, A. N.; Chung, J.; Gural, N.; Ford, C. B.; Min, C.; Shah, R. R.; Ahmad, R.; Fernandez-Suarez, M.; Fortune, S. M. *Nature communications* **2013,** *4,* 1752.

(12) Abebe, F.; Holm-Hansen, C.; Wiker, H.; Bjune, G. *Scand. J. Immunol.* **2007,** *66,* 176-191.

(13) Reither, K.; Saathoff, E.; Jung, J.; Minja, L.; Kroidl, I.; Saad, E.; Huggett, J.; Ntinginya, E.; Maganga, L.; Maboko, L. *BMC Ifect. Dis.* **2009,** *9,* 141.

(14) *Malaria Rapid Diagnostic Test Performance;* World Health Organization: Geneva, 2010.

(15) Norbis, L.; Alagna, R.; Tortoli, E.; Codecasa, L. R.; Migliori, G. B.; Cirillo, D. M. *Expert Rev. Anti Infec. Ther.* **2014,** *12,* 633-47.

(16) Piccini, P.; Chiappini, E.; Tortoli, E.; de Martino, M.; Galli, L. *BMC Ifect. Dis.* **2014,** *14,* S4.

(17) Venisse, A.; Berjeaud, J. M.; Chaurand, P.; Gilleron, M.; Puzo, G. *J. Biol. Chem.* **1993,** *268,* 12401-12411.

(18) Chatterjee, D.; Khoo, K. H. *Glycobiology* **1998,** *8,* 113-120.

(19) Lawn, S. D. *BMC Ifect. Dis.* **2012,** *12,* 103.

(20) Sarkar, S.; Tang, X.; Das, D.; Spencer, J.; Lowary, T.; Suresh, M.; Nigou, J. *PLOS ONE* **2012,** *7,* e32340.

(21) Hamasur, B. *J. Microbiol. Methods* **2001,** *45,* 41-52.

(22) Wood, R.; Racow, K.; Bekker, L.-G.; Middelkoop, K.; Vogt, M.; Kreiswirth, B.; Lawn, S. *BMC Ifect. Dis.* **2012,** *12,* 47.

(23) Sada, E.; Aguilar, D.; Torres, M.; Herrera, T. *J. Clin. Microbiol.* **1992,** *30,* 2415-2418.

(24) Sada, E.; Brennan, P.; Herrera, T.; Torres, M. *J. Clin. Microbiol.* **1990,** *28,* 2587-2590.

(25) Lawn, S. D.; Edwards, D. J.; Kranzer, K.; Vogt, M.; Bekker, L.-G.; Wood, R. *AIDS* **2009,** *23,* 1875-1880.

(26) Sarkar, P.; Biswas, D.; Sindhwani, G.; Rawat, J.; Kotwal, A.; Kakati, B. *Postgrad. Med. J.* **2014,**

(27) Drain, P.; Losina, E.; Coleman, S.; Giddy, J.; Ross, D.; Katz, J.; Walensky, R.; Freedberg, K.; Bassett, I. *BMC Ifect. Dis.* **2014,** *14,* 110.

(28) Tsigeweini Asgedom Tessema, B. H., Gunnar Bjune, Stefan Svenson, Bjarne Bjorvatn *Scand. J. Infect. Dis.* **2001,** *33,* 279-284.

(29) Kerkhoff, A. D.; Wood, R.; Vogt, M.; Lawn, S. D. *PLOS ONE* **2014,** *9,* e103285.

(30) Nicol, M. P.; Allen, V.; Workman, L.; Isaacs, W.; Munro, J.; Pienaar, S.; Black, F.; Adonis, L.; Zemanay, W.; Ghebrekristos, Y.; Zar, H. J. *The Lancet Global Health* **2014,** *2,* e278-e284.

(31) Dheda, K.; Davids, V.; Lenders, L.; Roberts, T.; Meldau, R.; Ling, D.; Brunet, L.; van Zyl Smit, R.; Peter, J.; Green, C. *PLOS ONE* **2010,** *5,* e9848.

(32) Boehme, C. *Trans. R. Soc. Trop. Med. Hyg.* **2005,** *99,* 893-900.

(33) Chan, J. *Infect. Immun.* **1991,** *59,* 1755-1761.

(34) Briken, V.; Porcelli, S. A.; Besra, G. S.; Kremer, L. *Mol. Microbiol.* **2004,** *53,* 391-403.

(35) Arias-Bouda, L. M. P.; Nguyen, L. N.; Ho, L. M.; Kuijper, S.; Jansen, H. M.; Kolk, A. H. *J. Clin. Microbiol.* **2000,** *38,* 2278-2283.

(36) Mishra, A. K.; Driessen, N. N.; Appelmelk, B. J.; Besra, G. S. *FEMS Microbiol. Rev.* **2011,** *35,* 1126-1157.

(37) Sakamuri, R.; Price, D.; Lee, M.; Cho, S.; Barry, C.; Via, L.; Swanson, B.; Mukundan, H. *Tuberculosis* **2013,** *93,* 301-307.

(38) Tessema, T.; Bjune, G.; Hamasur, B.; Svenson, S.; Bjorvatn, B.; Syre, H. *Scand. J. Infect. Dis.* **2002,** *34,* 97-103.

(39) Cox, J. A.; Lukande, R. L.; Kalungi, S.; Van Marck, E.; Van de Vijver, K.; Kambugu, A.; Nelson, A. M.; Colebunders, R.; Manabe, Y. C. *PLOS ONE* **2015,** *10,* e0123323.

(40) Granger, J.; Granger, M.; Firpo, M.; Mulvihill, S.; Porter, M. *Analyst* **2013,** *138,* 410-416.

(41) Driskell, J. D. *Anal. Chem.* **2005,** *77,* 6147-6154.

(42) Grubisha, D. S. *Anal. Chem.* **2003,** *75,* 5936-5943.

(43) Stuart, D. A.; Haes, A. J.; Yonzon, C. R.; Hicks, E. M.; Van Duyne, R. P. *IEE Proc.-Nanobiotechnol.* **2005,** *152,* 13-32.

(44) Xu, S.; Ji, X.; Xu, W.; Li, X.; Wang, L.; Bai, Y.; Zhao, B.; Ozaki, Y. *Analyst* **2004,** *129,* 63-68.

(45) Chon, H.; Lee, S.; Son, S.; Oh, C.; Choo, J. *Anal. Chem.* **2009,** *81,* 3029-3034.

(46) Bantz, K.; Meyer, A.; Wittenberg, N.; Im, H.; Kurtuluş, Ö.; Lee, S.; Lindquist, N.; Oh, S.-H.; Haynes, C. *Phys. Chem. Chem. Phys.* **2011,** *13,* 11551-11567.

(47) Graham, D.; Goodacre, R. *Chem. Soc. Rev.* **2008,** *37,* 883-884.

(48) Porter, M. D.; Lipert, R.; Siperko, L.; Wang, G.; Narayanan, R. *Chem. Soc. Rev.* **2008,** *37,* 1001-1011.

(49) Sharma, B.; Frontiera, R.; Henry, A.-I.; Ringe, E.; Van Duyne, R. *Mater. Today* **2012,** *15,* 16-25.

(50) Lim, C. Y.; Owens, N. A.; Wampler, R. D.; Ying, Y.; Granger, J. H.; Porter, M. D.; Takahashi, M.; Shimazu, K. *Langmuir* **2014,** *30,* 12868-12878.

(51) Moskovits, M. *Rev. Mod. Phys.* **1985,** *57,* 783-826.

(52) McCreery, R. L. *Raman Spectroscopy for Chemical Analysis*; John Wiley & Sons: New York, 2005.

(53) Park, H.-Y.; Lipert, R.; Porter, M.; Islam, M. S.; Dutta, A. *Proc. of SPIE* **2004,** *5593,* 464-477.

(54) Driskell, J.; Lipert, R.; Porter, M. *J. Phys. Chem. B* **2006,** *110,* 17444-17451.

(55) Haiss, W.; Thanh, N. T. K.; Aveyard, J.; Fernig, D. *Anal. Chem.* **2007,** *79,* 4215-4221.

(56) Gaylord, H. *Infect. Immun.* **1987,** *55,* 2860-2863.

(57) Bradley, M. Advancements of Surface-enhanced Raman Scattering-based Immunoassays and Colorimetric-solid Phase Extraction. Master of Science, University of Utah, Dec. 2010.

(58) Hegner, M. *Surf Sci.* **1993,** *291,* 39-46.

(59) Kumar, A.; Biebuyck, H. A.; Whitesides, G. M. *Langmuir* **1994,** *10,* 1498-1511.

(60) Laurentius, L. B.; Crawford, A. C.; Mulvihill, T. S.; Granger, J. H.; Spencer, J. S.; Chatterjee, D.; Porter, M. D. *Anal. Chem.* **2016,** *Unpublished work,*

(61) Park, H.-Y.; Driskell, J.; Kwarta, K.; Lipert, R.; Porter, M.; Schoen, C.; Neill, J.; Ridpath, J.; Kneipp, K.; Moskovits, M.; Kneipp, H. *Surface-enhanced Raman Scattering: Physics and Applications*; Springer: 2006; Vol. 103, p 427-446.

(62) Benator, D. *Lancet* **2002,** *360,* 528-534.

(63) Spencer, J. S.; Kim, H. J.; Wheat, W. H.; Chatterjee, D.; Balagon, M. V.; Cellona, R. V.; Tan, E. V.; Gelber, R.; Saunderson, P.; Duthie, M. S.; Reece, S. T.; Burman,

W.; Belknap, R.; Mac-Kenzie, W. R.; Geluk, A.; Oskam, L.; Dockrell, H. M.; Brennan, P. J. *Clin. Vaccine Immunol.* **2011,** *18,* 260-267.

(64) Anderson, A. J. *Nature* **1965,** *208,* 491-492.

(65) Chatterjee, D.; Bozic, C. M.; McNeil, M.; Brennan, P. J. *J. Biol. Chem.* **1991,** *266,* 9652-9660.

(66) Vercellone, A.; Nigou J Fau - Puzo, G.; Puzo, G. *Front. Biosci.* **1998,** *3,* e149-163.

(67) Ludwiczak, P.; Brando, T.; Monsarrat, B.; Puzo, G. *Anal. Chem.* **2001,** *73,* 2323-2330.

(68) Maura, R. B.; Fernandez, S.; Reyes, G.; Perez, J. L.; Reyes, F.; de los Angeles García, M.; Fariñas, M.; Infante, J. F.; Tirado, Y.; Puig, A. *VacciMonitor* **2010,** *19,* 20-26.

(69) Singh, A. K.; Reyrat, J. M. *Curr. Protoc. Microbiol.* **2009,** 10C. 1.1-10C. 1.12.

(70) Reyrat, J. M.; Kahn, D. *Trends Microbiol.* **2001,** *9,* 472-474.

(71) Patil, S.; Ramu, G.; Prasad, R. *J. Neuroimmunol.* **2000,** *105,* 64-68.

(72) Daley, P. *Int. J. Tuberc. Lung Dis.* **2009,** *13,* 989-995.

(73) Minion, J.; Leung, E.; Talbot, E.; Dheda, K.; Pai, M.; Menzies, D. *Eur. Respir. J.* **2011,** *38,* 1398-1405.

(74) Mdivani, N.; Li, H.; Akhalaia, M.; Gegia, M.; Goginashvili, L.; Kernodle, D. S.; Khechinashvili, G.; Tang, Y. W. *Clin. Chem.* **2009,** *55,* 1694-1700.

(75) Jiang, L. *J. Microbiol. Biotechnol.* **2012,** *22,* 1301-1306.

(76) Yew, W. W. *Clin. Chim. Acta* **2001,** *313,* 31-36.

(77) Keeler, E.; Perkins, M. D.; Small, P.; Hanson, C.; Reed, S.; Cunningham, J.; Aledort, J. E.; Hillborne, L.; Rafael, M. E.; Girosi, F. *Nature* **2006,** *444,* 49-57.

(78) Wang, G.; Park, H.-Y.; Lipert, R. J.; Porter, M. D. *Anal. Chem.* **2009,** *81,* 9643-9650.

(79) Mukundan, H.; Kumar, S.; Price, D.; Ray, S.; Lee, Y.-J.; Min, S.; Eum, S.; Kubicek Sutherland, J.; Resnick, J.; Grace, W. K.; Anderson, A.; Hwang, S.; Cho, S.; Via, L.; Barry, C.; Sakamuri, R.; Swanson, B. *Tuberculosis* **2012,** *92,* 407-416.

(80) Schmidt, R.; Jacak, J.; Schirwitz, C.; Stadler, V.; Michel, G.; Marmé, N.; Schütz, G. J.; Hoheisel, J. r. D.; Knemeyer, J.-P. *J Proteome Res* **2011,** *10,* 1316-1322.

(81) Chan, C. E.; Gotze, S.; Seah, G. T.; Seeberger, P. H.; Tukvadze, N.; Wenk, M. R.; Hanson, B. J.; MacAry, P. A. *Sci. Rep.* **2015,** *5,* 1-12.

(82) Hamasur, B.; Bruchfeld, J.; van Helden, P.; Kallenius, G.; Svenson, S. *PLOS ONE* **2015,** *10,* e0123457.

CHAPTER 6

CONCLUSION

6.1 Future Perspectives

The global population is desperately in need of diagnostic methods that are available, affordable, and reliable for low-resource regions. The regions display the highest burden due to close living quarters, lowered hygiene standards, limited health resources that allow for communicable diseases to thrive. Diseases such as human immunodeficiency virus/acquired immunodeficiency syndrome (HIV/AIDS), tuberculosis (TB), diarrheal diseases, vaccine-preventable diseases, malaria, respiratory infections, neonatal deaths, and maternal conditions experience increased mortality rates in low and middle income regions simply due to the lack available health care. The cost and resources required for state-of-the-art medical care, which reduces the availability to prevent, diagnose, and treat disease in areas with high exposure, limit the ability to implement these techniques. This indicates a high demand for the development of reliable and effective methods that can function with the limited resources for example, restricted electricity and clean water, in the region of need.

Large portions of research-based resources for diagnostics are directed towards the production of novel techniques. New methods that use state-of-the-art materials,

equipment, and novel concepts are commonly pursued. As such, the boundaries of knowledge are continually pushed. These technological advancements are however, inconsequential if an application of the research is never achieved. Diagnostic research directed towards potentially life-changing technologies that are cost effective, easy to use, and reliable is needed to validate new technology for the betterment of mankind. In order to develop this type of diagnostic method for regions with limited resources and mortality rates of curable and preventable infectious diseases a researcher should take into account the resources available at the point of care.

In order to move forward, reexamination of available methods is sometimes required. The fine tuning of fundamental principles involved can lead to advancements in the application of a method. This dissertation is predominantly directed towards the improvement of a nanoparticle (NP)-based surface-enhanced Raman scattering (SERS) immunoassay. The influence of extrinsic Raman label (ERL) sampling on the SERS substrate and AuNP sedimentation were investigated and revealed sources of error that cause decreased reproducibility of the results. Thoroughly understanding potential sources of error and implementation of methods that reduce their impact has led to advancement, not only in the reliability of the method, but also in the reliability of the results and the conclusions drawn from them.

In Chapter 2 and Chapter 3, fundamental investigation into sources of error in the results of an NP-based SERS immunoassay in terms of sampling and ERL sedimentation is investigated. The use of NP-based ERLs in a sandwich immunoassay format produces unique challenges that have not previously been well discussed, or were overlooked entirely. The variability in SERS signal intensity has led to speculation as to the reliability

of SERS, based on the limited reproducibility of many systems. Understanding the specific sources of errors associated with the NP-based SERS immunoassay provides an avenue for increased accuracy and precision, resulting in more reliable and impactful results.

The NP-based SERS immunoassay quantification is based on the excitation of the localized surface plasmon resonance by the external laser source on the SERS substrate. The resulting signal strength is dependent on the number of ERLs within the excitation. This indicates that the focused laser spot on the surface defines the sample size. To determine the impact of the sample size on this specific type of analysis, a simulation of the distribution of ERLs on a SERS substrate and the subsequent analysis of the SERS substrate were conducted. Results from the simulation display how the number of replicate measurements on a substrate ($n_{\text{replicate}}$) and laser spot size influence the accuracy and precision of results. While the accuracy is improved with increased $n_{\text{replicate}}$, the precision reaches a point where it cannot be improved past the fundamental error associated with the sample size. This fundamental error can be larger than instrumental error introducing a avoidable and large source of error. However, the accuracy and precision are improved by increasing the sample size, which statistically more reliably indicates the true density of ERLs on the substrate. The practical application of this information indicates that while an objective with a higher numerical aperture increases collection efficiency, the small focused laser spot inherently dictates the accuracy and precision of a measurement. This is backed by empirical data indicating the reproducibility of the results can be increased by increasing the laser spot size; however, there is inherent trade off in signal strength.

The results for the simulation in Chapter 2 follow the assumption that the ERLs on the SERS immunoassay substrate are randomly distributed on the substrate. This would

follow a random sequential adsorption model for the adsorption of the ERLs. Assuming that the SERS signal intensity is related to the ERL density on the surface, high density Raman mapping of the SERS substrate should display a relatively even distribution of signal across the substrate with a given fundamental error. In Chapter 3, the preparation of ERLs and the SERS immunoassay substrate were investigated to determine methodologies to reduce signal variations across a single SERS immunoassay substrate. Investigation indicated that the sedimentation of ERLs on the surface disrupts the adsorption of the ERL. This is believed to be a consequence of settled ERLs potentially blocking specific biding sites and an increased level of nonspecific adsorption, and limiting specific interactions, which also leads to larger signal distributions. Investigation allowed for prediction and characterization of the ERL sedimentation through a finite volume method used to solve the partial differential described by the Mason-Weaver equation for NP sedimentation. Results show that through proper modification, ERL sedimentation can be minimized but that the AuNP core with a finite size and high density will always display some inherent sedimentation. The impact of transport due to sedimentation can be removed through simple inversion of the substrate during the ERL incubation step. This keeps stable particles free in solution to interact and bind to antigen immobilized on the capture substrate through strictly diffusional transport. This method produced a much more consistent and even signal distribution on the SERS immunoassay substrate.

Understanding the potential sources of error in the SERS immunoassay allows for the implementation of techniques that reduce the signal variability and increase reproducibility. These techniques were applied to the global health problem associated with tuberculosis (TB) detection. With one third of the world's population believed to be

infected with the causative agent *Mycobacterium tuberculosis* (*M. tuberculosis*) and as the world's second deadliest infectious disease for a single infectious agent, TB is a considerable global threat. This is primarily due to the lowered health and sanitation standards for low-resource regions as well as a high occurrence of coinfection with immune suppressing diseases. Areas of Asia and Africa display the highest burden from TB as these regions that lack simple resources such as medical professionals, clean needles, electrical power, and a clean water source. These limited resources put a large number restrictions on a diagnostic method due to the additional constraints of resources for development of a reliable test.

Initially, the primary goal was to develop a serological test for an antigenic marker or markers that is reliable for potentially immunocompromised patients in regions with high exposure. This excludes testing for antibodies because of low production of antibodies in some immunocompromised patients and production of antibodies in noninfected patients that have been exposed to antigens, respectively. The goals of the project were expanded after the World Health Organization (WHO) called for the ban of all currently available serologically-based TB tests due to the level of inaccuracy having negative impact on the patients' health. There were many steps to try and identify a reliable TB marker, including assay development, investigation of multiple antigenic markers, identification of the unique potential of lipoarabinomannan (LAM) as a lipopolysaccharide, investigation of serum pretreatment, and application of findings towards the identification of mannose-capped LAM (ManLAM) in a panel of serum samples from an endemic area. However, the potential impact of this work is based on cumulative understanding of the detection platform, the study of antigenic TB markers, and identification of methods that reduce

serum matrix effects. With the combination of advancements, results from a panel of endemic serum samples indicate potential validation of a new diagnostic method as well as indicate the potential of ManLAM as reliable antigenic marker for TB.

I believe that if the progresses and/or conceptual advancements in this dissertation can be implemented towards the eventual application of technology that improves the quality of a single life, then all the effort is validated. Applicable advancements do not happen overnight and are possible due to the combination of work achieved by previous generations of scientists, parallel developments, and collaboration. Only time will tell what the future will bring, but I have done my best to try and ensure that my research has what I consider a positive impact.